Alma Mater Studiorum · University of Bologna

School of Science
Department of Physics and Astronomy
Master Degree in Physics

DEVELOPMENT AND CHARACTERIZATION OF A NEUTRON IMAGING SYSTEM FOR CULTURAL HERITAGE

Supervisor:
Prof. Maria Pia Morigi

Co-supervisor:
Dott. Matteo Bettuzzi

Submitted by:
Naomi Orlandi

Academic year 2020/2021

Abstract

The use of non-destructive methods is highly relevant for cultural heritage objects, due to their uniqueness. Investigations by means of X-ray imaging is often sufficient to gain an overview of their constituent materials, manufacturing techniques and conservation state, but there are cases where this method reaches its limits. Hence, neutron imaging can provide new insights into the studied object, due to neutrons different interactions with matter. In Italy, INFN-CHNet (Cultural Heritage Network of the Italian National Institute for Nuclear Physics) NICHE (Neutron Imaging for Cultural HEritage) experiment aims to implement the first thermal neutron imaging facility in Pavia, at TRIGA reactor. The present work, as a part of NICHE project, provides the characterization of the detector of the neutron imaging system and tomographic analyses of different samples. In particular, the thesis describes the experimental tests carried out to select the scintillator for the CCD-based detector. The spatial resolution of the system was evaluated both with a visual method, through the acquisition of a radiography of a gadolinium bar pattern, and by calculating the Modulation Transfer function. Further tests were performed to verify the linearity of response of the imaging system and the trend of the Signal-to-Noise Ratio as a function of the acquisition time of the CCD camera. Finally, three tomographies were executed with several samples, allowing their 3D external and internal visualization. A calibration curve was obtained for converting gray levels of the reconstructed images of samples with known composition, into the neutron total macroscopic cross section for the corresponding materials. The experimental tests described in this work have provided satisfactory results, but they have also highlighted some critical points of the neutron imaging system. Therefore, the first prototype of the CCD-based detector has been recently upgraded in order to improve its performance.

Contents

Introduction

Cultural heritage objects, which are generally unique and delicate, have to be studied by means of non-invasive testing methods. Among these, techniques based on the transmission of radiation, such as neutron and X-ray imaging have proven to be particularly suitable as they provide inside information on the structure and composition of the studied object [20]. Both X-ray and neutron imaging are based on the attenuation of the radiation beam, after its interaction with the sample under study. The resulting images will present areas with different brightness based on the different attenuation of the beam produced by the materials that make up the sample.

Imaging techniques include radiography, which provides a 2D image of the sample, and tomography, in which a set of 2D radiographies are acquired and processed with specific algorithms to reconstruct and visualize the three dimensional volume of the sample. Tomography, in particular, allows an accurate investigation of the inside of artefacts, without affecting their integrity.

The difference between X-rays and neutron images stands in the different interaction behaviours shown by the two radiations with matter. X-rays attenuation is strongly correlated to the atomic number of the interacting element, where light elements, like hydrogen, are low attenuating. For neutrons, no clear correlation with the atomic number can be found. Nevertheless, the attenuation behaviour can be described as partially complementary to that of X-rays as some light elements, such as hydrogen, lithium and boron, show high attenuation coefficients, while some heavy metals, such as lead, are practically transparent. Hence, the combination of the two imaging methods is usually performed for a more exhaustive examination of cultural heritage objects.

While X-ray radiography has been applied to the cultural heritage field since the 1930s, neutronic radiography had to wait the 1950s and still in 1990s it was quite a new method, because of slower development of the radiation sources and detectors for neutrons.

Nowdays there are about twenty neutron imaging facilities all around the world. In this regard, the INFN-CHNet (Cultural Heritage Network of the Italian National Institute for Nuclear Physics) NICHE (Neutron Imaging for Cultural HEritage) experiment aims to implement the first neutron imaging facility in Italy, in Pavia, with the usage of the thermal neutron flux produced in the TRIGA MARK II reactor at LENA (Applied Nuclear Energy Laboratory).
The present work is a part of the NICHE research project and its objectives are the development and the characterization of the neutron imaging system for the acquisition of neutron radiographies and tomographies, applicable in the field of cultural heritage.
About the characterization of the experimental detection setup, an analysis of different scintillators was performed in order to choose the most adequate to achieve the research goal. Then the linearity of the detector response, the spatial resolution and the signal to noise ratio were evaluated. Some preliminary radiographic tests and finally three neutron tomographic scans were performed with several samples made of different materials. The acquired images were corrected from the misalignment of the sample axis of rotation with the central axis of the detector. Considering the samples with known composition, a calibration curve for converting the gray levels of the reconstructed images into the neutron total macroscopic cross section for the corresponding materials was obtained. For one sample, previously investigated in an experimental research reported in [29], the reconstructed images were visually compared with the published ones.
The chapters of the thesis are the following. Chapter 1 is a generic introduction to tomography, with a short description of radiation-matter interactions for X-rays and neutrons, a presentation of the principles of attenuating imaging techniques, a definition and a brief history of tomography and its mathemathical foundamentals. Chapter 2 is focused on neutron tomography applied to cultural heritage, with a comparison with X-ray imaging method, a description of some case studies and a list of the current available neutron imaging facilities. Chapter 3 describes a typical imaging acquisition setup, with all its components in details, and how to perform a characterization of the detection system. Chapter 4 is about NICHE project, its materials and methods. Chapter 5 reports the results of the characterization of the detection system (choice of the scintillator, linearity of the system response, spatial resolution, signal to noise ratio), of preliminary neutron radiographies and of the first neutron tomographies. In chapter 6 there are the discussions about the results and in chapter 7 some concluding remarks.

Chapter 1

Tomography

1.1 Radiation-matter interactions

1.1.1 X-rays

X-rays are electromagnetic waves, i.e. oscillating electric and magnetic fields. They principally interact with the electrons in the atoms of irradiated sample. They can be absorbed or scattered. The absorption interactions are the following:

- **Photoelectric effect**. X-ray photon transfers all its energy to a tight bound inner-shell electron, being completely absorbed. The electron is emitted with an energy ($E_{photoelectron}$) equal to the difference between the photon energy ($h\nu$) and its biniding energy (E_b):

$$E_{photoelectron} = h\nu - E_b \tag{1.1}$$

  with h Planck constant and ν frequency of the incoming radiation. The vacancy left by the electron is filled by an electron of outer shells, giving rise to the so called *characteristic X-rays* emission. The emitted radiation energy is equal to the difference between the energies of the different levels which the electrons belong to.

- **Pair and Triplet production**. The photon interacts with a strong electric field from the nucleus of the atom or from an atomic shell electron, giving rise to the emission of a pair electron (e^-) - positron (e^+) in the first case and of a triplet e^--e^+-$e^-_{original}$ in the second case. A X-ray threshold energy of 1,02 MeV and of 2,04 MeV is required for pair and triplet production respectively.

- **Photonuclear reaction.** If the photon energy is greater than the binding energy that holds protons (p) and neutrons (n) together in the nucleus, it can interact directly with the nucleus, be completely absorbed and lead to the ejection of a particle (p or n). The threshold x-ray energy for this reaction is of 10.8 MeV.

The scattering interactions are listed here:

- **Rayleigh scattering**, elastic scattering or coherent scattering. The oscillating electric field associated with the wave (X-ray) puts the electrons of the atom in vibration. The oscillating electrons emit radiation with the same frequency of the incoming photon. The diffused waves give rise to interference, constructive in forward direction or distructive at high angles. The described process usually occur at low photon energies.

- **Compton scattering**, inelastic scattering or incoherent scattering. A photon interacts with an outer-shell electron, a portion of its energy is absorbed by the electron, giving rise to the emission of a recoil electron and a scattered photon with a different lower frequency (bigger wavelenght).

Figure 1.1 shows all the described reactions.

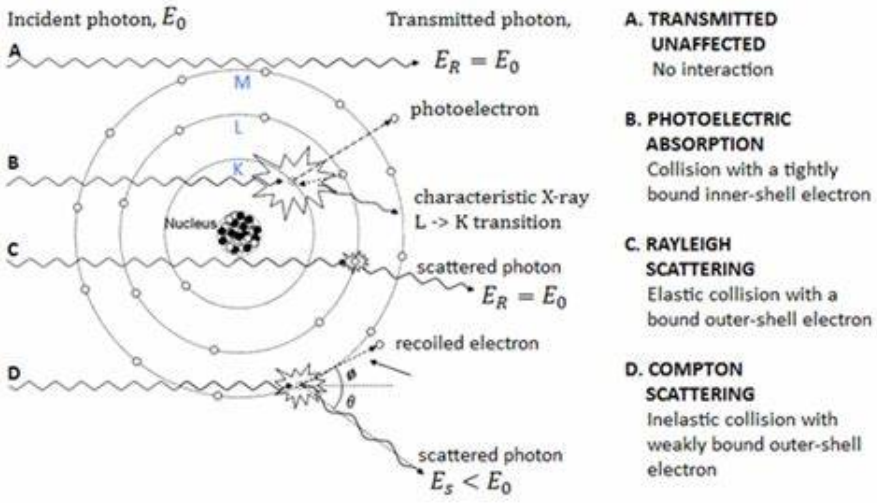

Figure 1.1: picture of the principal x-rays - matter interactions.

The probability of interaction is expressed by the so called *cross section* σ, that has the dimension of an area. Each type of interaction has its own probability and cross

section and the probability of each event is independent of the probabilities of the others, so the total probability of any event occurring is the sum of the individual probabilities. Similarly, the sum of all the individual cross sections is the total cross section:

$$\sigma_t = \sigma_{ph} + \sigma_c + \sigma_r + \sigma_{pair} \tag{1.2}$$

where σ_t is the total cross section, σ_{ph} is the photoelectric cross section, σ_c and σ_r are rispectively the compton and rayleigh scattering cross sections, and σ_{pair} represents the probability for pair production. Photonuclear reactions occur in a short energy range at high energy (in the order of MeV).
It is usefull to define the *linear attenuation coefficient* μ, with the inverse of a lenght dimension, that is the total cross section σ_t, multiplied by the mass density of the material ρ and the Avogadro's number N_a and divided by the atomic weight of the element, A:

$$\mu = \frac{N_a \rho}{A} \sigma_t \tag{1.3}$$

With the definition of μ, it is possible to introduce the Beer-Lamber law for X-rays, that defines the attenuation of X-rays interacting with a sample with thickness x in good geometrical conditions (photons that have interacted with the object can not interact with the detector):

$$I(x) = I_0 e^{-\mu x} \tag{1.4}$$

where $I(x)$ is the intensity of the radiation at x position, I_0 is the intensity of the incoming radiation, before the interaction with the sample, μ is the linear attenuation coefficient deifned in eq. 1.3 and x is the thickness of the sample. In general, the Beer-Lambert law, that can be applied to various type of radiations, requires some conditions to be satisfied:

1. attenuators must act independently one from each other;
2. the attenuating medium must be homogeneous in the interaction volume;
3. the incident radiation must consist of parallel rays, each traversing the same length in the absorbing medium;
4. the incident radiation should preferably be monochromatic;

The following fig. 1.2 represents the total *mass attenuation coefficient*, that is the ratio between μ and the density of the material ρ, as a function of the X-rays energy for interaction with Carbon (Z=6). The single contributes of each type of interaction are also reported.

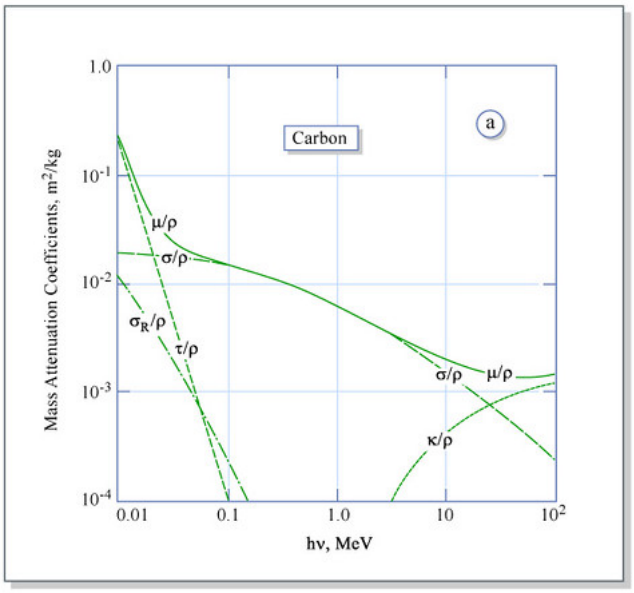

Figure 1.2: Total mass attenuation coefficient μ/ρ for X-rays interaction with Carbon (C) as a function of photon energy. τ/ρ is the component for photoelectic effect, σ_R/ρ for the Rayleigh scattering, σ/ρ for the Compton scattering and κ/ρ for pair production.

1.1.2 Neutrons

Neutron is a spin 1/2 particle, electrically neutral but with a magnetic moment. Therefore, they only interact with materials through the short-range nuclear forces and by magnetic interactions. Since neutrons are no charged particles and their electric dipole moment is either zero or too small to measure, they penetrate matter far better than charged particles. As a consequence, neutrons can penetrate thick layers of most materials without being scattered or absorbed [16]. Neutrons can be classified according to their energy, as shown in table 1.1. It affects the probability of their interactions with matter.

Neutrons	**Energy**
Cold	$< 0.005eV$
Thermal	$0.025eV$
Epithermal	$0.025 < E < 1eV$
Slow	$1 < E < 100eV$
Intermediate	$100eV < E < 1MeV$
Fast	$1MeV < E < 20MeV$
Relativistic	$> 20MeV$

Table 1.1: Neutron classification according to their Energies(eV)

The principal neutron-nuclear interactions are shown in fig.1.3 and described here:

- **Nuclear elastic reaction.** The nucleus is left in the same internal quantum state after interaction as before, but may gain or lose laboratory kinetic energy while the neutron respectively loses or gains kinetic energy. Neutron scattering can be elastic or inelastic, depending on whether the neutron changes energy in the scattering process or not; both cases are still nuclear elastic reactions.

- **Nucler inelastic reaction.** The nucleus absorbs energy from the neutron and is left in a different internal quantum state after the interaction than before. The struck nucleus eventually decays by photon (gamma-ray) emission, and the neutron emerges with lower energy than before colliding.

- **Absorption.** The neutron disappears into the nucleus, forming a compound nucleus in an excited state, one mass unit heavier than the original, which decays by emitting lighter particles or electrons. Usually the formation of a compound nucleus is promptly accompanied by emission of gamma rays. In many instances, a massive charged particle emerges from the reaction, and the products carry substantial kinetic energy. The residual nucleus may have a long lifetime (this is neutron activation) and beta decay may be followed by emission of characteristic gamma rays. The absorption cross sections for some isotopes are spin-dependent, that is, depend on the relative orientation of the nucleus and the neutron spin.

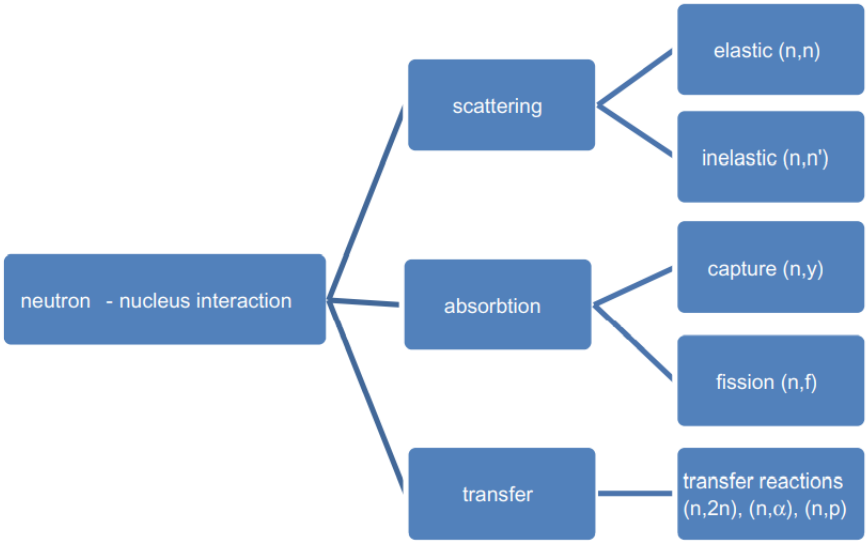

Figure 1.3: Scheme of the principal neutron-nuclear interactions. (source [16])

- **Fission.** The neutron disappears into the nucleus momentarily, leaving it in a highly excited state, from which the nucleus (must be a heavy nucleus, Z > 80) splits into two roughly equal fragments and a few light particles, almost always neutrons. Fission fragments carry about 180 MeV of energy, which appears as ionization and heat in the surroundings.

- **Capture.** The neutron disappears into the nucleus regardless of what happen afterwards (therefore, capture includes absorption and fission). Capture cross sections for low energy neutrons are usually proportional to the neutron wavelength.

- **Transfer.** The neutron collides directly with the nucleus and emits nucleons. Transfer reactions usually requires high energetic neutrons

The probability of a neutron interaction with a single nucleus is expressed by the microscopic cross section σ, that has the dimensions of an area. The sum of all the individual cross sections is the total cross section [17].
In general the total microscopic cross section σ_t is expressed by the following mathematical relation:

$$\sigma_t = \sigma_a + \sigma_s \tag{1.5}$$

where σ_a is the absorption cross section and σ_s is the scattering cross section, which is, $\sigma_s = \sigma_i + \sigma_{el}$, with σ_i inelastic scattering cross section and σ_{el} elastic scattering cross section.

Moreover, neutron cross section magnitudes are dependent on neutron energy.

Note that, as a general rule, cross section decreases with increasing energy. At low energies, below 1 MeV, elastic cross section is nearly constant, whereas inelastic scattering cross section and absorption cross section are proportional to the reciprocal of the neutron's speed (that is $1/v$). So, at low energies the total cross section can be nearly constant or decreasing with energy, depending on which type of event dominates. At higher energies the cross section may have large peaks superimposed on the $1/v$ trend. These peaks are called *resonances* and occur at neutron energies where reactions with nuclei are enhanced [17].

For example, a resonance will occur if the target nucleus and the captured neutron form a "compound" nucleus, and the energy contributed by the neutron is close to that of an excited state of the compound nucleus.

In fig. 1.4 total neutron microscopic cross sections for water (H_2O), Iron (Fe) and Aluminium (Al) are plotted as a function of the neutron energy. For neutrons slower than thermal ones, inelastic scattering and absorption interactions dominate, for thermal, epithermal and slow neutrons elastic scattering dominates, while for fast neutrons resonances can be visualized.

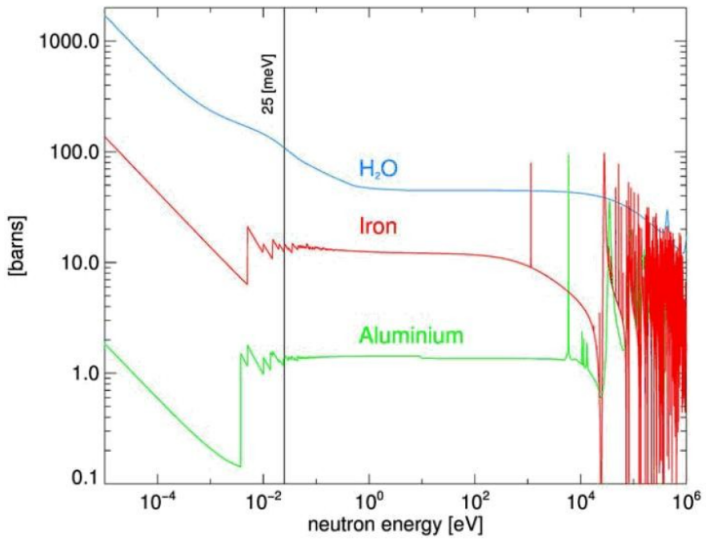

Figure 1.4: Energy dependence of neutron cross sections shown for aluminium, iron and the water molecule.

Fig. 1.5 shows the total neutron scattering and absorption cross sections for bound atoms across the periodic table [4]. In practice, the scattering cross sections are typically taken as constant in the epithermal, thermal, and into the cold neutron energy ranges.

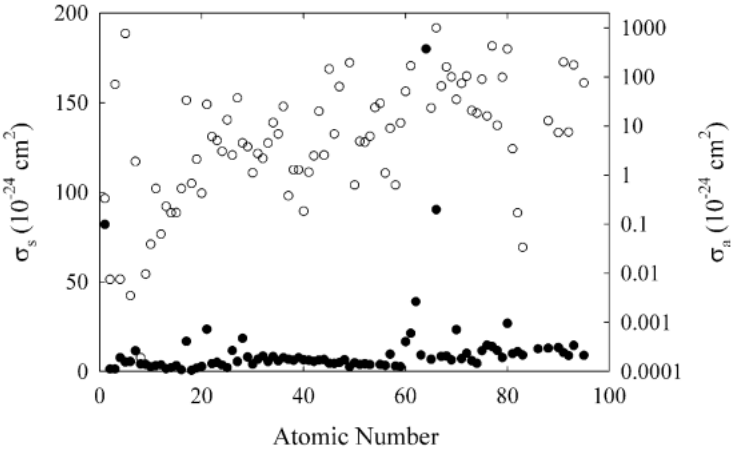

Figure 1.5: Neutron scattering and absorption cross sections for thermal neutrons ($v = 2200m/s$). Open circles are absorption cross sections and are plotted on the logarithmic scale of the right y-axis. Closed circles are the bound atom scattering cross sections plotted on the linear scale of the left y-axis. (source [4])

Although the study of the interactions of a neutron with a single nucleus on the microscopic scale provides a basis for understanding the interaction process, measurements are actually performed with thick samples that often contain a mixture of elements. These additional features are described by using the macroscopic cross sections, appropriate for bulk materials.

The definition of the macroscopic cross section arises from the transmission of a parallel beam of neutrons through a thick sample. The thick sample can be considered to be a series of atomic layers. For each layer one can apply the results found with the microscopic cross-section concept. By integrating through enough atomic layers to reach a depth x in the sample, the intensity $I(x)$ of the uncollided neutron beam follows the Beer-Lambert law, with the conditions listed in the previous section, and is:

$$I(x) = I_0 e^{-N\sigma_t x} = I_0 e^{-\Sigma_t x} \tag{1.6}$$

where I_0 is the intensity of the beam before it enters the sample, N is the atom density, σ_t is the total microscopic cross section. The total macroscopic cross section is $\Sigma_t = N\sigma_t$, with cm^{-1} unit of measure.

If the sample is a compound instead of a simple element, the total macroscopic cross section is the sum of the macroscopic cross sections of the individual elements:

$$\Sigma_t = \sum_i \Sigma_i = \sum_i N_i \sigma_{ti} \tag{1.7}$$

and the atom density of each element is given by

$$N_i = \frac{\rho N_a n_i}{M} \tag{1.8}$$

where ρ and M are respectively the compound density and molecular weight, N_a is the Avogadro number (6.022×10^{23}) and n_i is the number of atoms of i-th element in one molecule.

1.2 Attenuation imaging techniques

Among many ways to display information about real objects, the use of images is the most direct, easy to understand and widespread method.
Images in the original sense represent real-space information about optical properties of objects, e.g. brightness, colour, shininess. In a more general sense, images describe spatial distributions of physical properties such as density or element distribution. Often, images are obtained by using radiation that passes through an object, during which the radiation properties are modified: radiation can be simply attenuated, shifted in phase, deflected, scattered, or changed in energy. After passing through the objects, suitable detector systems detect and record the changes [1].
Imaging diagnostic techniques like radiography and tomography concern the attenuation of particle beams through their interaction with matter. The attenuation of the incident beam, that can be electromagnetic radiation or a beam of particles such as protons, electrons or neutrons, is exponentially depending on the thickness d and the attenuation coefficient of the material. It is mathematically expressed by the Beer-Lambert law, under specific contitions, listed in section 1.1.1:

$$\frac{I(d)}{I_0} = exp(-\mu d) \qquad for \quad X-rays \tag{1.9}$$

$$\frac{I(d)}{I_0} = exp(-\Sigma d) \qquad for \quad neutrons \tag{1.10}$$

where $I(d)$ is the intensity of the attenuated beam at d position, I_0 is the initial beam instensity, before the interaction with the sample, μ is the linear attenuation coefficient for X-rays, Σ is the total macroscopic cross section for neutrons and d is the thickness of the material. Figure 1.6 shows the discribed situation.

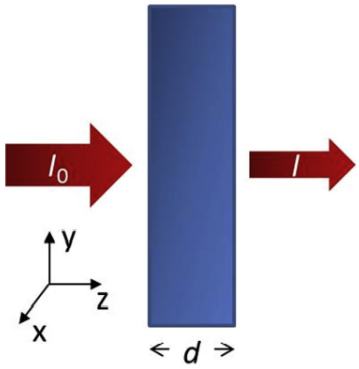

Figure 1.6: A schematic representation of beam attenuation by a material with thickness d.

Radiography produces a single 2D attenuation map of the radiation that has penetrated the examinated object. Tomography, instead, exploiting the acquisition of multiple radiographic projections, allows a 3D reconstruction and visualization of the sample.

1.3 Tomography definition and history

The word 'tomography' comes from the Greek words 'tomos' (to cut or section) and 'graphein' (to write). It is a *non-destructive* imaging technique that allows to get physical and morphological information about the structure of the studied sample.
Tomography relies on the acquisition of radiographic projections at different views, usually equiangular steps from 0° to 180° or 360°. Reconstruction algorithms are performed on these images to get the distribution of materials in the sample and its 3D visualization.
Historically, very shortly after the discovery of X-rays in 1895, one of the first ever X-ray radigraphic images was acquired by Wilhelm Conrad Rontgen (1845–1923) from the hand of a colleague in 1896 (figure 1.7). In the same year, the first use of X-rays under clinical conditions was made by John Hall-Edwards in Birmingham, England, when he radiographed a needle stuck in the hand of an associate. Owing to the geometry of the arrangement, features within the object behind each other with respect to the beam direction were superimposed and could not be separated. Doctors tried to partially overcome this problem by turning the hand of the patient, and to acquire more than one radiogram from different angles. From this procedure a further important step was taken with the invention of medical tomography by Godfrey N. Hounsfield (1919-2004) in

Figure 1.7: X-ray radiogram made by Wilhelm Conrad Rontgen of the hand of a colleague in 1896.

1967. A mathematical reconstruction algorithm was applied to images to approximately calculate the X-ray attenuation coefficient of any spatial volume inside the object. The mathematical foundations were first laid by Johann Radon (1917), but the contribution of Allan Cormack (1963), who, many years later, formulated some of the mathematical principles, is considered equally important.

Computed tomography (CT) has a long story in medical and industrial fields before its application in cultural heritage. X-ray radiography first entered in museums in 1930s [2], but more recently CT has been applied in cultural heritage analysis. The first CTs were performed by means of medical CT scanners, usually with courtesy and permission of hospitals. However, the use of medical CT scanners gave good results only in case of analysis of samples with size and density similar to those of the human body, but this requirement is not always satisfied in the field of Cultural Heritage diagnostics, where various kinds of objects with different size and composition have to be analyzed. Moreover, it is usually difficult to move the works of art from the place where they are located [3]. Hence, new portable X-rays acquisition systems were developed both for

radiographies and tomographies.

For what regards neutron imaging, although the discovery of neutrons by the English physicist James Chadwick occurred in 1932, the history of neutron radiography begins in 1935 when, in Germany, Kallmann and Kuhn performed the first experiments specifically concerned with generating images using neutrons [4]. Because of the Second World War, further development of neutron radiography did not occur until the mid-1950s. Indeed, Kallmann and Kuhn had to wait until 1948 to publish their results. Despite the War, nuclear reactor technology development continued, increasing the intensity of neutron fluxes available to researchers by many orders of magnitude. The first instance of a neutron radiograph being produced by a beam of thermal neutrons from a reactor occurred in 1956.

It took longer to develop neutron tomography than its X-ray counterpart simply because the fluxes of neutron sources are lower and the available 2D detectors less effective. Still, in the proceedings of the 4th World Conference on Neutron Radiography, 10 papers dealt with neutron tomography, quite a new method in 1992. It was in the 1990s that tomography was largely facilitated by new digital image acquisition systems – a prerequisite for fast and reliable 3D imaging.

Today, X-ray tomography based on either X-ray tubes or synchrotron X-ray sources on the one hand, and neutron tomography using neutrons from reactors or spallation sources on the other hand are standard techniques available at many laboratories worldwide. A fairly new idea is to combine X-ray and neutron imaging to couple different contrast generation mechanisms [5].

1.4 Tomography mathematical principles

1.4.1 Projections

An object O(x, y, z) is considered as a superposition of n layers of the same thickness along z axis, all located in planes parallel to the plane (x, y) and perpendicular to z (fig. 1.8). Each layer represents a section in the object to be reconstructed. The distribution of linear attenuation coefficients is a 2D function $f(x, y)$ of the position. The generalization of such function for the tomographic measurements is closely related to the determination of the nature of interaction of the scanning beam with the object under examination. The purpose of tomography is the reconstruction of this 2D function, representing a layer or slice of the object, from the measured projections in a unique way [6].

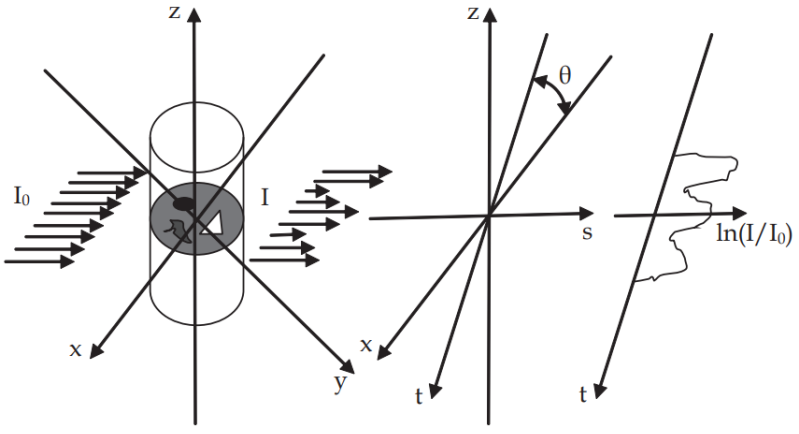

Figure 1.8: The geometry of a studied object scanning in the (x,y,z) coordinates system. A layer in the plane (x, y) is scanned along the angle θ and the transmitted intensity is stored in a system (t, s) of rotational coordinates. I_0 is the incident beam intensity, I is the attenuated intensity, $ln(I/I_0)$ is a measured line integral in the projection acquired at angle θ. (source [6])

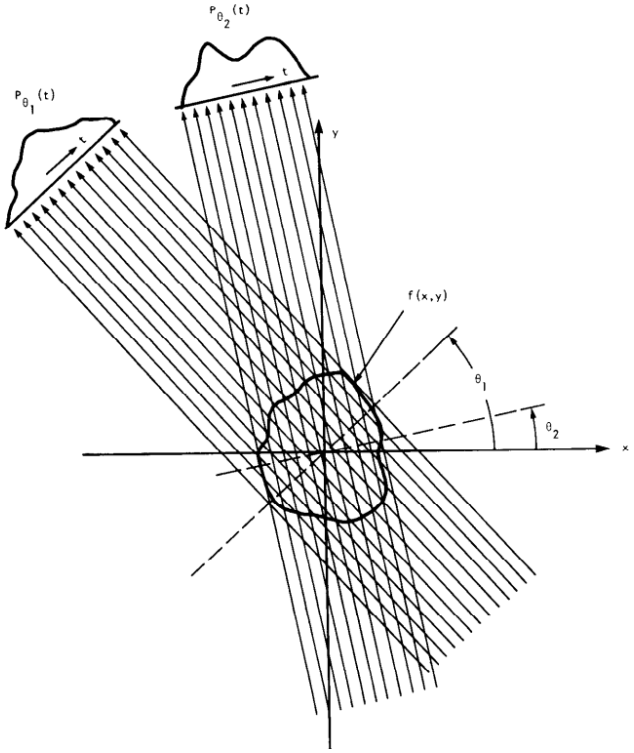

Figure 1.9: Parallel projections acquired at angles θ_1 and θ_2. f(x,y) represents the distribution of the attenuation coefficient in a slice of a 3D object. (source [7])

A parallel projection is obtained by measuring a set of parallel rays for a specific angle (fig. 1.9). The total attenuation of the radiation along a line through the object represents a line integral [7]. Hence, a projection consists of line integrals of the attenuation coefficient. A variable number of projections is acquired between angles 0° and 180° or 360° in order to reconstruct a single slice of the object.
Considering the Beer-Lambert law expressed by the eq. 1.9, the mathematical relation for a parallel projection is the following [6]:

$$P_\theta(t) = -ln(\frac{I}{I_0}) = \int_{path} \mu(x,y)ds = \int_{-\infty}^{+\infty} \delta(xcos\theta + ysin\theta - t)\mu(x,y)dxdy \qquad (1.11)$$

Here $P_\theta(t)$ is the line integral at position t in the projection at angle θ, I_0 is the incident beam intensity, I the attenuated intensity, directly derived by the Beer-Lambert law and $\mu(x,y) = f(x,y)$ is the 2D function to rebuild.
A new square and rotational coordinates system (t, s) is defined to express the rotatable

detection system in comparison to the fixed object coordinates system (or vice versa, if the object is rotating and the detection system is fixed). Hence

$$t = xcos\theta + ysin\theta \tag{1.12}$$

and the expression of the radiation path through the sample in terms of t and θ is $\delta(t - xcos\theta + ysin\theta)$. The Dirac function δ ensures that only the points that obeys to the eq. 1.12 and that are related to the beam contribute to $P_\theta(t)$. The last expression of eq. 1.11 is one of the different forms of the two dimensional Radon transform , that is a mapping from the Cartesian rectangular coordinates (x, y) to a distance and an angle (t, θ), also known as polar coordinates. Applying the Radon transform on an image f(x,y) for a given set of angles can be thought of as computing the projection of the image along the given angles.
Using all these projections, a 2D image can be analytically reconstructed by exploiting the so called "Fourier Slice" or "Central Slice" theorem, explained in the following section.

1.4.2 Fourier slice theorem

The theorem states:
The 1D Fourier transform of a parallel projection of an image $\mu(x, y)$, taken at angle θ, gives a slice of the two-dimensional Fourier transform, F(u,v), subtending an angle θ with the u-axis. In other words, the Fourier transform of $P_\theta(t)$ gives the values of $F(u, v)$ along line BB in Fig. 1.10.

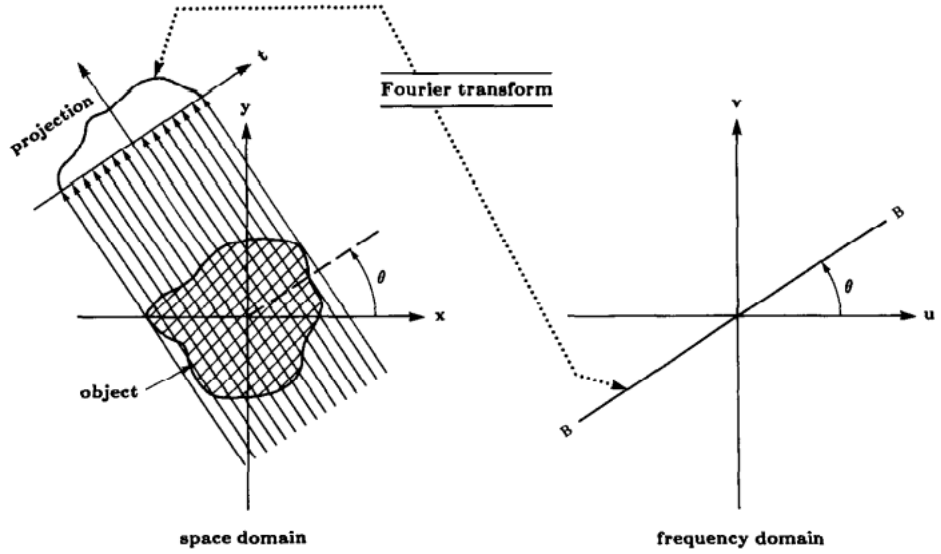

Figure 1.10: Illustration of the Fourier slice theorem

The derivation and the demonstration of the theorem are reported in [7] and [6]. The theorem indicates that one can determine the values of $F(u, v)$ on radial lines , by taking the projections of an object function at angles $\theta_1, \theta_2, ..., \theta_k$ and Fourier transforming each of these, as shown in Fig. 1.10. If an infinite number of projections are taken, then $F(u, v)$ would be known at all points in the uv-plane. Knowing $F(u, v)$, the object function $\mu(x, y)$ can be recovered by using the inverse 2D Fourier transform [7]

$$\mu(x, y) = \int_{-\infty}^{+\infty} \int_{-\infty}^{+\infty} F(u, v) e^{j2\pi(ux+vy)} dvdu \tag{1.13}$$

where $F(u, v)$ is the 2D Fourier transform of $\mu(x, y)$:

$$F(u, v) = \int_{-\infty}^{+\infty} \int_{-\infty}^{+\infty} \mu(x, y) e^{-j2\pi(ux+vy)} dxdy \tag{1.14}$$

1.4.3 Reconstruction

The most common reconstruction methods divide in two groups: *analytical* and *algebraic*. Analytical methods, of which filtered backprojection (FBP) is the most widely used example, are based on a continuous representation of the reconstruction problem. The advantage of these methods is that they are usually computationally inexpensive.

However, the approach is based on the assumption that the projection data is available for all angles, which is clearly not feasible in practice. As a result, the reconstruction quality of analytical methods tends to become unacceptable when data is only available for a small number of angles.

Algebraic reconstruction methods, such as ART (Algebraic Reconstruction Technique) and SIRT (Simultaneous Iterative Reconstruction Technique) [8], often handle limited-data problems better than analytical methods. They are based on a discrete representation of the problem, which leads to a system of linear equations. These equations can be solved using iterative methods. They provide more accurate reconstruction than analytical methods but they have a very high computational cost, often several orders of magnitude larger than analytical methods. Recently a new method that uses ANN (Artificial Neural Network) has been developed. This method is computationally similar to analytical methods, ensuring a low computational cost. Furthermore, it learns how to use problem specific knowledge to produce more accurate reconstructions than existing analytical methods. No specific prior knowledge has to be presented to the method, making it applicable to any type of image [10].

In this section the filtered back projection algorithm will be described.

As the name implies, there are two steps to the algorithm: the filtering part, which can be visualized as a simple weighting of each projection in the frequency domain, and the backprojection part, which is equivalent to finding the elemental reconstructions in the spatial domain.

The basic idea of this algorithm is derived from the tomography principle and the scanning mode: the object (set of layers) is scanned by projections from 0° to 180°, at least, which means that $P_\theta(t) = P_{\theta+180}(-t)$, suggesting the use of a polar coordinates rather than Cartesian square ones.

One can rewrite eq.1.13 in polar coordinates [6]:

$$\mu(x,y) = \int_0^{2\pi} \int_{-\infty}^{+\infty} F(\omega,\theta) e^{j2\pi\omega(xcos\theta+ysin\theta)} \omega d\omega d\theta \tag{1.15}$$

where $u = \omega cos\theta$ and $v = \omega sin\theta$.
Considering the relation 1.12, the following expression is obtained:

$$\mu(x,y) = \int_0^{\pi} \int_{-\infty}^{+\infty} [F(\omega,\theta)e^{j2\pi\omega t}|\omega|d\omega]d\theta = \int_0^{\pi} \left[\int_{-\infty}^{+\infty} F(\omega,\theta)e^{j2\pi\omega t}|\omega|d\omega \right] d\theta \quad (1.16)$$

Here, for the Fourier Slice Theorem, the 2D Fourier transform (FT) $F(\omega,\theta)$ can be substituted with the 1D FT of the projection at angle θ, $S_\theta(w)$:

$$\mu(x,y) = \int_0^{\pi} \left[\int_{-\infty}^{+\infty} S_\theta(w)e^{j2\pi\omega t}|\omega|d\omega \right] d\theta \quad (1.17)$$

and introducing

$$Q_\theta(t) = \int_{-\infty}^{+\infty} S_\theta(w)e^{j2\pi\omega t}|\omega|d\omega \quad (1.18)$$

the integral 1.17 becomes:

$$\mu(x,y) = \int_0^{\pi} [Q_\theta(t)]d\theta = \int_0^{\pi} [Q_\theta(xcos\theta + ysin\theta)]d\theta \quad (1.19)$$

$Q_\theta(xcos\theta+ysin\theta)$ is the so called "filtered projection", since $|\omega|$ plays the role of a special ramp filter function in frequency domain.
It is known that a product in Fourier space (frequency domain) corresponds to a convolution of inverse Fourier transforms (IFT) in real space (spatial domain). The IFT of $|\omega|$ can be approximated by a filter response function (convolution with gains, filter functions) [6].
At this point the reconstruction process of $\mu(x,y)$ from the projections $P_\theta(t)$ can be summarized as following:

1. the projections $P_\theta(t)$ for all the θ angles are acquired (fig.1.11).

2. The projections are converted to grayscale and convoluted with a filter with a specific gain.

3. The filtered projections are back-projected onto the entire plane (x,y). The addition of all projections result in the reconstruction of the 2D layer desired. The greater is the number of projections, the better the reconstruction plane will be

covered in terms of data and less the star-shaped artefacts will be present on the reconstructed image, as shown in fig.1.12.

With such reconstructions, 3D images can be obtained by stacking all the 2D layers and a reconstructed 3D volume data (details of the object) can be extracted from the stack obtained.

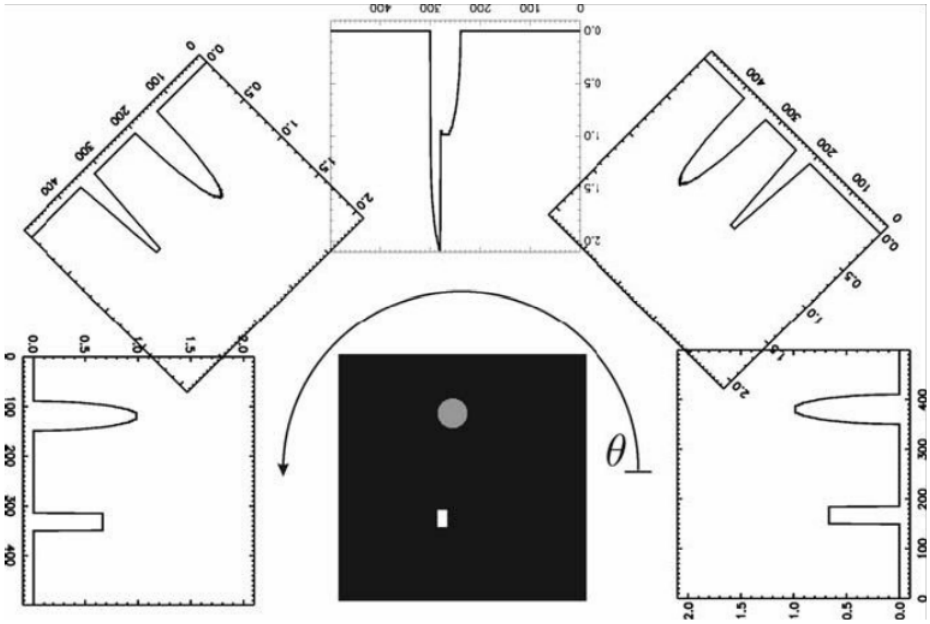

Figure 1.11: Illustration of the projections at different θ angles of a 2D object (details: circle and square). (Source [6])

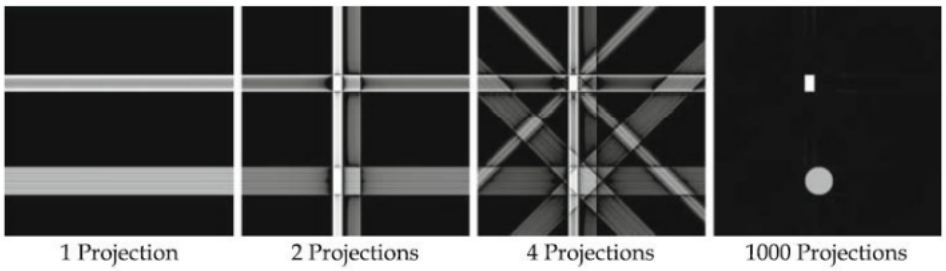

Figure 1.12: Reconstructions of the 2D object in fig.1.11 obtained with 4 different numbers of projections (1, 2, 4, 100) to show the appearance of star-shaped artifacts when the number of projections is not sufficient. (Source [6])

The theory above is valid for reconstructing images from their parallel projections, acquired as in fig.1.8 and fig.1.9, where a source-detector combination has to linearly scan over the length of a projection, then rotate through a certain angular interval, then scan linearly over the length of the next projection, and so on. A much faster way to generate the line integrals is by using fan beams such as those shown in fig.1.13, where a source of radiation emanates a fan-shaped beam and on the other side of the object an array of detectors is used to make all the measurements in one fan simultaneously.

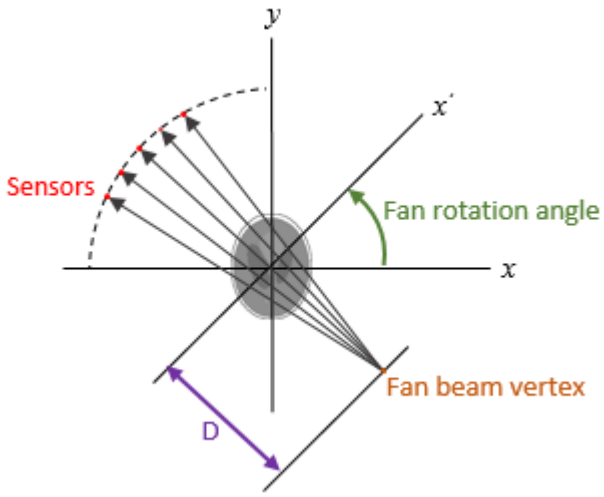

Figure 1.13: Equiangular fan beam geometry. Equiangular rays are directed from the pointsize source to the sensors in the detector. D is the distance from the radiation source to the origin of the coordinates system.

For the tomographic reconstruction of these images, the simple backprojection of parallel beam tomography now becomes a weighted backprojection. The steps of the equiangular rays fan beam backprojection algorithm are the following [8]:

1. modification of the acquired projections, taking into account the geometry of the detector.

$$P_{theta}(n\alpha)' = P_{theta}(n\alpha) \cdot D \cdot cos(n\alpha) \tag{1.20}$$

where $P_{theta}(n\alpha)'$ and $P_{theta}(n\alpha)$ are rispectively the modified and the original projections, D is the distance between the radiation source and the origin of the system, n is a positive integer and α is the angle between the equiangular rays;

2. Convolution of each modified projection with a specific function that depends on $n\alpha$, to generate the corresponding filtered projections;

3. A *weighted* backprojection of each filtered projection along the fan. While for the parallel case, the filtered projection is backprojected along a set of parallel lines, for the fan beam case the backprojection is done along the fan, converging lines, as shown in fig.1.14.

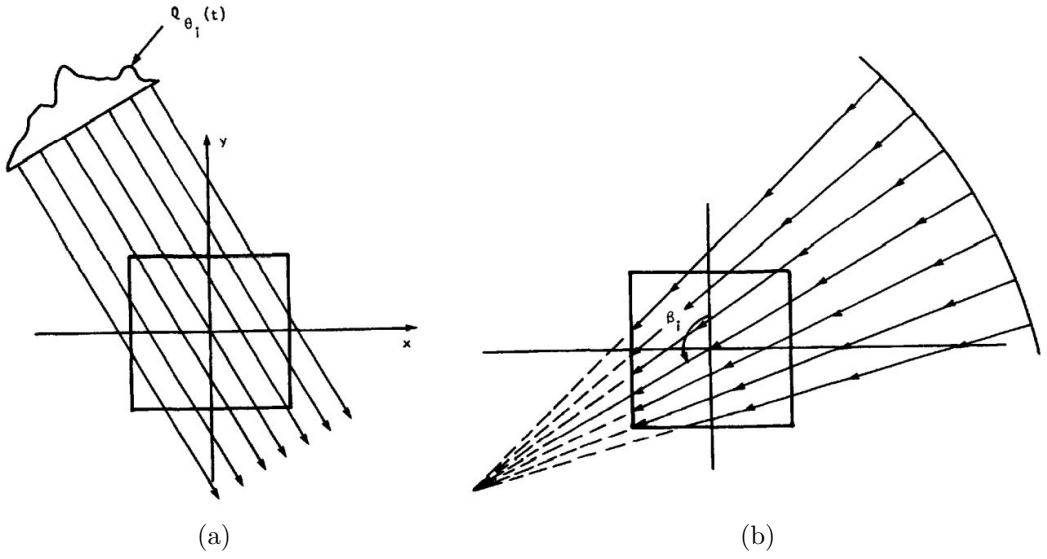

(a) (b)

Figure 1.14: (a) Parallel beam backprojection along parallel lines. (b) In fan beam case the backprojection is performed along converging lines. [8]

A convolution-backprojection method is also deduced for the direct reconstruction of a three-dimensional density function from a set of two-dimensional projections. It is called cone beam reconstruction and it is a generalization of the two-dimensional equiangular rays fan beam algorithm. Now, instead of illuminating a slice of the object with a fan of rays, the entire object is illuminated with a cone-shaped beam produced by a point source and the radiation flux is measured on a plane. One of the filtered backpropagation algorithms for three dimensional reconstruction is the FeldKamp algorithm, based on filtering and backprojecting a single plane within the cone. Eeach elevation in the cone is considered separately and the final three dimensional reconstruction is obtained by summing the contribution to the object from all the tilted fan beams, like the one shown in fig.1.15. For more technical details, consult [8] or [9].

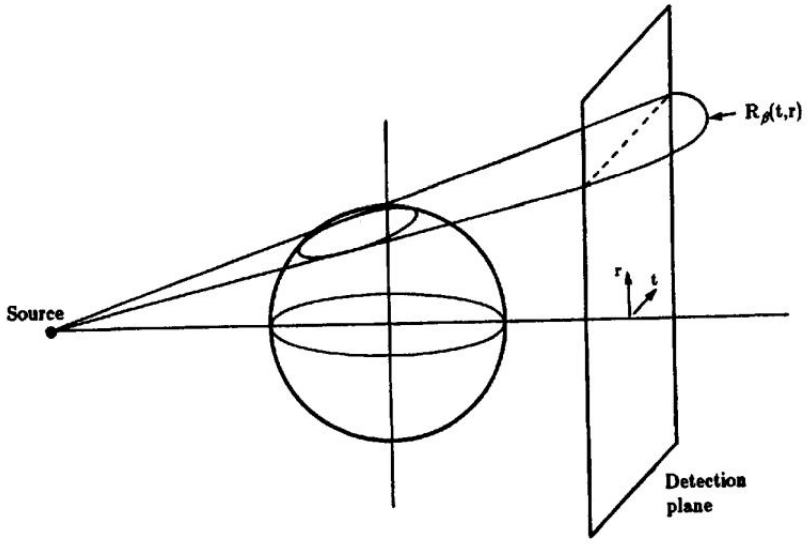

Figure 1.15: The illustration of a single fan beam, composing the cone radiation beam that interacts with the analyzed object (a sphere in this case). In cone beam projections the detector measures the radiation flux over a plane. [8]

Chapter 2

Neutron Tomography for Cultural Heritage

The analysis of cultural heritage objects requires the usage of non-invasive and non-destructive methods , because of their material as well as immaterial value. The term 'cultural heritage object' does not have a very sharp definition and hence comprises a vast variety of topics, from prehistoric archaeological findings to pieces of modern art. Besides the largely varying background and provenance of the objects, there is a broad diversity of questions arising with the objects and thus reasons that necessitate a closer inspection. These may vary from an ascertainment of the actual condition of the object (necessary for conservative measures) to questions on the inner structure and build-up of the object (such as the materials used and information on the manufacturing processes) or the search for features or ancient artefacts hidden within the object [20]. Hence, it is of great importance to gain a close inspection of cultural heritage objects by transmission imaging techniques, using non-destructive and non-invasive methods that do not affect the integrity of the object studied.

While X-ray imaging is often sufficient for such investigations, there are numerous cases where the method reaches its limits. Here, the complementarity sometimes provided by neutron imaging with respect to X-ray imaging can provide new insights into the studied object. The better transmission for metals and the higher contrast for organic materials can already be exploited in the simple neutron radiography mode, but even more advanced are the neutron tomography methods, where virtual sections through the objects

at arbitrary positions enable deeper perceptions and also dimensional determinations in full 3D. Since x-rays and neutrons show different interaction behavior with matter, the two imaging methods, that sometimes show complementary information, are usually combined in order to perform an exhaustive examination of the studied object.
In this chapter a comparison between neutrons and x-rays interactions with matter and some neutron tomography practical examples in cultural heritage field are reported. Finally some neutron imaging facilities are presented.

2.1 Comparison between neutrons and X-rays

X-rays are electromagnetic waves, while neutrons are uncharged particles, hence they show different behaviours interacting with matter. As it has been explained in the first chapter, sections 1.1.1 and 1.1.2, X-rays interact principally with the electrons in the atomic shell of the elements composing the sample, while neutrons interact mostly with nuclei. Hence X-rays attenuation coefficient is almost linearly dependent on the atomic number of the crossed element, while for (thermal) neutrons is not possible to determine such trend. Fig. 2.1 compares mass attenuation coefficients of thermal neutrons and 100 keV X-rays (a typical energy used in imaging) and clearly demonstrates the complementarity of neutron and X-ray imaging for a broad range of materials.
Another usefull representation of the different and sometimes opposite attenuation capability of neutrons and X-rays is reported in fig.2.2, where gray levels obtained by thermal neutron imaging and by X-ray imaging are shown for all the elements.
It is evident that, while neutrons feature high contrast for Hydrogen and thus for organic materials, accompanied by good transmittance for most metals, X-rays show high contrasts for metals and good transmittance for materials consisting of light elements. These different behaviours let neutrons and X-rays be almost complementary and this complementarity is reflected in the images acquired with the two techniques.

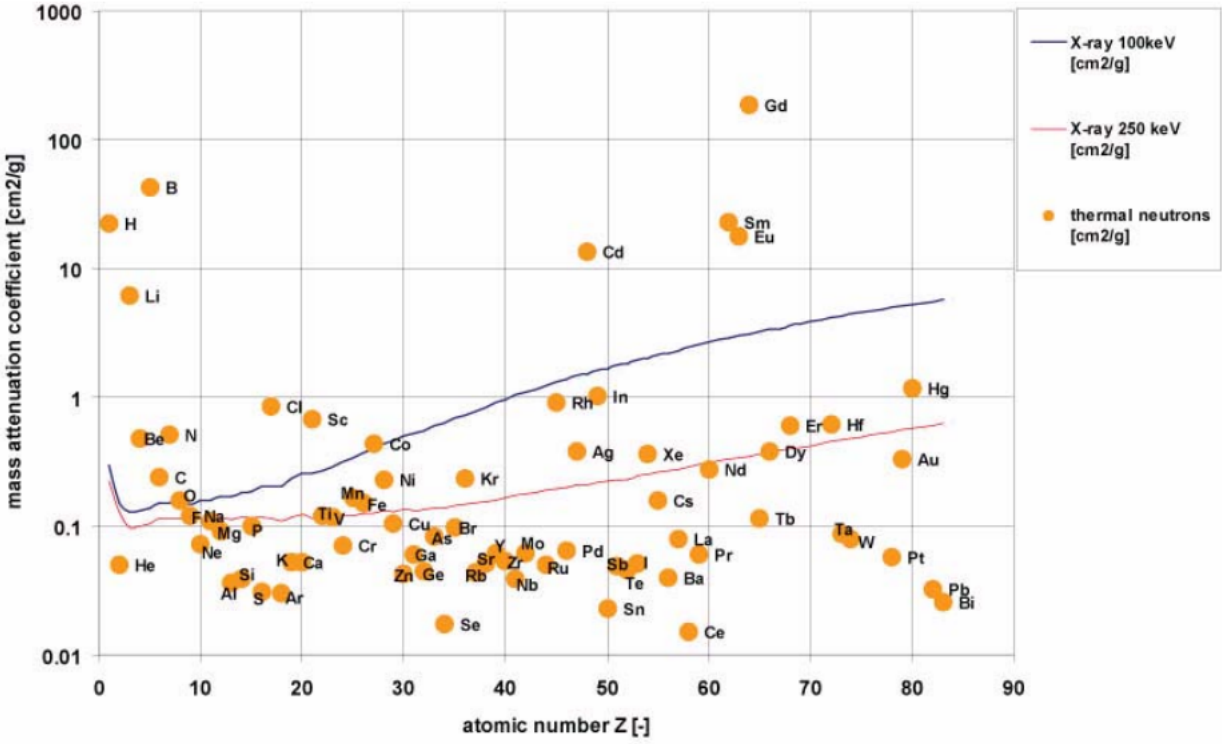

Figure 2.1: Mass attenuation coefficients for thermal neutrons and 100 keV and 250 KeV X-rays for the elements.

Now, let's consider the samples analyzed with neutron or X-ray imaging techniques in cultural heritage field. Cultural heritage objects represent a very versatile group with respect to the composition. They most often represent composite materials, which can consist of a large variety of different constituents such as metals, ceramics or organic material (wood, textiles etc.). To this, add further substances related to the aging (e.g. corrosion products), conservation treatments (biocides, consolidants etc.) or storage (e.g. moisture). Neutrons easily penetrate thick layers of metals like Pb, Fe and Cu where standard X-ray imaging even with energies of several hundreds keV would fail. Hence, in this context, the two radiations appear to be complementary in the case of non-destructive radiography or tomography investigations [19], giving the possibility to visualize many more features of the samples and aswer a larger amount of questions about them.

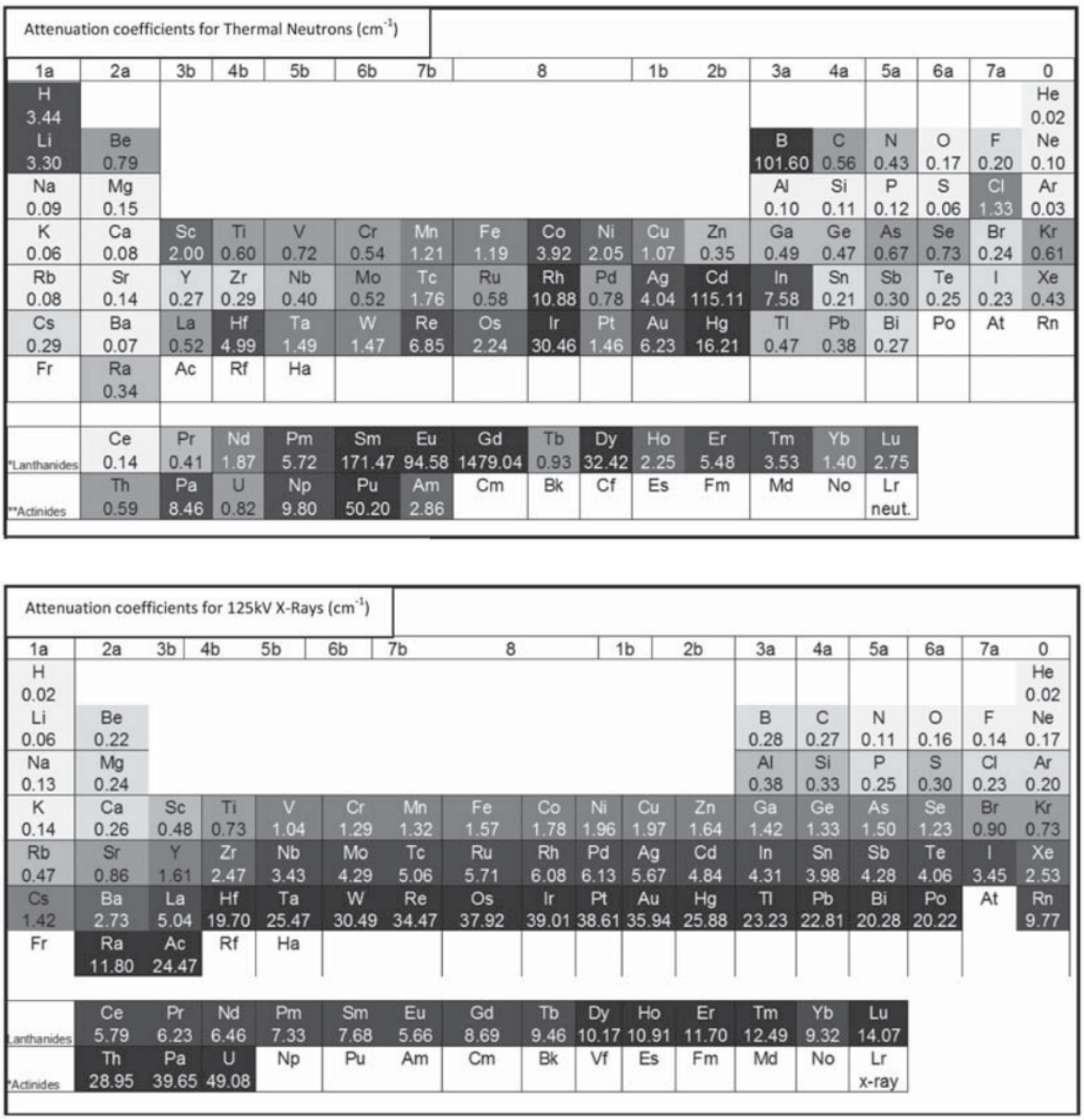

Figure 2.2: The attenuation coefficient for thermal neutrons (on the top) and for 125 kV X-rays (on the bottom) represented in gray levels on the periodic table of elements.

2.2 Case-studies

In this section, some practical applications of neutron tomography (NT) are reported. The first example is the study by means of neutron tomography of Renaissance bronze objects from the Rijksmuseum (Amsterdam) collection and lead ingots from ancient roman shipwrecks found near Sicily (Italy), performed by E.H. Lehmann et al. [18]. The aim of the analysis was to gain information about the inner composition, the manufacturing process and the conservation status from the inside of the 16th century bronze statues. An experimental setup similar to the one schematized in fig. 3.1 was placed at the end position of the thermal neutron imaging station NEUTRA2 at the Paul-Scherrer-Institute (PSI), Switzerland, where the neutron beam had a spectrum with mean energy of 25 meV. Some results are here reported through figures 2.3, 2.4 and 2.5. Each of them represents the statue with the corresponding photo, homogeneity map and cross section map derived by neutron tomography. For more results see [18].

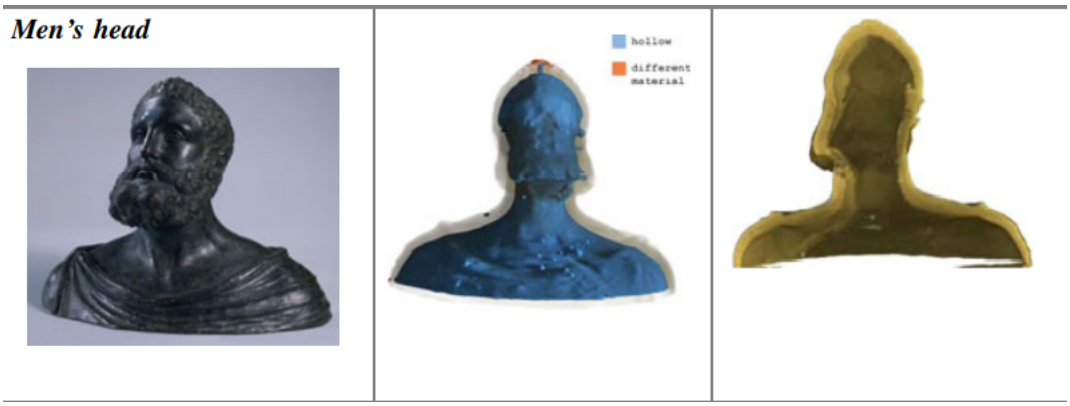

Figure 2.3: Bust of a man, Padua or Ravenna,c.1505-1525, height 15,5 cm, Rijksmuseum, Amsterdam, inv. nr. BK-NM-12080. ***On the left*** *the photo of the statue,* ***in the middle*** *the homogeneity map and* ***on the right*** *the cross section map. The inner volume of the object is highlighted in the middle image (in blue), indicating the regions of the inner surface and some empty pores in the bulk. This is compared to the virtually cutted object on the right side. Obviously, on the heads peak some other (sealing?) material (in red) can be found closely connected with the filling channel remained in that region. Video:* `https://youtu.be/_mMSrHXzPb8`*. (source [18])*

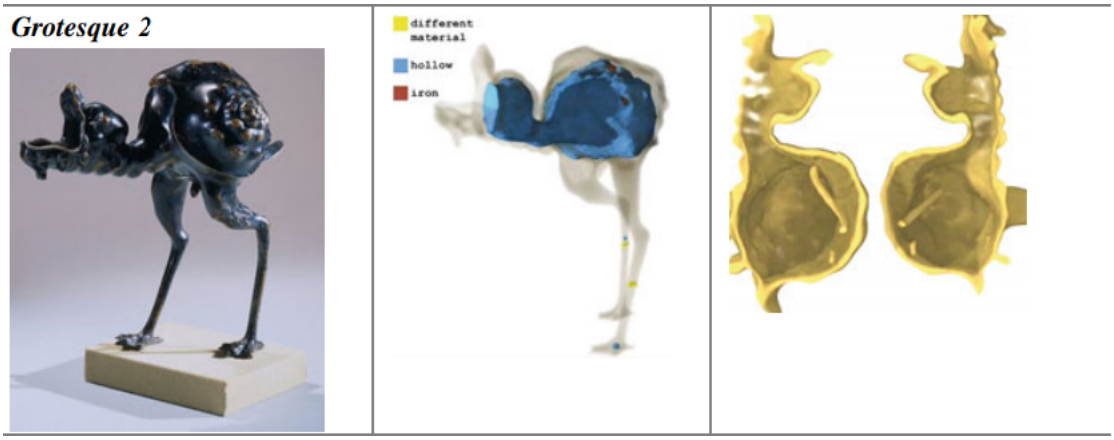

Figure 2.4: Grotesque Animal, Amsterdam or Zwolle, cast 18th century?, height 17 cm, Rijksmuseum, Amsterdam, inv. nr. BK-16127. The empty space of this hollow casted sample is shown in the middle image (in blue). The inner surface and some stabilizing wires can be seen in the sections in the right figure. Some iron traces (in red) and different materials (in yellow) can be seen in the transparent structure in the middle image. Video: `https://youtu.be/F5gud6Mql7U`. *(source [18])*

Figure 2.5: Whereas the lower figure is cast hollow (in blue), the 'upper' body is filled with another material (in red), probably ceramics from the casting process; the tomography data show some outer damages of the lower figure, e.g. at the knee (middle image). The sections through the bodies (right image) show in detail the hollow areas, the remaining casting residuals and the non-homogeneities in the metal structure Video: `https://youtu.be/WRPBFJnb5y8`. *(source [18])*

A second example is the investigation of the content of ancient Tibetan metallic Buddha statues by means of neutron imaging, performed by E.H. Lehmann et al. [19]. Ancient metallic Tibetan Buddha statues are precious religious and cultural objects. They need to be treated with care and with respect. Without their inner organic content remaining undisturbed, they have no symbolic meaning and no religious power. In fact, Buddhists believe that it may be of negative influence or even dangerous to keep a statue if the inner content has been disturbed or removed by opening the metallic enclosure. We know about the inner contents of metallic Tibetan Buddha statues from at least two sources: accidental or unscrupulous opening, and the ritual text used for consecration. An essential piece is a central wooden stick called *'tsog-sin'*, literally 'life-stick' or 'soul-pole', sometimes compared to the human backbone. In addition, there are always Tibetan Buddhist religious texts on paper or silk, wrapped around the pole and also rolled up in separate bundles. Some statues contain series of numerous small paintings.
The experiment was performed at NEUTRA facility, at the beam port 32 for thermal neutrons, in the spallation neutron source SINQ, the Swiss national facility for research with neutrons. In addition to its neutron performance, the NEUTRA station is equipped with a strong X-ray source with high voltages up to 320 kV. Therefore a comparison between neutron and X-ray imaging (X-rays with high voltage, 150 kV) was perfomed.
Four bronze statues, whose data are reported in the table in fig.2.6, were investigated.

	A	*B*	*C*	*D*
Name of the object	Buddha Sakyamuni	Buddha Sakyamuni	Buddha Amitayus	Buddha Akshobhya
Origin	Bhumisparsa Mudra, West Tibet	Bhumisparsa Mudra, Central Tibet	Central Tibet	Central Tibet
Manufactured	14th–15th century	End 15th century	17th century	17th century
Height (cm)	17.1	17.2	19.5	20
Largest diameter (cm)	13.3	12.5	13.5	13.3
Weight (g)	769	1119	1042	1322
Material	Bronze	Bronze	Bronze	Bronze

Figure 2.6: Data of the observed Buddha statue[19].

Here the results for statue A are reported. For more details see [19].

(a) (b) (c)

Figure 2.7: Buddah sculpture A reported in table 2.6 photo (a), its neutron image (b) and its X-ray image (c). (source [19])

Fig.2.7 shows the photo, the frontal neutron and X-ray radiographies of the statue A. It is apparent that, while X-ray image shows more details of the external bronze surface of the sample, with no chance of internal investigation, neutron radiography allows the visualization of the filling materials.
There is a wooden stick in the middle, which is surrounded by a rolled textile or paper layer and fixed with a cable. Flowers or other plants with buds have been filled in the lower part of the sculpture.
In fig. 2.8, some visualization options of sample A neutron tomography are presented. In these 3D renderings, contrast variation can be made more precise and suitable, when only one slice is involved. Hence, it becomes much easier to distinguish separate materials and structures with the same attenuation coefficient and hollow areas can be determined much better too. This visualization confirms the presence of the wooden stick (*'tsog-sin'*), the rolled paper and the wire around, whereas the plants on the ground have reduced contrast. Moreover it becomes clear that there are residual amounts of ceramic remains in broken pieces somewhere inside the bronze cover.

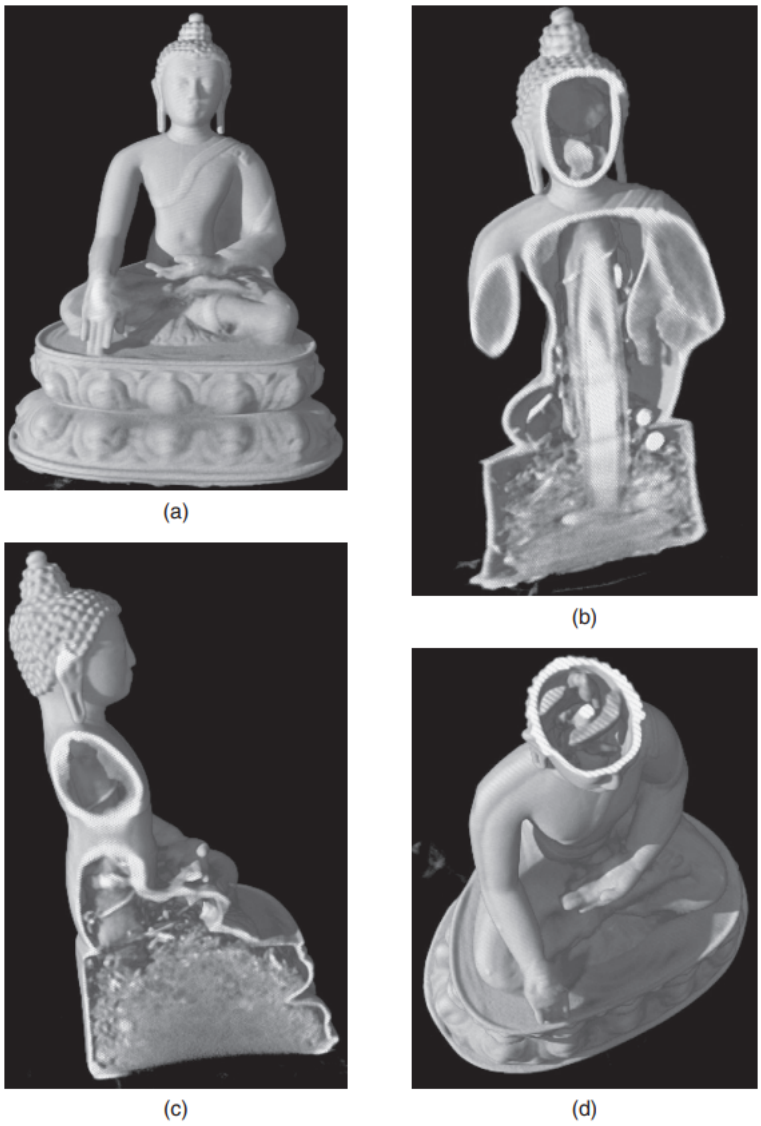

Figure 2.8: Some 3D volume rendering to show and to slice the sample A virtually at relevant positions. In (a) the external surface, in (b) and (c) a slice representing the internal filling, in (d) a slice that shows the filling in the head of the statue A. (source [19])

The analysis computed on statue A, and even on the other three remaining statues, allowed to confirm the ritual requirement and indicated that the statues were 'empowered and thus fit for ritual and meditation'. Positive contribution was given to the important question of whether the statues were genuine or not.

2.3 Neutron Facilities

In the following table some neutron imaging facilities are reported. For a more complete list, consult the site of International Society for Neutron Radiography (ISNR) [21].

Country	Site	Institution	Facility	Neutron Source	Spectrum	Power (MW)	Status
Australia	Sydney	ANSTO	DINGO	OPAL reactor	thermal	20	operational
Germany	Munich-Garching	TU Munich	ANTARES	FRM-2 reactor	cold	25	operational
Germany	Munich-Garching	TU Munich	NECTAR	FRM-2 reactor	fast	25	operational
Germany	Berlin	HZB	CONRAD	BER-2 reactor	cold	10	operational
Hungary	Budapest	KFKI	NRAD	WWS-M reactor	thermal	10	operational
Japan	Kyoto	Kyoto University	imaging beamline	MTR reactor	thermal	5	standby
Japan	Tokai	JAEA	RADEN	JPARC spallation	cold	0.5	operational
Korea	Daejon	KAERI	imaging beamline	HANARO reactor	thermal	30	operational
Russia	Dubna	JINR	imaging beamline	IBR-2M pulsed reactor	thermal	2	operational
Switzerland	Villigen	PSI	NEUTRA	SINQ spallation	thermal	1	operational
Switzerland	Villigen	PSI	ICON	SINQ spallation	cold	1	operational
UK	Oxfordshire	Rutherford Lab	IMAT	ISIS spallation	cold	0.3	operational
USA	Gaithersburg	NIST	BT-2	NBSR reactor	Thermal	20	operational
USA	Gaithersburg	NIST	NG-6	NBSR reactor	Cold	20	operational
USA	Oak Ridge	ORNL	CG-1D	HFIR reactor	cold	85	operational
South Africa	Pelindaba	NECSA	SANRAD	SAFARI reactor	thermal	20	standby

Table 2.1: List of the "state-of-art" of the neutron imaging facilities, reactors and spallation sources based.

Chapter 3

Acquisition system and its characterization

3.1 Imaging system setup

A typical setup for tomographic imaging for cultural heritage is shown in fig.3.1.

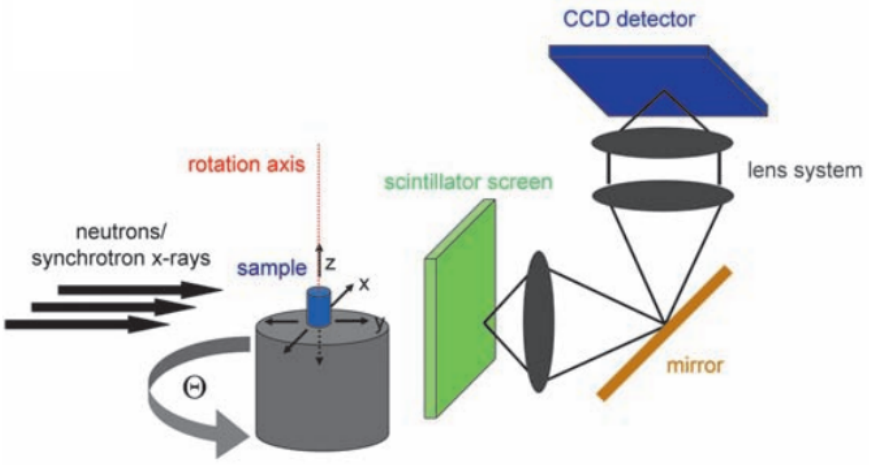

Figure 3.1: Scheme of a tomography experiment: radiation is directed on a rotating sample; the attenuated beam interacts with a scintillator screen and is converted into visible light; the latter is reflected by a 45° inclinated mirror, focused by lenses and detected by a CCD camera.

It consists of a source of radiation (X-rays or neutrons), a rotation and translation stage, a scintillator screen, optics, including a deflecting mirror and lens, and a charged coupled device (CCD) camera. The incident beam interacts with the sample, placed on the stage, being attenuated. The attenuated radiation interacts with the scintillator, which converts the radiation particles in visible light. The latter is deflected with an angle of 45° by the mirror and finally collected by the CCD camera. Softwares on a computer elaborate the acquired data in order to obtain images for the tomographic reconstruction.

3.1.1 Radiation sources

X-ray sources

X-rays can be created in two ways: either by ejecting core electrons from atoms and letting other electrons fall into the holes created and emit X-ray photons, or by accelerating or decelerating free charged particles.

- *X-ray tubes*: they traditionally exploits both mechanisms. By bombarding a metal target with electrons, holes in low-lying atomic levels of the target atoms are created that are then filled by electrons of higher atomic levels. In some cases this gives rise to characteristic (fluorescence) radiation, in other cases de-excitation is radiationless. Other electrons are simply decelerated in one or more steps and release their kinetic energy as electromagnetic radiation giving rise to the typical continous *bremsstrahlung*. The resulting radiation has a spectrum that is the superposition of a broad distribution of energies with a cutoff at the energy of the bombarding electrons and some peaks related to the target material (fig.3.2)

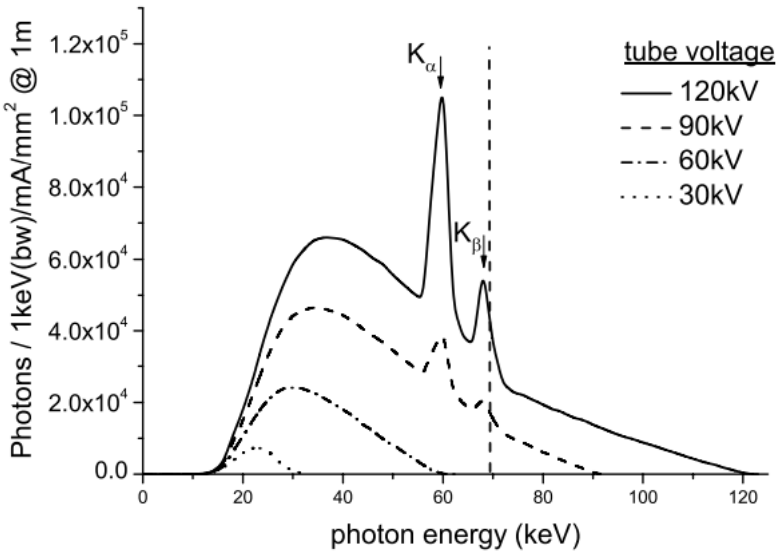

Figure 3.2: Spectrum of a X-ray tube with a tungsten anode for 4 different tube voltages. The broken line denotes the absorption edge of tungsten at almost 69.5 keV. (source [1])

- *Synchrotrons and storage rings*: synchrotron radiation is created by accelerating free particles in high vacuum. By the laws of electrodynamics this acceleration leads to the emission of electromagnetic radiation. Magnetic fields are used to force the particles onto a desired closed orbit to obtain a source of continous radiation. The radial acceleration associated with the change of direction then generates radiation. Three generations of synchrotron sources can be recognized.
  In the first one, x-ray beams were principally used for particle-physics experiments. In the second generation, as shown in fig.3.3, instead of a circular orbit, a polyhedral path is chosen on which bending magnets change the particle's direction, after which they fly on a straight section again before entering the next bending device. The advantage is the production of X-rays of a higher energy and intensity.

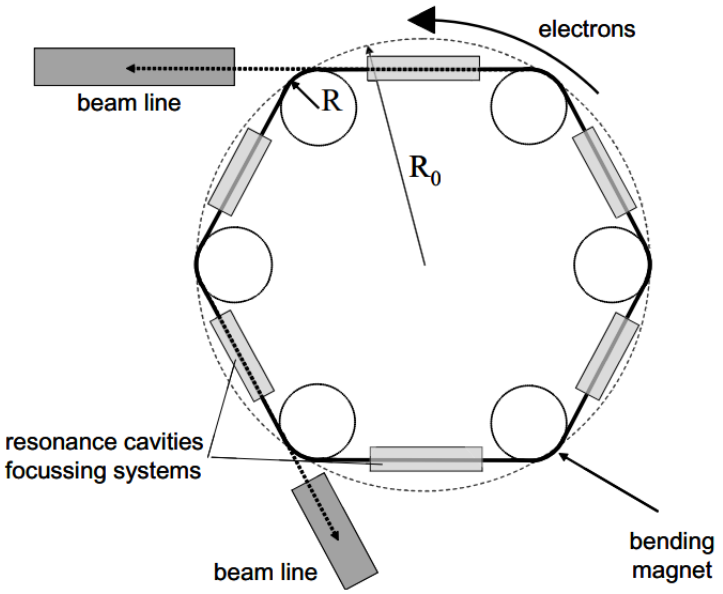

Figure 3.3: Scheme of a second generation synchrotron radiation source. (source [1])

In third-generation synchrotron sources, radiation is created by so-called *insertion devices*, arrays of various magnets that undulate the electron beam many times such that radiation from each curve superimposes. Insertion devices are located in the straight sections between two bending magnets and give rise to a much more brilliant radiation, where *brilliance* specifies the number of photons N emitted per time t from an area A (this is flux) and divides this by the solid angle $d\Omega$ into which the radiation is emitted and then relates it to 10^{-3} of the spectral bandwidth $\Delta\lambda$ of the emitted radiation [1].

Neutron sources

Neutrons are abundant in nature since all atoms, except hydrogen ^1H, contain neutrons. However, as the binding energy of neutrons within the nucleus is high, some MeV per nucleon, ejection of neutrons from nuclei requires high energies. In practice, one has to bombard suitable nuclei with nucleons or ions and initiate nuclear reactions. As a result, neutrons and other particles will be ejected as free particles [1]. Neutron sources are the following:

- *Radioactive sources*: Radium (Ra) or Polonium (Po) are used to emit α-particles (^4He-nuclei) of sufficient energy and to let these particles hit other nuclei. One useful reaction is

$$^4He +^9 Be \rightarrow^{12} C + n + 5.7MeV$$

  where the kinetic energy released is distributed over the reaction products.
  The neutron production rate of this system, however, is quite low, typically of the order of 1 x 10^7 n/s for a sample of 1g mass.

- *Accelerator-based sources*: here accelerating protons (^1H) or deuterons (^2H) to a few hundred keV initialize nuclear reactions. They can be

$$^2H +^3 H \rightarrow^4 He + n + 17.6MeV$$
$$^2H +^9 Be \rightarrow^{10} B + n + 4.3MeV$$

  The second reaction is especially suitable for accelerator-based neutron sources.

- *Reactors*: most neutron sources used for imaging are dedicated research reactors, small nuclear reactors that are primarily used to produce neutrons, unlike nuclear power reactors, which are larger and used to generate electricity.
  Fission of nuclear fuel, usually ^{235}U, takes place when ^{235}U nuclei are hit by slow neutrons (few meV of energy). Many possible reactions like the following can occur:

$$n_{slow} +^{235} U \rightarrow^{144} Ba +^{89} Kr + 3n_{fast} + \gamma + 200MeV$$

  where fast neutrons have an energy of few MeV. In order to obtain a chain reaction, fast neutrons must be thermalized by a moderator, usually light water (H_2O) or heavy water (D_2O), or graphite, to be used as projectiles in the next reaction cycle. Thermalization is a series of scattering events of fast neutrons with light nuclei of the moderator that finally lead to an adjustment of neutron energies to the range of the moderator temperature.
  Surrounding the moderator there may be reflector materials that do not provide much moderation but scatter or reflect some of the fast neutrons back into the moderator to enhance the thermalized neutron flux output [4].

Neutrons coming out of the reactor core are directed to the measurement stations through flight tubes. The extracted beam is *polychromatic*, since it contains a spectrum of neutron energies. Some flight tubes have been constructed so as to allow fast fission neutrons to fly out of the reactor and to be used, but usually the beam tubes are oriented tangentially to the core to avoid too many fast neutrons (and γ-rays) in the beam.

Special moderators, *cold sources* like liquid hydrogen or deuterium or *hot sources* like carbon heated by γ radiation from the reactor, can be strategically placed in order to shift the neutron energy spectrum to either slightly lower energies (producing *cold neutrons*) or higher energies (producing *fast neutrons*). Typical thermal and cold neutron spectra is shown in fig.3.4 where the energy shift is due to the temperature of the moderator.

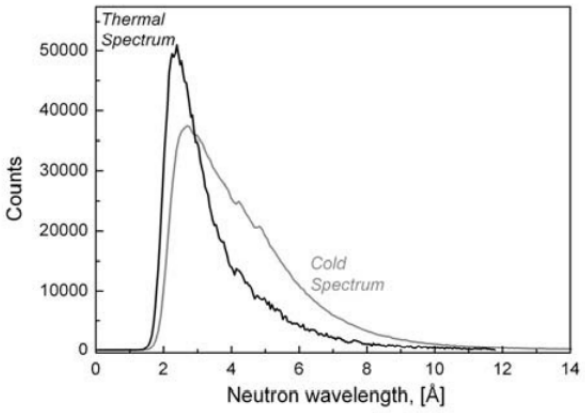

Figure 3.4: Spectral distribution of neutron energies at the research reactor FRM-I in Munich. Cold and thermal spectra are shown.

- *Spallation sources*: with this technology neutrons are produced by bombarding a target made of a heavy material such as lead (Pb), tungsten (W) or ^{238}U with high-energy protons (up to 1 GeV). Each proton can produce 30 neutrons. The proton beam is usually pulsed at repetition rates of a few tens of Hz and the corresponding neutron pulses therefore have a similar time structure. Spallation technology has not been brought to an inherent technological limit yet and therefore the future of neutron production for research seems to lie in such sources [1].

Neutron beam requires a further preparation as it comes out from flight tubes.
It has to be collimated and focused by collimators or neutron optical components, it could be made monochromatic, through the usage of choppers, velocity selectors or single crystals, and it could be polarized, with polarizing filters.

3.1.2 Scintillator

Scintillator is the imaging system component that converts the attenuated particles coming from the object under study in visible light. The latter will be detected by the CCD camera. A scintillator can be organic or inogranic, depending on the composing material(s), and it has to be properly chosen according to the type of incoming radiation particles (X-rays or neutrons). General requirements for a good scintillator are:

- high scintillation and detection efficiency;
- linear conversion between the energy deposited in the scintillator by the radiation and the light emitted;
- transparency of the scintillator material to the fluorescence light emitted;
- as short as possible light emission time;
- well-matching between the emission wavelenght and the CCD sensitivity curve;

Inorganic scintillators, like Cesium iodide (CsI), bismuth germanate (BGO), zinc sulfide (ZnS) or glass scintillators, are insulating material made up of crystals of inorganic salts containing small impurities as activators for luminescence process (through the deexcitation from luminescence centres in the medium). Organic scintillators, like plastic scintillators or pure organic crystals, are hydrocarbon compounds that contain benzene ring structures and the fluorescence is produced from transitions of the free valence electrons of the molecules. For X-ray CT, CsI(Tl) or Gadolinium Oxysulfide $Gd_2O_2S : Tb$ scintillators are used, for example, in transportable facilities for cultural heritage investigation developed by the INFN-CHNet (cultural heritage network) X-ray tomography laboratory of Bologna [11]. The scintillator is positioned in a light-tight box, as shown in fig. 3.5 and optically coupled with a CCD camera, through a lens and a 45° mirror. In this configuration, X-rays interact with the scintillator, producing visible-light photons,

which are deflected by the mirror and directed on the CCD. This design avoids radiation damages caused by the direct irradiation of the CCD.

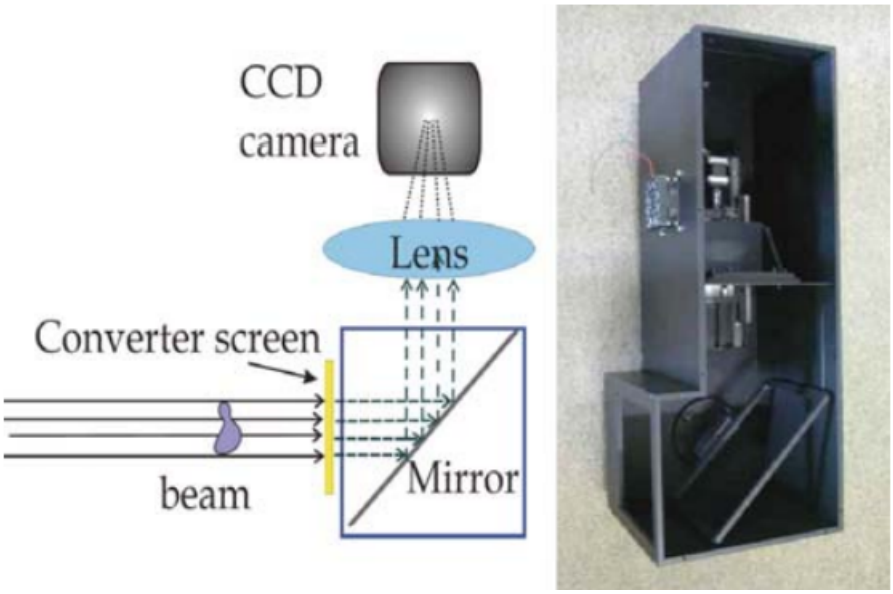

Figure 3.5: Left: radiation beam attenuated by the interaction with the scanned object hits the scintillator screen, is converted into visible light, that is reflected by a mirror, focused by a lens and collected on the CCD of a camera. Right: light-tight box containing the scintillator, the mirror, the lens and the CCD camera.

For neutron CT, the box configuration described above is still used (fig.3.5), but visible light production requires an intermedial step, the conversion of neutrons to charged particles, through nuclear reactions. Charged particles can directly interact with the scintillator, allowing the production of photons with the wavelenght in the visible range. Usually the double conversion, neutron to charged particle to light, is performed using a chemical vapor deposition (CVD) of a mixture of a neutron-absorbing component, such as Litium fluoride (LiF) on a fluorescent compound, like zinc sulfide (ZnS).
The neutron absorption takes place thanks to the ^{6}Li nuclei, according to the reaction:

$$n +^6 Li \rightarrow^3 H +^4 He + 4.79 MeV$$

then the positive ions ^3H and ^4He (α particle), that are the reaction products, interact with the ZnS particles, leading to the emission of visible light.
Development over years has shown that ZnS layers, doped with colour centres (Ag or

Cu) can shift the emitted light wavelenght to the desired one.
The fig. 3.6 shows what happens in a ^{6}LiF+ZnS:Ag scintillator screen.

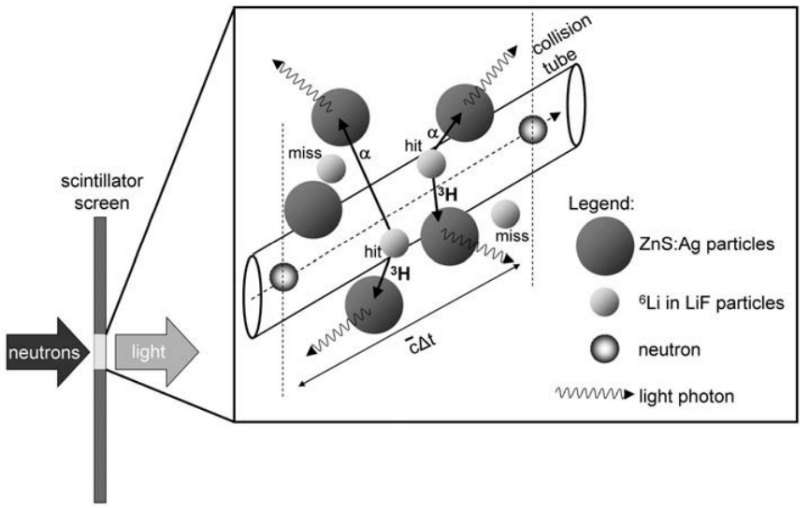

Figure 3.6: Conversion principle of neutron scintillator screens. A neutron with velocity $\bar{c}$ enters the scintillator and is absorbed by a ^{6}Li nucleus present in the LiF converter contained in the scintillator. As a result, ^{3}H and ^{4}He (α particle) reaction products are emitted as positively charged ions that then interact with the ZnS:Ag particles around in a second step, eventually leading to the emission of visible light. (source [1])

The thickness of the LiF compound is a compromise between the need to increase the light output (increasing the thickness) and the requirement of improving the light transmission (reducing the thickness).

3.1.3 CCD camera

The CCD camera is the setup component that captures the image from the light emitted by the scintillating screen through the charge couple device (CCD) technology.
CCD is a mean of capturing an image electronically. It can be classified as an integrated circuit that contains numerous small photo elements that have high sensitivity to light photons. They are the sensors of the CCD, also called pixels and each of them is made by a Metal Oxide Semiconductor (MOS) capacitor. A cross section of a CCD sensor is shown in fig. 3.7.

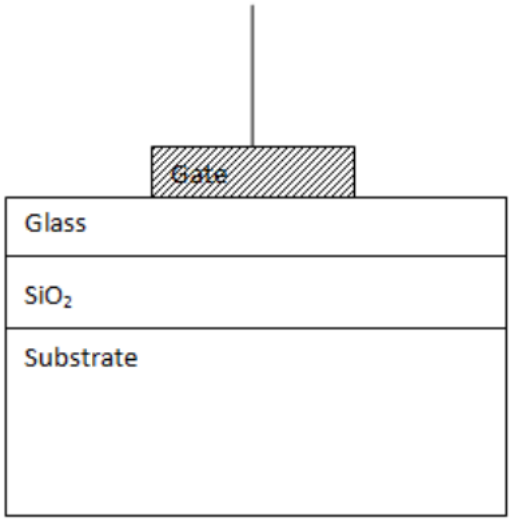

Figure 3.7: Cross-section of a MOS capacitor, CCD sensor. It is composed by four layers: the gate, the glass, the Silicon oxide (SiO_2) and the substrate.

It contains four layers: the first is a gate where the photon strikes, then glass as an insulator, Silicon Oxide (SiO_2) and the substrate.
When light interacts with the surface of the CCD, photons strike the silicon element of the sensor. Here a photon transmits its energy and produces the photoelectric effect. This transmission of energy breaks the covalence band of silicon and causes electrons to freely escape [23]. The number of electrons produced depends on the number of photons striking the glass of the detector. Now, the basic principle of CCD is based on electrical charge transfer between sensors. It takes place in the following way, represented in fig. 3.8: as the voltage adjacent to the electron's pixel is brought high, they begin to migrate in this direction until the voltage in the preceding gate is then brought to zero, or low, thus effectively transferring all the electrons into its neighboring pixel.
Electrons are shifted in two opposite directions on a CCD, *parallel* and *serial* directions. Since the CCD is a squared matrix of pixels, the serial shift directs the electron packets collected in the pixels of the last column of the matrix to the measurements eletronics, where an analog to digital converter measures the voltage created by the packet of electrons and turns this into an electronic signal that can be amplified and digitally saved. Thus, the image can be registrated.

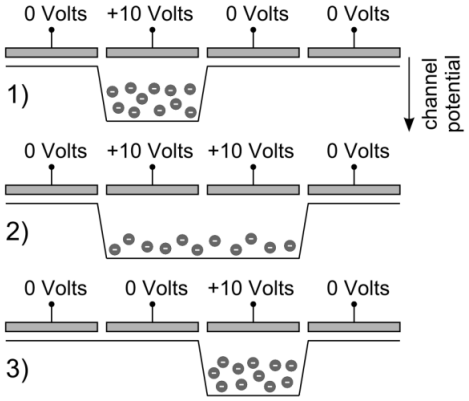

Figure 3.8: Scheme of the electrons transfer with a potential well that change its position depending on the voltage applied to the gates.

CCD devices are characterized by the following parameters:

- Quantum Efficiency (QE): the capacity of conversion from photons into electric signal;
- Lenght of absorption: distance for which 63% of the incoming photons will be absorbed;
- readout noise: it is due to analog to digital (A/D) converter and/or to electronics;
- dark current: thermal noise, composed of electrons liberated by thermal energy and depends on the CCD temperature;
- pixel size: the larger is the CCD pixel size, more charge can be collected;
- binning pixels: bring all the charges of multiple pixels together;
- gain expressed in e/ADU;
- dynamic range: maximum achievable signal divided by the camera noise, where the signal strength is determined by the full-well capacity, that is the amount of charge an individual pixel can hold before saturating, and noise is the sum of dark and read noises.

3.2 Characterization of the detection system

Once a imaging setup has been installed, its performance is evaluated through some characterization indeces. They include:

- the response linearity of the detection system,
- the spatial resolution,
- the signal to noise ratio (SNR) calculated from the acquired images.

3.2.1 Response linearity

The linearity of an imaging system, like the one described in the previous section, is principally influenced by the CCD device, because of the conversion of incident photons to a voltage output signal that will be further digitized for image visualization. The transfer function between the incident photonic signal and the final digitized output should vary linearly with the amount of incident light on the CCD, as expressed by eq. 3.1 [13].

$$digital\,signal = constant \times amount\,of\,incident\,photons \tag{3.1}$$

There is no standard method for measuring or reporting linearity values. One way can be to plot the mean signal value versus the exposure time over the full linear range of the CCD, before reaching saturation.

3.2.2 Spatial resolution

Spatial resolution is the capability of the imaging system to separate two distinct objects that are located close to each other and to make them visible as separate objects. In a complex imaging system composed by several devices, the overall spatial resolution will be the combination of the components resolutions (radiation source, scintillating screen, CCD camera, optics, computer monitor, etc.).
Some possible spatial resolution degradation factors can be:

- a bad coupling between the scintillator screen and the CCD camera,
- an improper thickness of the scintillator that causes a spread of radiation,

- a large detector pixel size (undersampling),
- a deviation of the radiation beam from parallelity.

Spatial resolution of an imaging system is usually expressed by the so called *Modulation Transfer Function (MTF)*. It represents how much contrast of the original object is mantained by the detector, in other words how faithfully the spatial frequency content (modulated signal) of the object gets tranferred to the image [14].
MTF, defined in frequency domain, is the Fourier transform of a system response function, that, convoluted with the object function, gives the output (acquired) image:

$$I(x,y) = O(x,y) * PSF(x,y) + \epsilon_{noise} \tag{3.2}$$

Here, $I(x,y)$ is the acquired image, $O(x,y)$ is the object function, $PSF(x,y)$ is the Point Spread Function, that is the response of the imaging system to a point object, ϵ_{noise} is the contribute of further deteriorating noise to the output image and $*$ represents the convolution. In this equation, the PSF can be replaced by the Line Spread Function (LFS), that is described below.
The PSF would be a δ-function for a perfect imaging system, but imaging artifacts lead to a deviation from this ideal shape, making the latter more Gaussian.
This means that an input "point signal" undergoes a sort of 2D gaussian blurring, given by the shape (width) of the PSF, as shown in fig.3.9.
A similar fuction to PSF is the Line Spread Function (LSF), in the sense that it describes the same spatial features, but in this case the image of an ideal line is used instead of a point (fig.3.10).

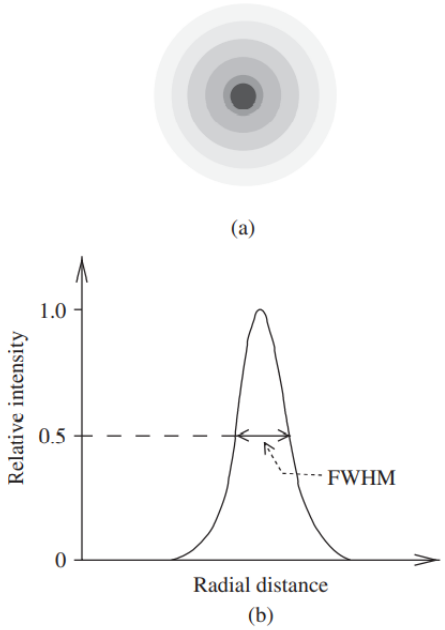

Figure 3.9: (a) Image of a point made by a pixel detector. (b) PSF of the image in (a). FWHM is the width of this function at exactly half the full amplitude. (source [14])

It is possible to demonstrate, as in [15], that:

$$FWHM = \frac{2}{\lambda} \tag{3.3}$$

where $FWHM$ is the width of the LSF at half of its full amplitude and λ is called "resolution parameter", hence low FWHM means high resolution of the system.
The Edge Spread Function (ESF), intended as a superposition of infinite line spread functions, is defined because it can be computed with an experimental easier configuration, a rectangular object place in front of the detector, as shown in fig. 3.11.
A relation between LSF and ESF exists:

$$ESF(x) = \int LSF(x)dx \tag{3.4}$$

or equivalently

$$LSF(x) = \frac{d}{dx}ESF(x) \tag{3.5}$$

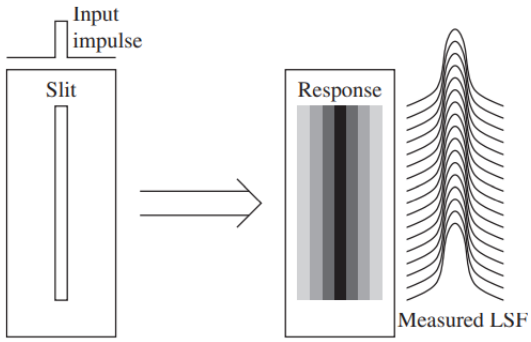

Figure 3.10: The LSF from a thin line can be thought to consist of a large number of PSFs at closely spaced points on the line. On the left, the line input. On the right the response image and the measured LSF. (source [14])

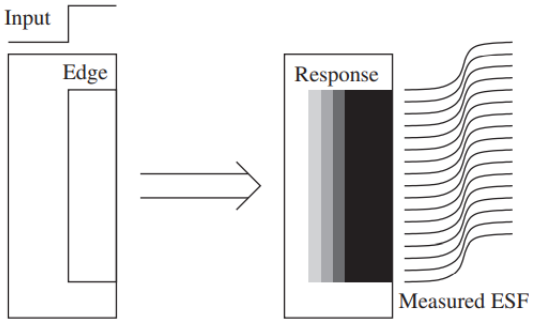

Figure 3.11: On the left the rectangular object with sharp edges. On the right the response of imaging system and the measured ESF. (source [14])

Modulation Transfer Function is inherently related to the various spread functions discussed above [14]. In fact, MTF can be defined as the modulus of the Fourier transform of the LSF, that is,

$$MTF(\nu) = |FT\{LSF(x)\}| = \left| \int_{-\infty}^{+\infty} LSF(x) e^{-i2\pi\nu x} dx \right| \tag{3.6}$$

where ν is the spatial frequency, x is the spatial distance and FT represents the Fourier Transform. Fig.3.12 shows an edge function with the derived LSF and the calculated MTF, where the percentage of transferred contrast is plotted as a function of the spatial frequency expressed in lp/mm (line pairs per mm). Typical values for spatial resolution

characterization are the lp/mm at 10% or at 5% of the MTF.

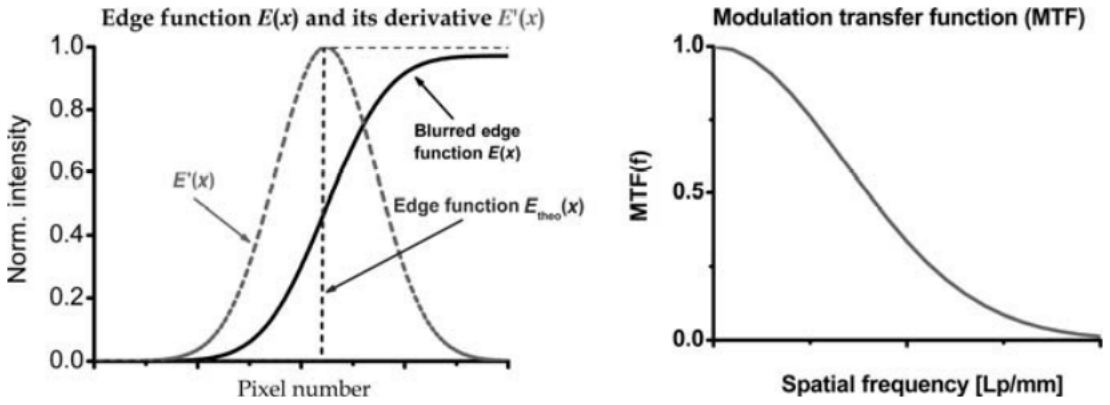

Figure 3.12: On the left, the representation of an ideal edge funtion (dashed line), the blurred edge function (plain line) and its derivative corresponding to the LSF ($E'(x)$, dashed curve). On the right, the MTF calculated with these data.

3.2.3 Signal to noise ratio

Gray level variation in the acquired images represents noise inherent the imaging system. It can be *statistical* or *electronic* and some noise sources are:

- statistical fluctuations of the incident radiation flux (in scintillator and CCD chip),
- statistical fluctuations of the radiation absorption and charge pair production (in CCD camera),
- thermal noise.

The term signal-to-noise ratio, as the name suggests, is the ratio of the signal to the total noise [14]. It can be calculated, considering an image acquired turning on the radiation and without any sample in front of the detector (flat image), as the ratio between the mean signal of the image and the corresponding standard deviation. If one takes into consideration a set of images acquired with different integration times, hence with a different amounts of incident photons on the detector, it is possible to evaluate if the acquired data are affected by systematic errors, in addition to the unavoidable statistical noise.

In fact, if just Poissonian distributed noise (statistical noise) is present in the image, the mean signal will be proportional to the number of detected photons (N), and the standard deviation (σ) to the square root of the same number. The signal to noise ratio will be expressed by the following mathematical relation:

$$SNR = \frac{mean\ signal}{\sigma} \propto \frac{N}{\sqrt{N}} = \sqrt{N} \tag{3.7}$$

Plotting the SNRs of the set of images previously described, a fitting function $y \propto \sqrt{x}$, with y SNR and x acquisition time, stands for a imaging system where the acquired images will be affected only by statistical noise.

Chapter 4

CH-Net NICHE

INFN-CHNet is the network of the Italian National Institute of Nuclear Physics that develops and applies new instrumentation for the study of Cultural Heritage (CH). This process results in both optimized traditional state-of-the-art and highly innovative detection setups for spectrometric techniques. It has the mission of harmonizing and enhancing the expertise of the Institute in the development and application of analytical techniques for the study and diagnostics of CH. This expertise is distributed in many of the INFN structures throughout the country (twenty INFN laboratories and also institutions with complementary skills to those of INFN, such as restoration centers, university departments and associations) and in some international research centers (currently in the United Arab Emirates, Iran, Myanmar, and Argentina).
Among various experiments, NICHE (Neutron Imaging Cultural Heritage Experiment) is placed at the gate B of the TRIGA reactor of the LENA (Laboratory of Applied Nuclear Energy) Laboratory in Pavia. It aims to create the first thermal neutron imaging system (radiography and neutron tomography) in Italy, specifically designed for the diagnostics of CH, to provide important information in many case studies, in particular in archaeological and artistic fields. The experimental project will continue throughout the year 2022.
In this thesis the characterization of the detection setup and some tomographic results are reported.

4.1 Materials and Methods

4.1.1 Experimental Setup

NICHE experiment has a typical neutron imaging setup, as shown in fig. 3.1 and fig. 3.5. Two photos are reported in fig. 4.1.

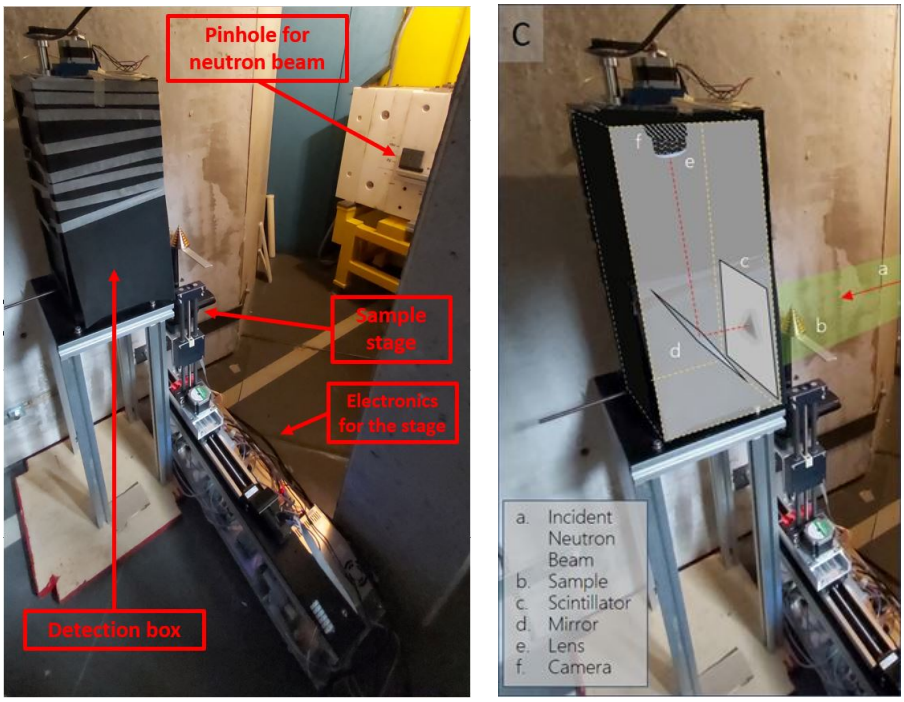

Figure 4.1: On the left, a photo of the experimental setup at NICHE facility station, at TRIGA MARK II reactor (LENA), in Pavia. On the right, a magnification picture of the same facility setup, in which a scheme showing the arrangement of the inner components of the detection box is shown.

Here the list of the components:

- **TRIGA MARK II reactor** at LENA in Pavia. It is the neutrons source. TRIGA MARK II is a pool-type reactor cooled and partly moderated by light water, with the fuel consisting of a uniform mixture of uranium and zirconium hydride. It is licensed for operating at 250kW power in steady state. The reactor core is shaped as a right cylinder and contains 90 slots, distributed over 5 concentric rings; they can contain either fuel elements, graphite (dummy) elements, control rods or

in-core irradiation channels. The fuel consists of a uniform mixture of uranium (8% wt., enriched 20% wt. in ^{235}U), zirconium (91% wt.) and hydrogen (1% wt.). Core reactivity is governed by three control rods, named Shim, Regulating and Transient; the first two contain boron carbide, while the latter is filled with boron-enriched graphite. A 30cm thick radial graphite reflector surrounds the core while the axial reflector is provided by two graphite cylinders located at the ends of the fuel element itself. The reactor has four vertical irradiation channels and four horizontal irradiation channels. Among the latters, channel B, due to higher thermal-to-fast neutron flux ratio with respect to other channels, is selected as station for the experiment. In table 4.1 the main characteristics of TRIGA MARK II (LENA) reactor are summarized [22], and figure 4.2 shows a photo of the facility.

Description	**Data**
Maximum steady state power	250 kW
Fuel	Uranium zirconium hydride (UZrH) fuel (enriched 20% wt. in ^{235}U)
Moderator/cooling	Demineralized light water
Reflector	Graphite
Control rods	2 (Shim and Regulating) containing boron carbide 1 (Transient) containing boron enriched graphite
Vertical irradiation channels	4 (Central Thimble, Rabbit, Lazy Susan and Thermal Channel)
Horizontal irradiation channels	4 (3 radial channels and 1 tangential channel) + Thermal Column + Thermalizing Column
Max Flux SS, Thermal neutrons	$1 \times 10^{13}(n/cm^2s)$

Table 4.1: Principal features of TRIGA MARK II reactor at LENA in Pavia.

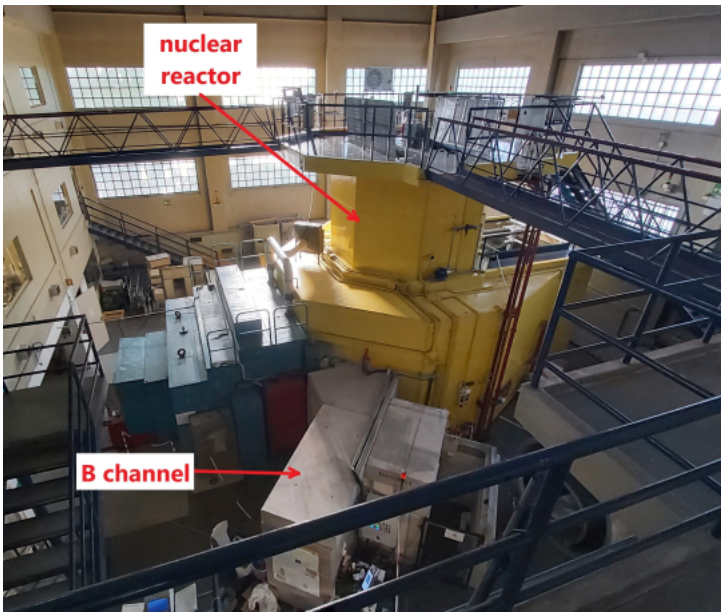

Figure 4.2: Photo of the TRIGA MARK II reactor at LENA in Pavia

- **Filters**. In the beam tube directed from the reactor core to the NICHE station there are a sapphire (Al_2O_3) filter and a bismuth (Bi) filter, in order to filter out γ -rays and fast neutrons from the thermal neutron beam used for the irradiation of the samples.

- A **double shutter** with 5 cm aperture, still in the beam tube, in order to control the irradiation of the sample (radiation ON and OFF according to the opening of the shutter). The MCNP simulated flux at the shutter beam position is 1.62×10^7 n/cm^2s for the thermal component, 3.53×10^5 n/cm^2s for the epithermal component, and 2.11×10^5 n/cm^2s for the fast component. The evaluated gamma flux is 10^6 γ/cm^2s in the range 1-5 MeV.

- A **pin hole** made of boron carbide (B_4C) ceramics placed after the shutter, at the end of the beam tube. It allows the passage of neutrons within its aperture. Two different pin holes are used for different analyses, one with 2 cm aperture and one with 10 mm aperture. Fig. 4.3 shows the pin hole at the end of the beam tube.

Figure 4.3: photo of the pin hole at the end of the beam tube directed from the TRIGA MARK II reactor core to the NICHE station facility at the end of B horizontal irradiation channel.

- A **movable stage** for the positioning of the samples. It can translate and rotate (mandatory for the tomographic analysis), hence making the sample translating or rotating. The movements are governed by electronics and controlled by a Labview code. Fig. 4.4 shows the electronics of the movable stage, on which a bronze sample is placed.

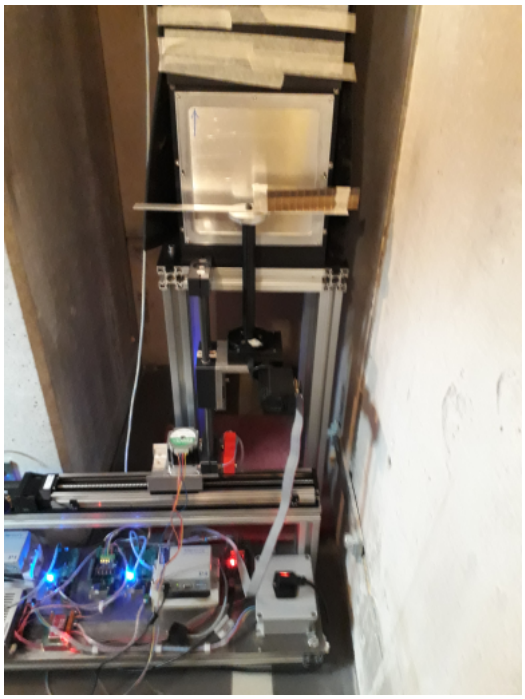

Figure 4.4: photo of the movable stage for the samples, with the controlling electronics.

- **Acquisition box**, shown in fig.4.1 on the right and schematically in fig.3.1. It contains:

  - **Scintillator**. Since for neutron beams, as explained in section 3.1.2, neutrons conversion into charged particles is needed before visible light production in the scintillator, the latter is a zinc sulfide (ZnS) fluorescent compound with a chemical vapor deposition of litium fluoride (LiF). The choice of the scintillator is performed through a comparison between $LiF-ZnS$ "test" scintillators produced by the manufacturer "TRITEC AG", in 2020/2021, with 2:1 composition, area of 1 cm^2, characterized by a different thicknesses (50μm, 100 μm, 200 μm, 250 μm, 300 μm, 400 μm) and different doping material (Silver (Ag), Copper (Cu) and Cadmium (Cd)), and a $LiF-ZnS:Cu$ (2:1) scintillator, produced by the same manufacturer in 2013, with a larger area and a thickness of 300 μm. The doping changes the spectrum of the produced light. Ag doping leads to a light spectrum close to the wavelenghts of blue light, while Cu doping to those of green light. Fig. 4.5 shows the Aluminium

plate onto which the scintillator il placed. In table 4.2 there is the list of the scintillators used for the comparison:

Scintillator	Area (mm × mm)	Thickness (μm)	Proportion LiF:ZnS	Year of production
LiF-ZnS:Ag	10 × 10	50 100 200 250 300 400	2:1	2020/2021
LiF-ZnS:Cu	10 × 10	50 100 200 250 300 400	2:1	2020/2021
LiF-ZnS:Cd	10 × 10	50 100 200 250 300 400	2:1	2020/2021
LiF-ZnS:Cu	200 × 200	300	2:1	2013

Table 4.2: List of the scintillator used for the comparison.

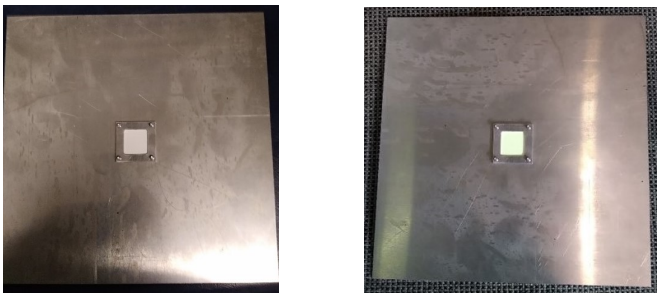

(a) (b)

Figure 4.5: (a)"test" scintillator LiFZnS:Ag and (b)"test" scintillator LiFZnS:Cu placed on the Al plate.

  - A **mirror** with 45° of inclination in order to direct the visible light produced by the scintillator onto the acquisition camera and preserve the latter from radiation damages that could be caused by the interaction with γ -rays.
  - **CCD camera**. The light is directed, through an objective (f3.5 of 20 mm), onto the CCD camera. The model is ZWO ASI 178 MM ([23]). The sensor is 1/1.8" CMOS IMX178 7.4 mm × 5 mm, with a resolution of 6.4 Mega Pixels (3096×2080) and a pixel size of 2.4 μm. The exposure range of the camera is 32μs-1000s. For more technical details, see [23].

- **Computer**. It is used to control the movements of the stage for the samples, and to visualize the acquired digital images. It is also used to perform the preprocessing of the images and their tomographic reconstruction. Finally it allows to perform analyses for the characterization of the setup.

- **Samples**. Here a list of the samples that have been irradiated at NICHE facility.

  - bar pattern P211 in gadolinium (fig. 4.6a);
  - a coffee maker with coffee inside;
  - a bronze elephant statue (82 mm × 63 mm × 30 mm), with a base of dimensions (63.5 mm × 2.5 mm × 44 mm) represented in fig.4.6b;
  - two plastic puppets (≈ 2 cm × 3 cm each);

- a fuchi, that is a metal bordering piece between the swords tsuba (guard) and tsuka (handle) of a Japanese Katana. Its composing material is a copper alloy, and its dimensions are 3.3 cm × 1.6 cm with 1.1 mm of thickness (fig.4.6c).

- two decorative objects, produced in the Iron Age, by a spiral wrapped around a cylindrical core of Frisian origin. One sample is in bronze, while the other is in iron and bronze. The lenght of both samples is ≈ 5 cm (fig.4.6c).

- an aluminium (Al) hollow cylinder with height 15 cm.

- a plastic pendrive with some silicium components.

- an accelerator component in Al realized with additive manufacturing with plastic materials. It is the MACHINA accelerator metal beam exit snout, with height ≈ 4 cm (fig. 4.6d).

- a 1 euro coin, 23.25 mm of diameter and 2.33 mm of thickness. The composing materials are a nickel-brass alloy, containing nickel, zinc and copper, and cupronickel, a copper and nickel alloy.

- eight cylinders of different materials and dimensions, shown in fig 4.6e. The following table reports their characteristics.

cylinder	**diameter (mm)**	**height (mm**	**composition**
Brass	10	100	Cu (63%), Zn (37%)
Silver	10	30	Ag (99.95%)
Aluminium	10	25	Al
Lead	10	25	Pb
Copper	10	25	Cu
Polyethylene	10	25	C (33%), H(66%)
Iron	10	25	Fe
Aluminium big	40	40	Al

Table 4.3: Details of the cylinders used as samples.

(a) (b) (c)

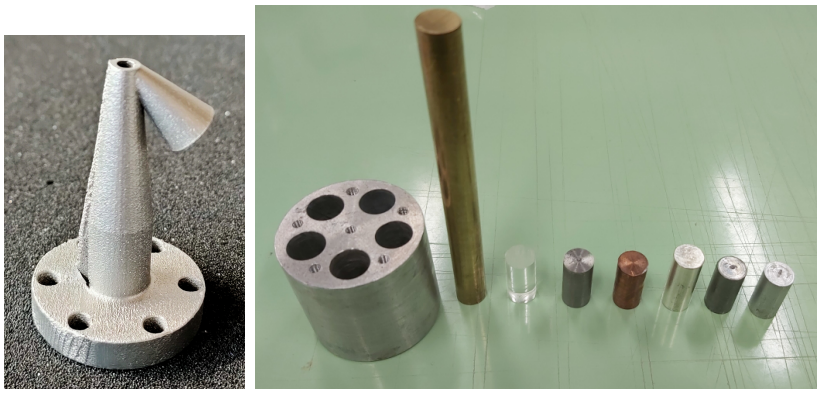

(d) (e)

Figure 4.6: (a) A radiography of the P211 gadolinium bar pattern used for resolution mesurements in the esperiment. (b) The bronze elephant statue. (c) one plastic puppet, the fuchi and the two decorating objects of Iron Age. (d) The accelerator component. (e) The eight cylinders of different materials and dimensions.

4.1.2 Methods

Scintillators comparison

The comparison of the scintillators described in table 4.2 is performed with the acquisition of a radiographic flat image, that means with radiation on and without any sample before the detection box, for each scintillator. The gain is set to 1 and the acquisition time to 300s. In the images, a ROI that includes just the irradiated region is selected and its mean gray value and standard deviation are calculated. The values obtained for each dopant of the scintillators (Ag, Cu ans Cd) are plotted as a function of the scintillator thickness. Necessary considerations are made in order to choose the scintillator for the

experiment.

Spatial resolution

As described in section 3.2.2, the spatial resolution of the detection system of NICHE experiment is calculated with the computation of the Modulation Transfer Function (MTF). At the same time, it is qualitatively estimated by means of the observation of a neutron radiographic image of the bar pattern P211, evaluating the maximum number of line pairs per mm (lp/mm) that can be visibly distinguishable. Figure 4.6a, in previous section, shows the radiography of the bar pattern. The neutron radiographic image is acquired with the following configuration:

- SDD (source to detector distance) = 1465 mm
- P211 Gd bar pattern positioned on the external surface of the Al plate. On the internal surface there is the scintillator.
- scintillator = $LiF - ZnS : Cu$ of 300 μm thickness, produced in 2013
- acquisition time = 600 s
- CCD camera gain = 1 (minimum gain)

For the calculation of the MTF, a region of interest (ROI) which presents a bright and a dark areas, is selected in the image, as shown in fig.4.7. The profile of that region is interpolated, because of the noise, by a specific *tool* of ***PARREC*** ([24]), a program for image elaboration and tomographic reconstruction elaborated by INFN section of Bologna. The result is the Edge Spread Function (ESF). The same *tool* calculates the derivative of the ESF, obtaining the line spread function (LSF) and the module of the Fourier Transform of the latter, that is the MTF.
The values of lp/mm at 10% and 5% of the MTF are taken as values representing the spatial resolution of the detection system.

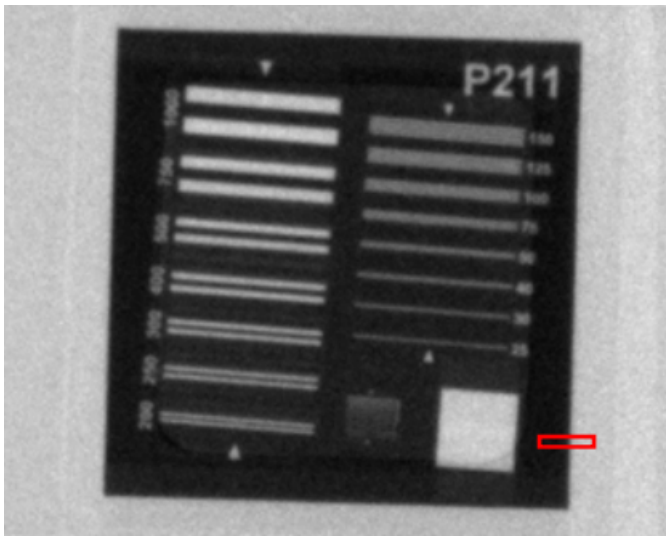

Figure 4.7: With red borders, the ROI selected from the Gd bar pattern radiographic image for the MTF calculation.

A comparison between the obtained spatial resolution values (in lp/mm) and the Nyquist frequency is also performed. The Nyquist frequency is the maximum theorical spatial frequency that can be decoded and correctly reproduced by the acquistion system at a given sampling rate and it is expressed by the formula

$$f_{Ny} = \frac{1}{2\Delta x} \tag{4.1}$$

where f_{Ny} is the Nyquist frequency and Δx is the detector pixel size, the inverse of the detector sampling rate. Δx is calculated dividing the known width of the Gd bar pattern, 30 mm, by the number of pixels, 603, in the radiographic image 4.7 that correspond to the same dimension.

Linearity of the camera and the detection system

The linearity of the CCD camera response is evaluated by the acquisition of a series of images under visible light, positioning the camera out of the detection system, framing a sheet of paper, with increasing integration times, from $100\mu s$ to $8ms$.
In fig. 4.8 an example of acquired image is reported.

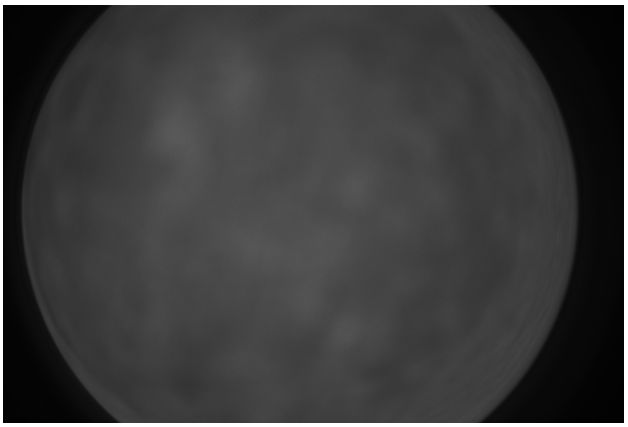

Figure 4.8: Image of a sheet of paper acquired with the CCD camera, with 3000 μs integration time.

A same ROI is selected in each image of the series and the mean gray value, that correspond to the mean light intensity detected, is calculated in that area. The results are plotted as a function of the integration time. A linear fit is computed to evaluate the linearity of the CCD camera and to determine if saturation is present and at which value of integration time it occurs.
Linearity of the whole detection system is evaluated by the same analysis of a series of flat neutron radiographic images, acquired with increasing acquisition times (from 60 s to 600 s).

Signal to Noise ratio

Signal to noise ratio (SNR) of the detection system is computed considering a series of flat images, as described in section 3.2.3, acquired with increasing integration time. Within a same ROI in each image of the series, the mean gray level and the corresponding standard deviation are calculated using the software ImageJ ([25]). The SNR is computed for each image dividing the mean signal by the corresponding standard deviation. The obtained values are plotted as a function of integration time and a fitting is performed. The degree of the fitting function is compared with a square root function ($x^{\frac{1}{2}}$) in order to evaluate the presence of unavoidable statistical noise in the acquired images.

Preliminary radiographic tests

Some neutron radiographies are acquired as tests of the detection system and to visualize interesting features of the samples, hardly visible with alternative imaging methods, like X-ray radiography. First the coffee maker and then the elephant statue (fig.4.6b) are placed on the sample stage and irradiated with the neutron beam for the radiographic images acquisition. Acquisition parameters are:

- SDD (source - detector distance) = 1465 mm;
- SOD (source - object distance) = 1420 mm;
- ODD (object - detector distance)= 45 mm.
- acquisition time = 300 s;
- gain = 1;

The acquired images are normalized and filtered for a noise reduction.

Tomographic reconstruction

Three neutronic tomographies with a final angle of 360° are acquired. The maximum flux of thermal neutrons (E $\approx$ 0.02 eV) is of $1\times\ 10^{13}\ n/cm^2s$. In table 4.4 some acquisition details are reported.

Tomography	**Samples**	**distances (mm)**	**num. of projections**	**acquisition time per projection (s)**
Tomo 1	one plastic puppet the fuchi the two Iron Age decorating materials Al hollow cylinder	SDD = 2000 SOD = 1950 ODD = 50	300	60
Tomo 2	Alluminium big cylinder Silver cylinder Brass cylinder Copper cylinder Lead cylinder Iron cylinder PE cylinder Alluminium cylinder 1 euro coin	SDD = 1465 SOD = 1420 ODD = 45	300	150
Tomo 3	Accelerator component two plastic puppets a usb pendrive the Al hollow cylinder	SDD = 1465 SOD = 1420 ODD = 45	300	120

Table 4.4: Acquisition parameters of the three neutron tomographies. The samples features are reported in Samples, in section 4.1.1.

A dark image (without radiation) and a flat one (with radiation on and without any sample) are acquired before the tomographic projections. Then, as described in section 1.4, the projections are acquired positioning the samples on the rotable stage, placed as close as possible to the scintillator plate. When the neutron irradiation is activated, the stage starts to rotate, with a step angle of 1.2°. At each angle a radiographic image (projection) is acquired.

It is important to know the position of the sample axis of rotation in projection images in order to perform an accurate tomographic reconstruction. Hence, since the axis of rotation of the sample does not necessarly correspond to the central axis of the detection system, I implemented a python program, called ***axis of rotation***, published on GitHub [26], in order to correct this misalignment. By means of ***axis of rotation*** program, the shift and the tilt angle of the sample axis of rotation with respect to the central vertical axis of the detection system (the central vertical axis of the images) are computed and the projections images are corrected. The shift and the tilt angle are calculated considering the projections acquired at 0° and at 180°. The centre of rotation for each vertical coordinate of the 0° image is calculated with a least square method applied to

the projection at 0° and the flipped projection at 180°, that should be ideally equal to the 0° image. Then a polynomial fit is performed on the obtained shift values in order to find the tilt angle and the middle shift of the axis of rotation of the sample with respect to the central vertical axis of the images. ***Axis of rotation*** program also allows to perform a preprocessing of the images, by cropping, normalizing and/or filtering the images from outliers before the correction.
Cropping process allows to remove the non relevant outer areas of the images, selecting just the region where a relevant signal is collected and the sample is visible.
The normalization is the process that changes the range of pixel intensity values. Also called contrast stretching, it enhances the contrast of the image. Each px intensity of each projection is calculated with the formula

$$I_{new}(x,y) = -ln\left(\frac{I(x,y) - I_{min}(x,y)}{I_{max}(x,y) - I_{min}(x,y)}\right) \tag{4.2}$$

where $I_{new}(x,y)$ is the new px intensity at position (x,y), $I(x,y)$ is the old px value, $I_{min}(x,y)$ is the corresponding px intensity of the dark image, $I_{max}(x,y)$ is the px intensity of the flat image and ln is the natural logarithm.
The outlier filtering is a non-linear process that reduces random or salt-and-pepper noise and preserves edges in an image. It's useful for correcting, e.g., hot pixels or dead pixels of a CCD image. ***Axis of rotation*** program corrects the px values in an image computing the weighted combination of two values, the original one and the one obtained with the application of a median filter. Hence the corrected px intensity is given by the following formula:

$$I_{corrected}(x,y) = w(x,y)I_{original}(x,y) + (1 - w(x,y))I_{median}(x,y) \tag{4.3}$$

where $I_{corrected}(x,y)$ is the corrected px intensity at position (x,y) in a image, $I_{original}(x,y)$ is the px value of the original image at the same position, $I_{median}(x,y)$ is the median px intensity of the px values in a neighboorhood of the (x,y) position and $w(x,y)$ is 0 or 1 whether the original px intensity deviates from the median value by a certain threshold or not.
The user can choose wich preprocess/es to perform before the computation of the position of the sample axis of rotation and the eventual correction of the images.

In the current case all the preprocesses, cropping, normalization and outliers filtering, are performed.
The corrected projections are elaborated by the ***PARREC*** software for the tomographic reconstruction.
The FeldKamp algorithm is used for the reconstruction. This algorithm, as shown in the fig. 4.9, takes into account a more realistic configuration of the neutron beam with respect to a parallel beam geometry. Hence, the radiation is considered divergent as a cone beam, and the final result of the FeldKamp is a stack of slices of the sample, that allows its three dimensional visualization.

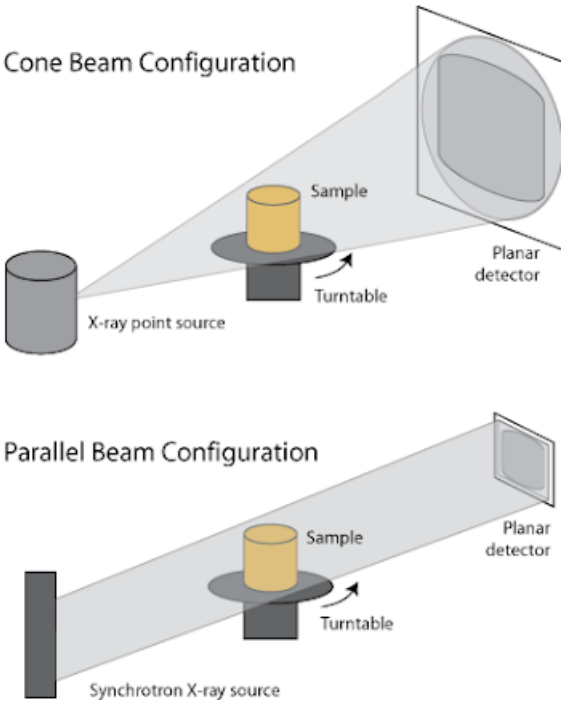

Figure 4.9: On the top of the figure a cone beam configuration, on the bottom a parallel beam configuration.

For all the tomographies the three dimensional rendering of the sample is elaborated with ***VgStudio Max*** software ([27]).
For Tomo 2, in addition, in which the samples composition are known, a calibration curve is evaluated for the conversion of gray levels obtained in the reconstructed images into the total neutron macroscopic cross section Σ_t of the corresponding materials, defined in eq. 1.6.

The curve is obtained by the fitting of the theoretical Σ_t, plotted as a function of the corresponding mean gray values in the reconstructed images. The theoretical neutron macroscopic cross section for each sample is calculated starting from the microscopic absorption and scattering cross section values (σ_a and σ_s) tabulated in the National Institute if Standards and Technology (NIST) site [28]. These values are summed, as expressed in eq. 1.5, in order to find the total microscopic cross section σ_t for each element. Then σ_t is multiplied by the element atomic density, defined in eq. 1.8, finding the total macroscopic cross section for that element. Finally the sample macroscopic cross section is calculated by a weighted combination of the Σ_t of its composing elements, as in equation 1.7.
The mean gray values are calculated in a region of interest in the reconstructed images for each sample.
For Tomo 3, because of the presence of a publication by F. Grazzi et al. [29], about the accelerator component, where the results of the combination of X-ray and neutron tomographies for the characterization of its manufacturing components are reported, a visual comparison between the obtained neutron images in the present work and the ones published in the article is performed.

Chapter 5

Results

5.1 Scintillators comparison

The available scintillators, described in table 4.2, were evaluated according to the image brightness, i.e. the average gray lavel in a selected ROI. The mean signal of the images acquired by means of the usage of a different scintillator are reported in fig.5.1.

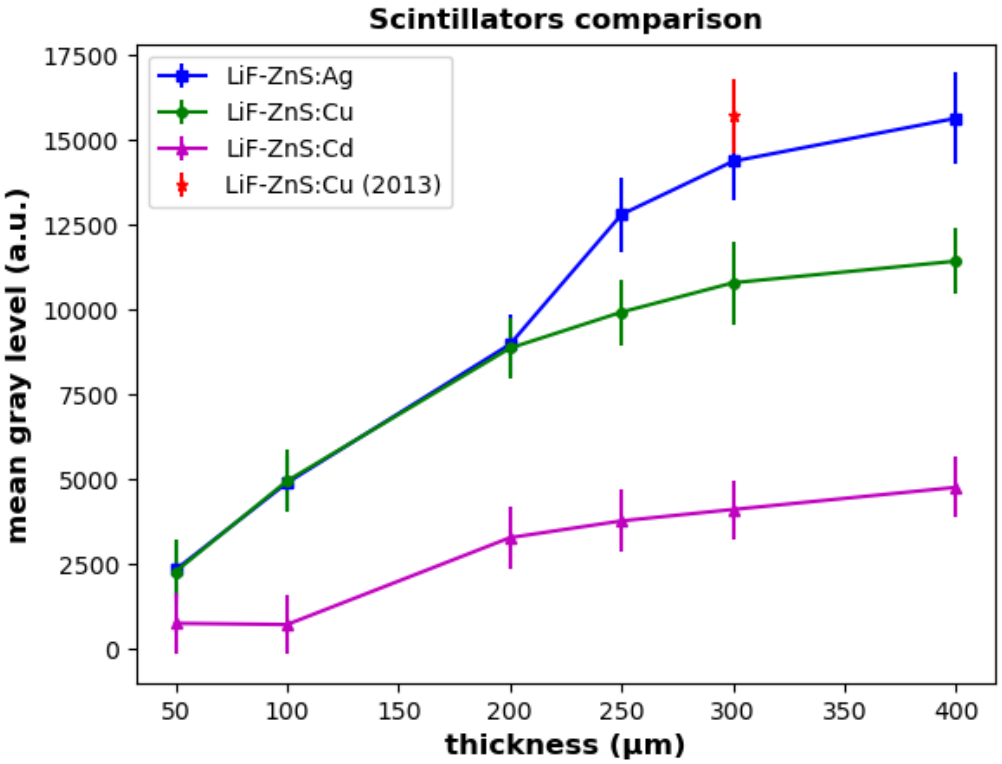

Figure 5.1: Mean signal acquired in a flat radiographic image for three different scintillator doping materials and different scintillator thicknesses. The different lines represents different dopant elements (Ag in blue, Cd in magenta, Cu in green and red).

5.2 Spatial resolution

The results obtained about the spatial resolution of the detection system are here reported.

A first qualitative estimate, performed with the observation of the Gd bar pattern radiography, shown in fig. 4.6a and fig. 4.7, is expressed by the maximum number of distinguishable line pairs per millimeter (lp/mm). The result is the following:

$$spatial\ \ resolution_{obs} = (2.9 \pm 0.2)\ \ lp/mm \tag{5.1}$$

The alternative method, more rigorous, that exploited the calculation of the MTF, has given the following results:

$$spatial\ \ resolution_{10\%} = 1.87\ \ lp/mm \tag{5.2}$$

$$spatial\ \ resolution_{5\%} = 2.23\ \ lp/mm \tag{5.3}$$

$$f_{cut} = 3.00\ \ lp/mm \tag{5.4}$$

The values in eq.5.2 and in eq.5.3 are the spatial frequencies at 10% and 5% of the Modulation Transfer Function (MTF) and eq.5.4 is the cutting frequency, where the MTF approaches zero value, obtained by the computations expressed in the following figures (5.2), that describes the passages of the PARREC tool.
The measured pixel size, $(0,0500 \pm 0.001)mm$, has provided a Nyquist frequency of the detection system:

$$f_{Ny} = (10.00 \pm 0.02)\ \ lp/mm \tag{5.5}$$

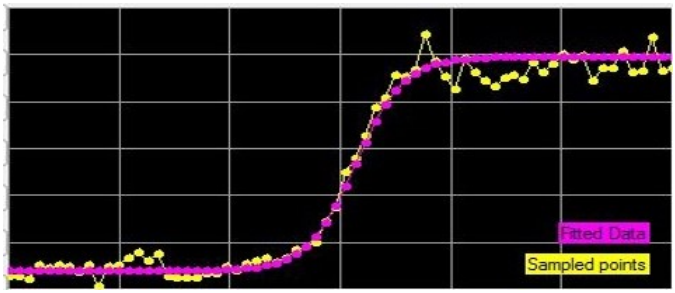

(a) Interpolated ESF in pink and sampled points in yellow

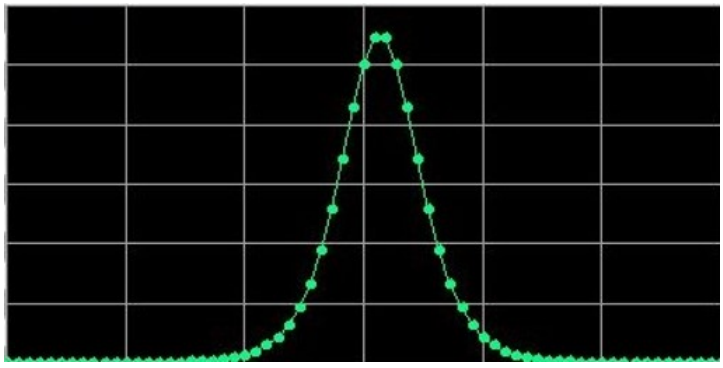

(b) LSF calculated with the ESF in (a)

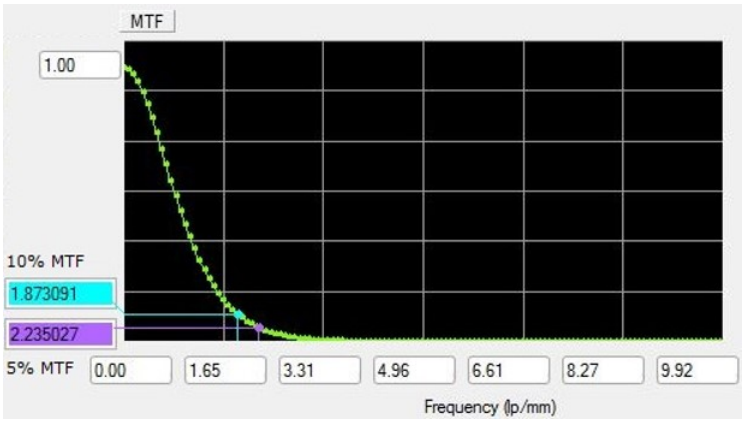

(c) MTF calculated with the LSF in (b)

Figure 5.2: Data elaboration and plots shown in PARREC software. (a) the Edge Spread Function (ESF) interpolated from the experimental noisy data. (b) The Line Spread function (LSF) calculated as the derivative of the ESF. (c) The normalized MTF, that is the module of FFT of the LSF. The values of spatial frequencies at 10% and 5% MTF are highlighted.

5.3 Linearity

The analysis of the linearity of the CCD camera response with respect to the acquisition time has given the results shown in the following plot, where the fitting line equation is reported in the legend.

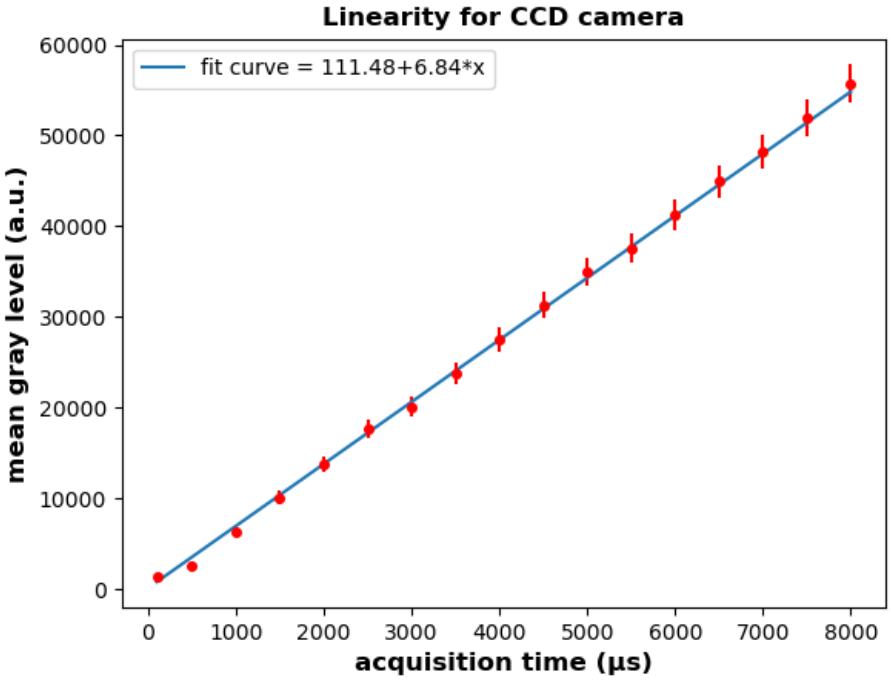

Figure 5.3: Plot of the mean signals (mean gray levels) of a same ROI in all the images of the series, like the one shown in fig.4.8, acquired with different acquisition times (from $100\mu s$ *to* $8ms$*). Red points are the mean signals, in blue the fitting line of the data.*

The analysis of the linearity of the whole detection system response with respect to the acquisition time, considering four flat images acquired with the neutron imaging setup, gave rise to the results shown in fig.5.4, where the mean signal is plotted as a function of the acquisition time. A linear fit was also performed and the fitting line equation is shown in the plot legend.

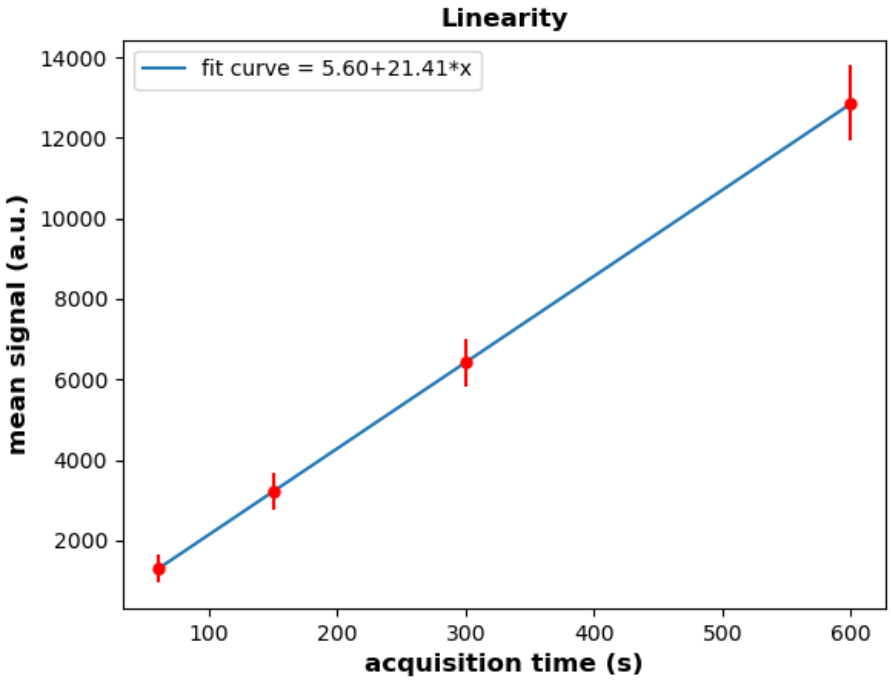

Figure 5.4: Plot of the mean signal of a same ROI in all the flat images of the series acquired with increasing acquisition times (60 s, 150 s, 300 s, 600 s). Red points are the mean signals, in blue the linear fitting line of the data.

5.4 Signal to noise ratio

The SNR analysis for the camera and for the whole detection system gave rise to the results reported in the following figures. Fig. 5.5 shows the SNR calculated for the image series acquired with just the CCD camera, while fig.5.6 shows the signal to noise ratio vs. acquisition time calculated for the four flat images acquired with the whole detection system. In both figures a fit with a function $y = ax^b$ has been performed.
For the CCD camera, the fit curve equation is the following:

$$y = 0.71\, x^{0.40} \tag{5.6}$$

where the curve coefficients are $a = 0.71 \pm 0.07$ and $b = 0.40 \pm 0.01$.
For the whole detection system, the curve equation is

$$y = 0.54\, x^{0.51} \tag{5.7}$$

where the curve coefficients are $a = 0.54 \pm 0.05$ and $b = 0.51 \pm 0.02$. In both equations y is the SNR and x is the acquisition time.

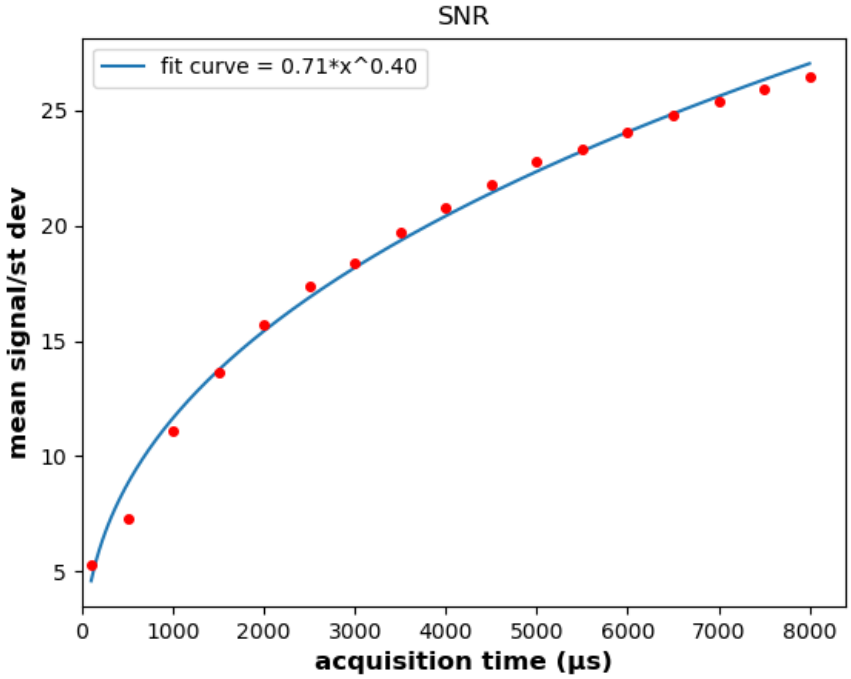

Figure 5.5: Plot of the SNR as a function of the acquisition time for the images acquired with just the CCD camera. The blue line represents the fit of the data.

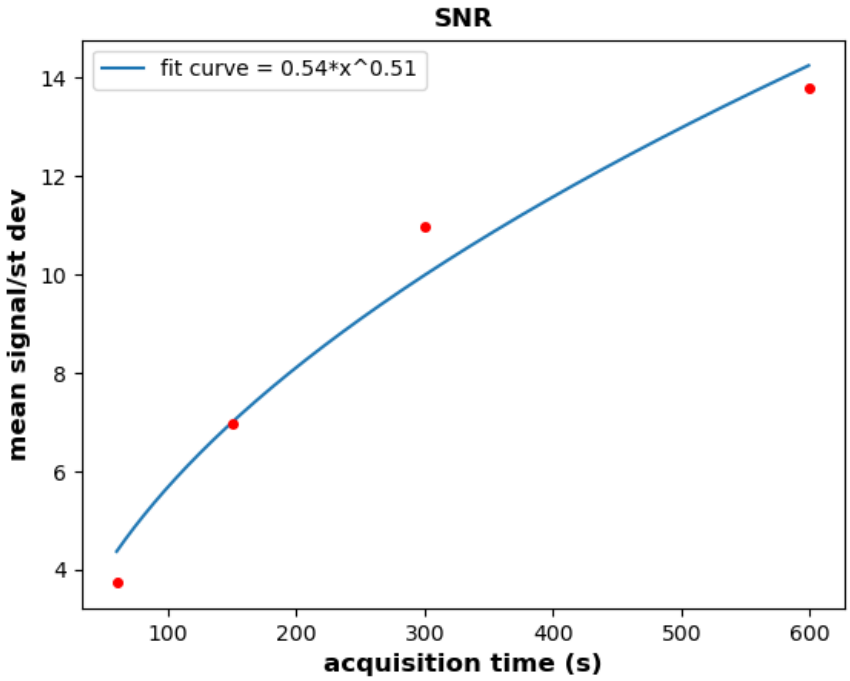

Figure 5.6: SNR as a function of the acquisition time for the flat images acquired with the whole neutron imaging detection system. The mean signals and the corresponding standard deviations are reported in fig.5.4. In blue the fit line of the SNR data.

5.5 Preliminary radiographic test

Two neutron radiographic images are shown in fig.5.7, for the bronze elephant statue and in fig.5.8, for the coffee maker.

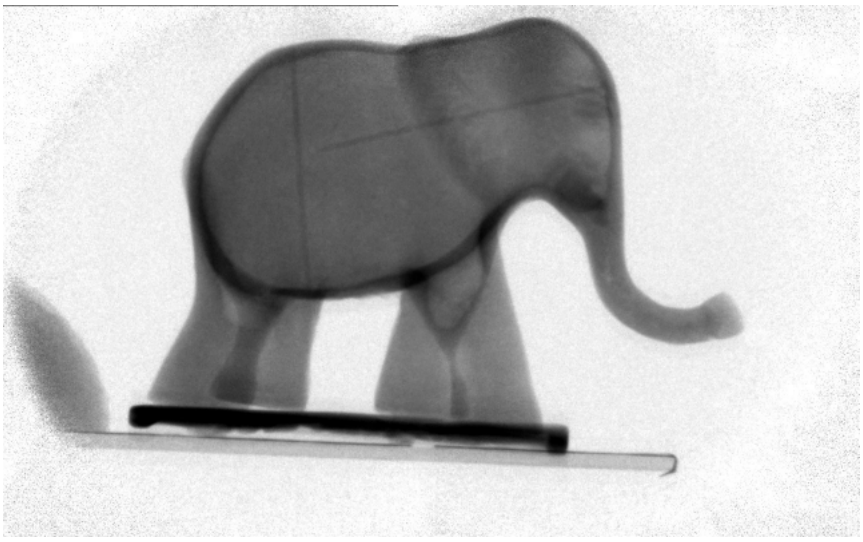

Figure 5.7: Neutron radiography of the bronze elephant statue, represented in fig.4.6b.

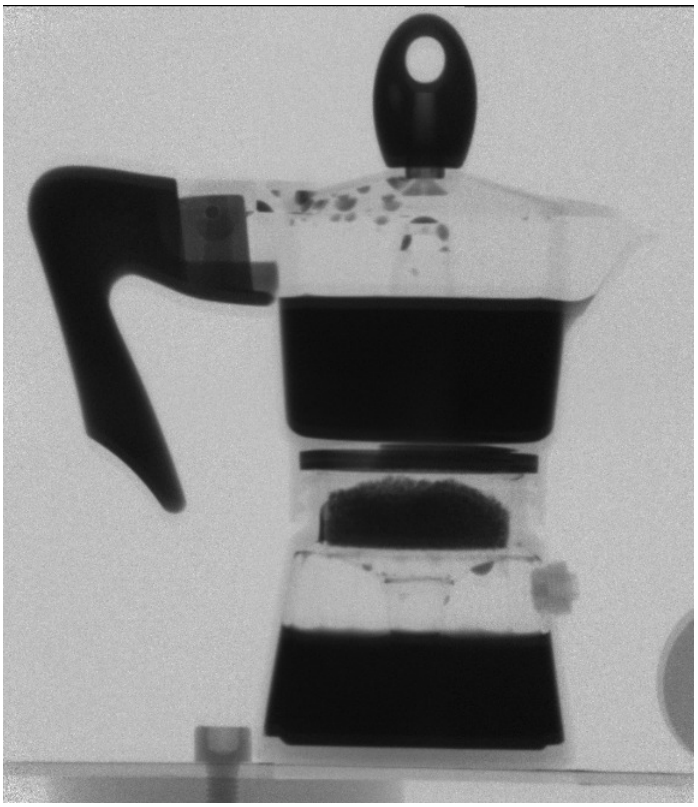

Figure 5.8: Neutron radiography of the coffee maker with coffee inside.

5.6 Neutron tomography

5.6.1 Tomo 1

The first neutron tomography was performed with the samples listed in the first row of the table 4.4 and illustrated in fig. 4.6c, all placed into an aluminium hollow cylinder, to facilitate the positioning of the samples on the rotating stage. Two of the acquired projections are shown in fig.5.9.

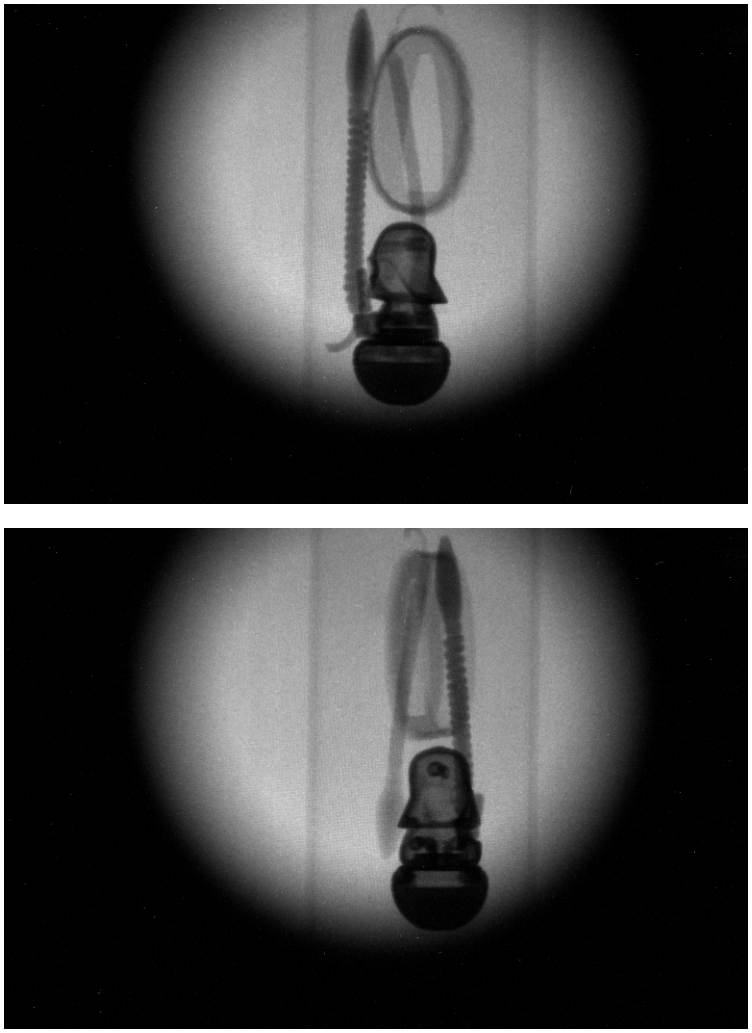

Figure 5.9: Two radiographic projections acquired in the neutron tomography Tomo 1 at different angles.

The projections were corrected with the program ***axis of rotation*** in order to ob-

tain projection images, in which the central vertical axis corresponds to the rotation axis of the sample. With ***axis of rotation*** program, the images were cropped, normalized and filtered from bright outliers, before the correction of the rotation axis. The results of the elaborations performed by means of the program ***axis of rotation*** are shown in fig. 5.10 and fig.5.11.
In the uncorrected images, the computed tilt angle (θ) of the sample axis of rotation with respect to the central vertical axis of the images is $\theta = 0.564^{\circ}$ and the shift at the middle vertical coordinate is $offset = -7.00 px$.
The tomographic reconstruction of the corrected projections, performed with ***PARREC*** software, produced frontal slices of the sample, that have been elaborated with the software ***VgStudio Max***, obtaining the three dimensional rendering shown in fig.5.12. It also allowed the visualization of the internal volume of the sample, as shown in fig. 5.13.

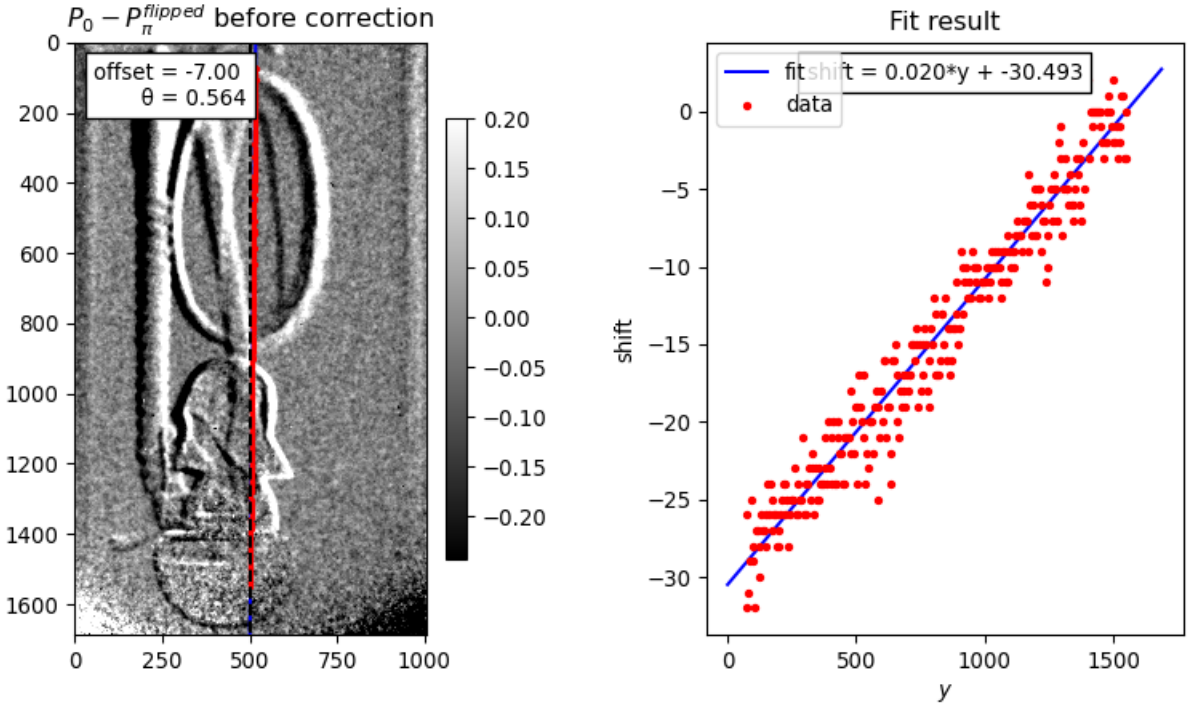

*Figure 5.10: Results of the elaborations performed with **axis of rotation** program, before the correction of the images. On the left, the difference between the projection acquired at angle 0° and the flipped projection at 180°. In this image, the dashed black line represents the central vertical axis, while the red line represents the computed axis of rotation of the sample. On the right, the red points are the shift values of the sample axis of rotation with respect to the central axis of the images for each selected vertical coordinate (y). The blue line is the fitting line of the data, used for the computation of the sample axis of rotation position and tilt angle.*

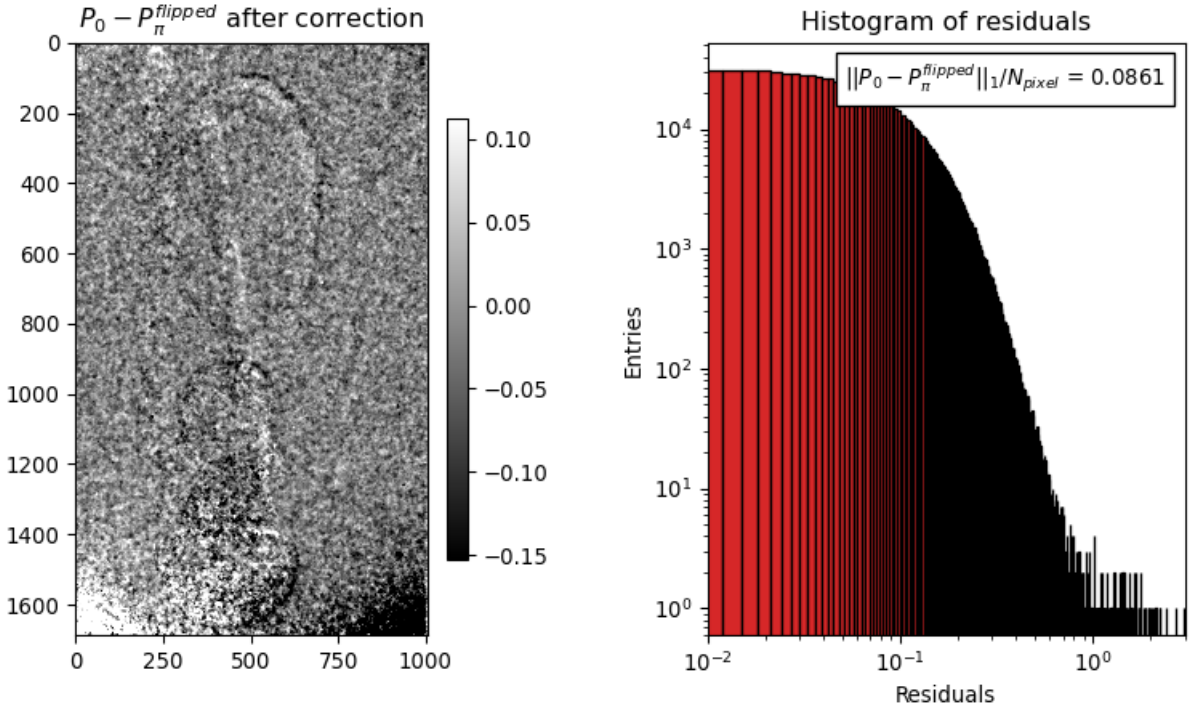

Figure 5.11: Results of the elaborations performed with ***axis of rotation*** *program, after the correction of the images. On the left the difference between the corrected projection at 0° and the flipped corrected projection at 180°. On the right the histogram of the residuals of the two images.*

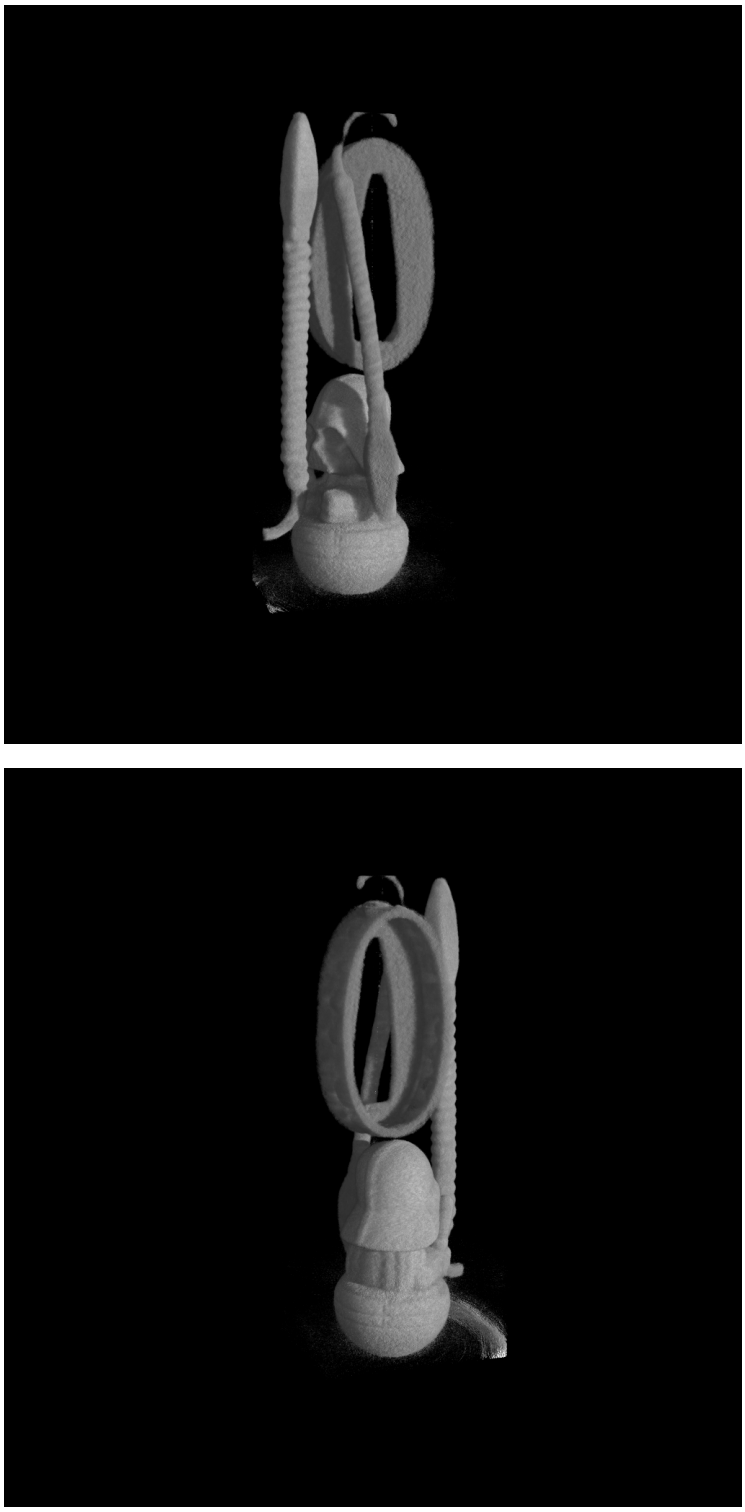

Figure 5.12: Two views of the three dimensional rendering of the tomographic reconstruction for Tomo 1.

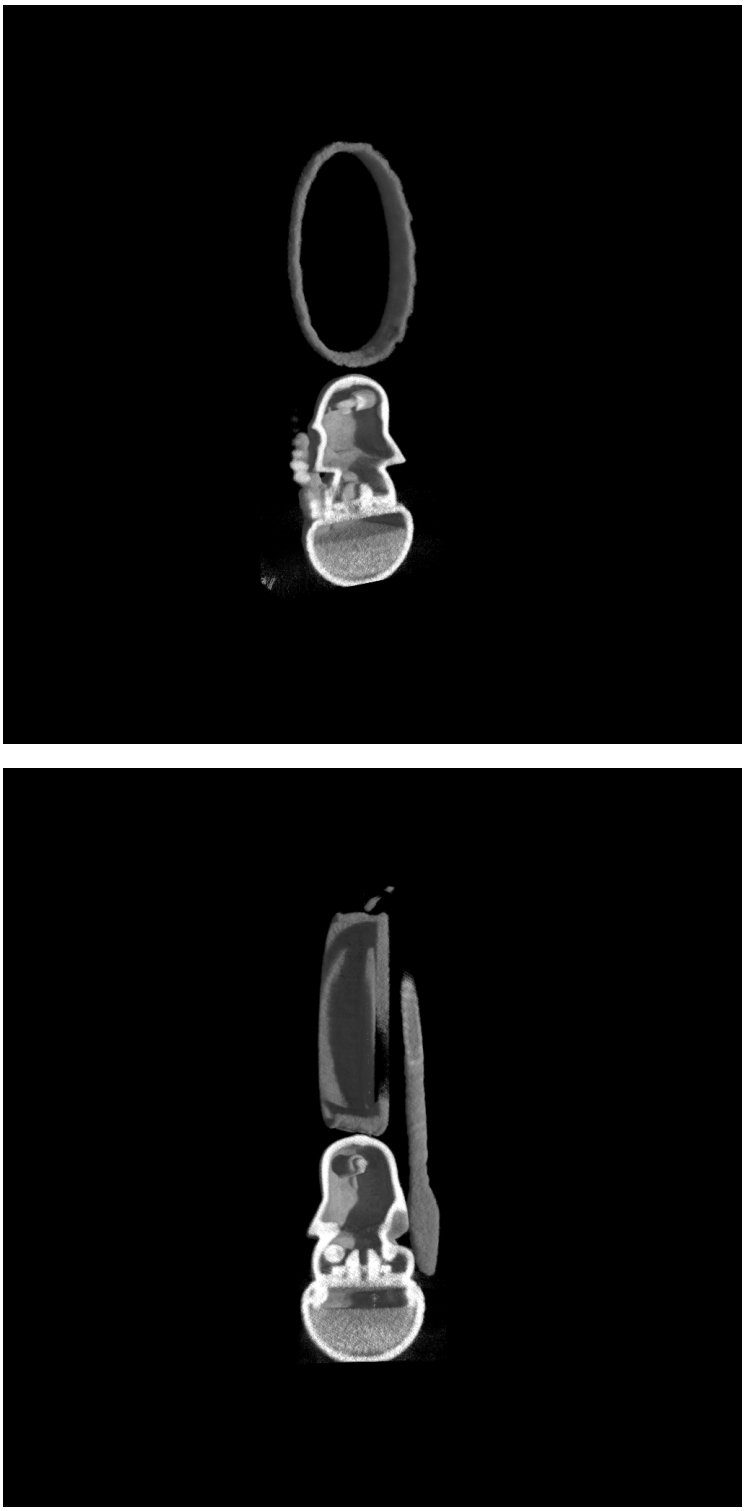

Figure 5.13: Two virtual sections of the samples in Tomo 1. It is possible to visualize internal details of the samples.

5.6.2 Tomo 2

The second tomography was performed with the samples listed in the table 4.4 and partially shown in fig. 4.6e. Their arrangement is represented in fig. 5.14. Two examples of acquired projections are shown in fig.5.15.
As for the case of Tomo 1, the projection images were preprocessed and corrected for a sample axis of rotation tilt angle $\theta = 0.163°$ and a $offset = -13.50px$ at the middle vertical coordinate with respect to the central vertical axis of the images, by means of ***axis of rotation*** program (fig.5.16 and 5.17).
The corrected images were elaborated with ***PARREC*** and ***VgStudio Max*** softwares, obtaining the rendering shown in fig.5.18.

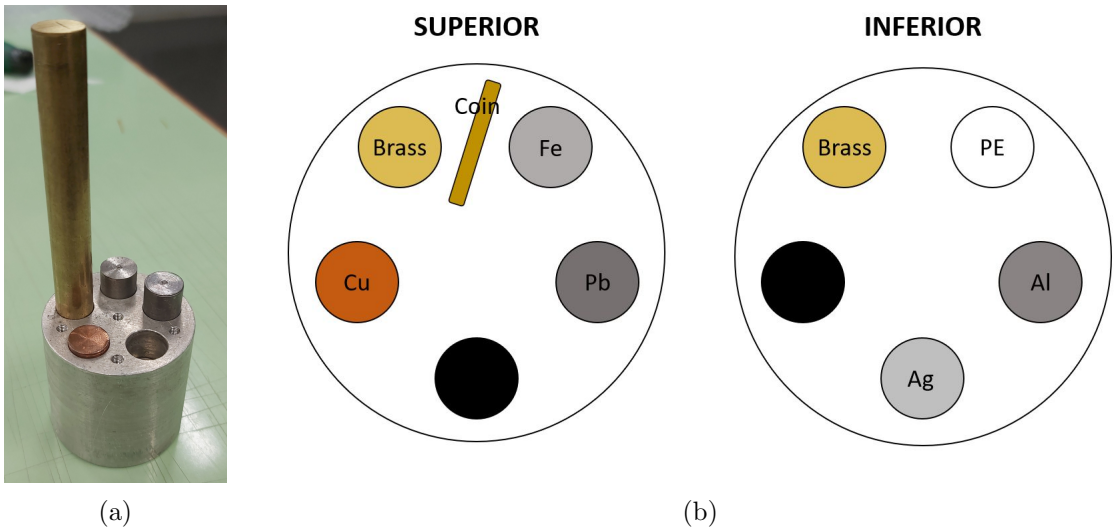

(a) (b)

Figure 5.14: Arrangment of the samples of Tomo 2. (a) A photo of the arrangement (the coin is missing). (b) The scheme (view from above) of the arrangement for the superior section and the inferior section of the sample. The black circles stand for voids.

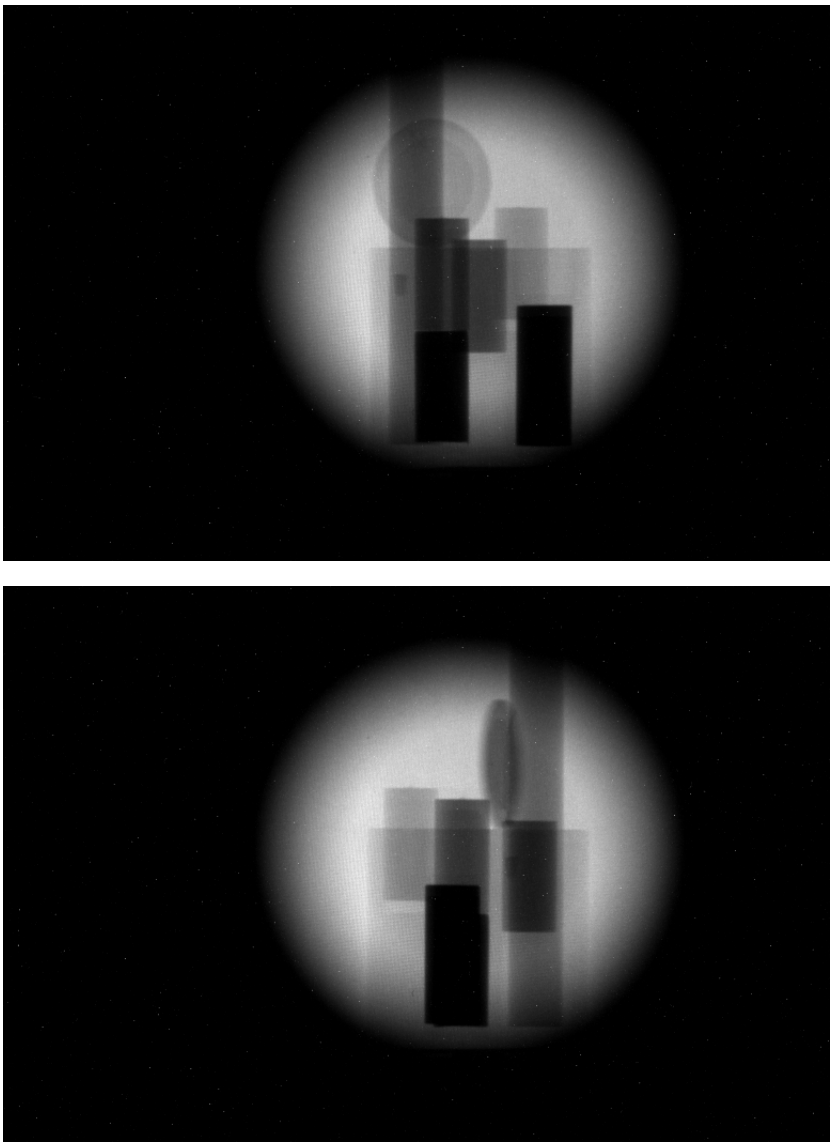

Figure 5.15: Two of the 300 acquired radiographic projections in the neutron tomography Tomo 2 at different angles.

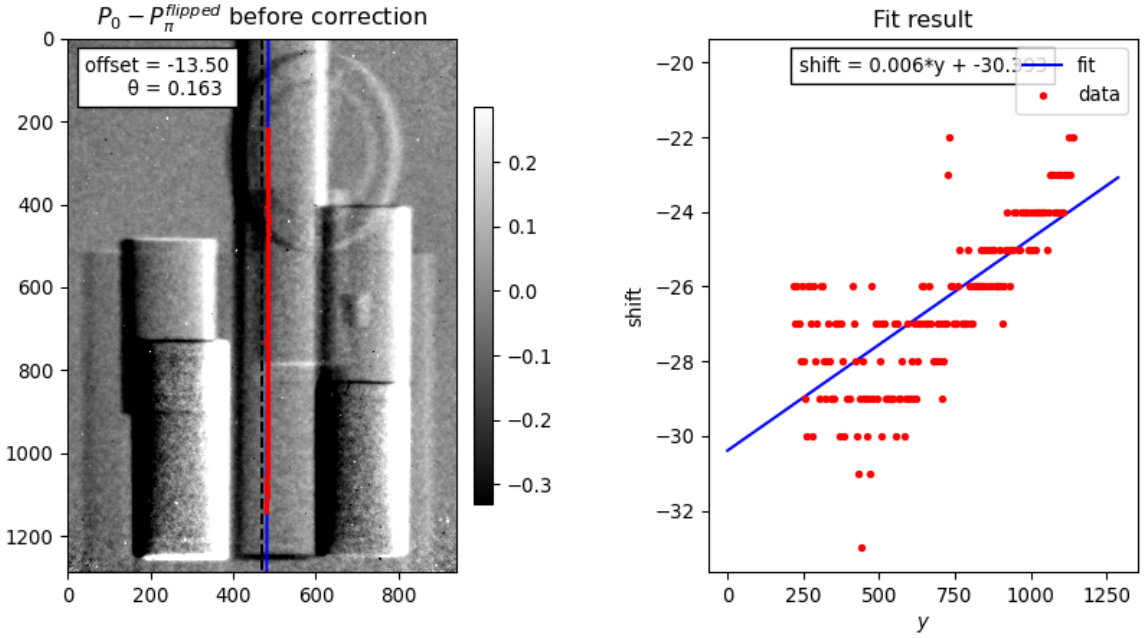

*Figure 5.16: Results of the elaborations performed with **axis of rotation** program, before the correction of the images. On the left, the difference between the projection acquired at angle 0˚ and the flipped projection at 180˚. In this image, the dashed black line represents the central vertical axis, while the red line represents the computed axis of rotation of the sample. On the right, the red points are the shift values of the sample axis of rotation with respect to the central axis of the images for each selected vertical coordinate (y). The blue line is the fitting line of the data, used for the computation of the sample axis of rotation position and tilt angle.*

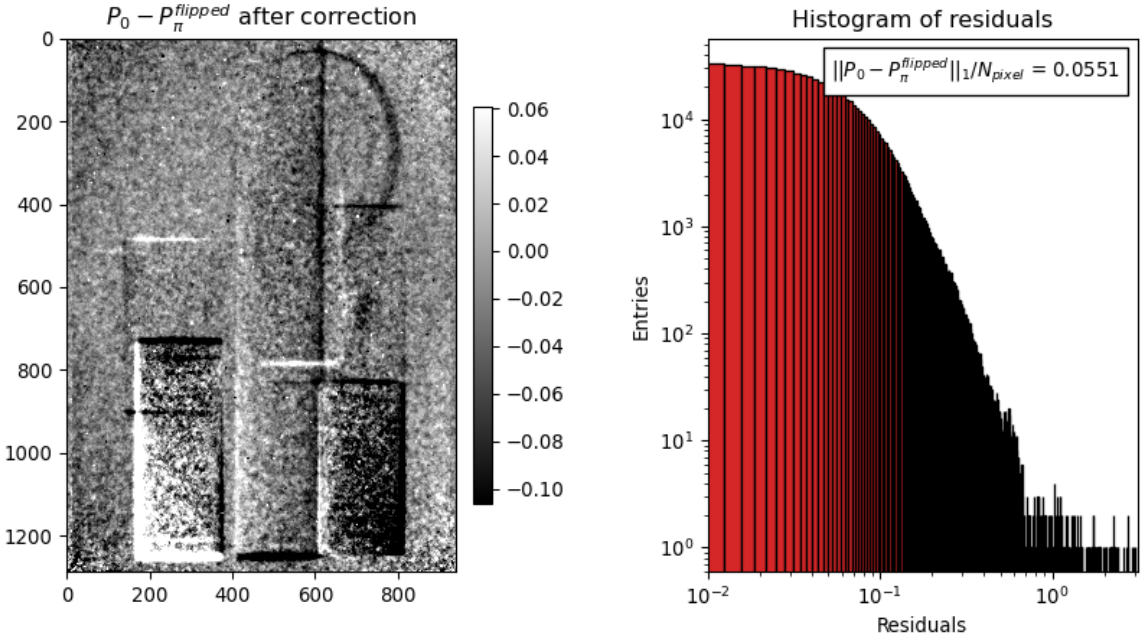

Figure 5.17: Results of the elaborations performed with ***axis of rotation*** *program, after the correction of the images. On the left the difference between the corrected projection at 0˚ and the flipped corrected projection at 180˚. On the right the histogram of the residuals of the two images.*

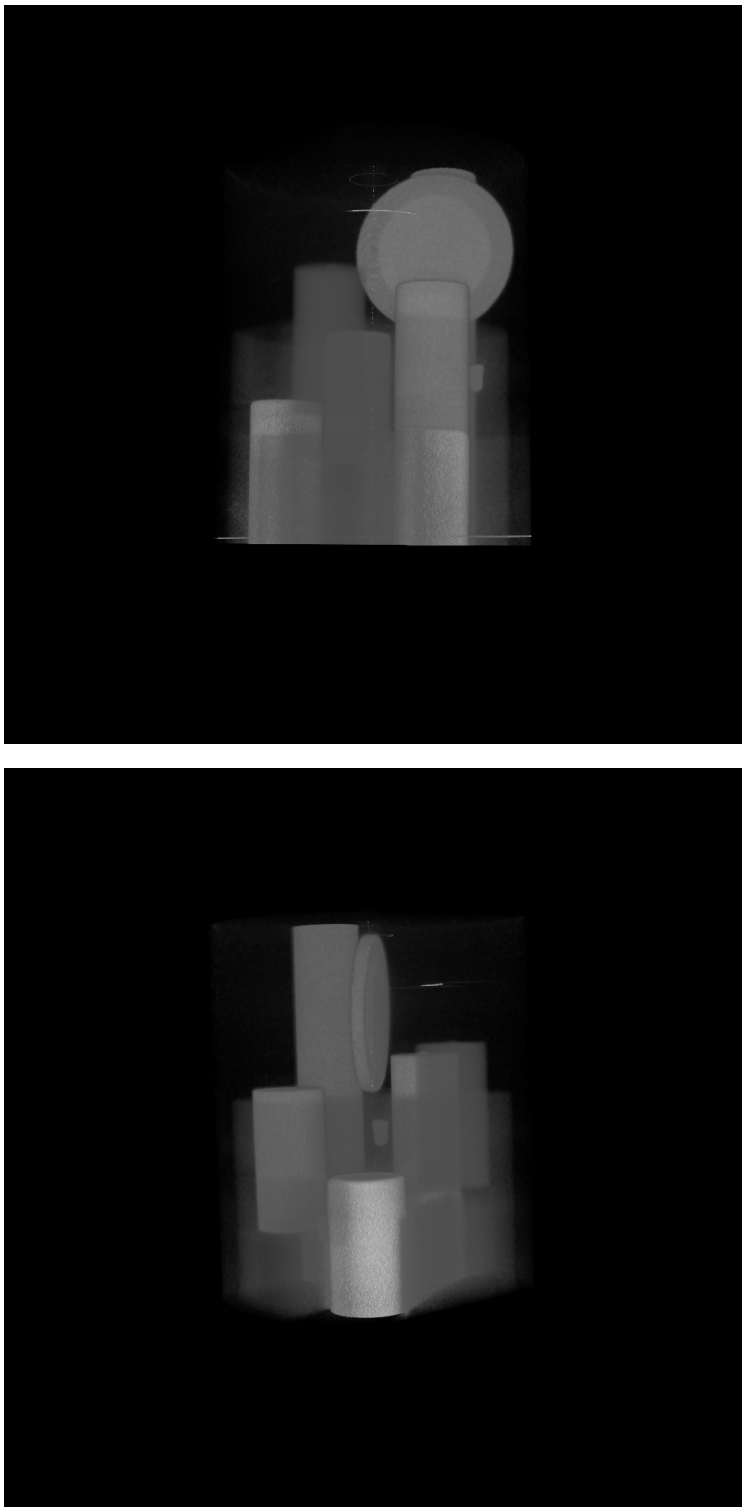

Figure 5.18: Two views of the three dimensional rendering of the tomographic reconstruction for Tomo 2.

Two axial slices of the samples, one for the superior section and one for the inferior one are shown in fig.5.19, in which each cylinder is identified by the symbol of the composing material.

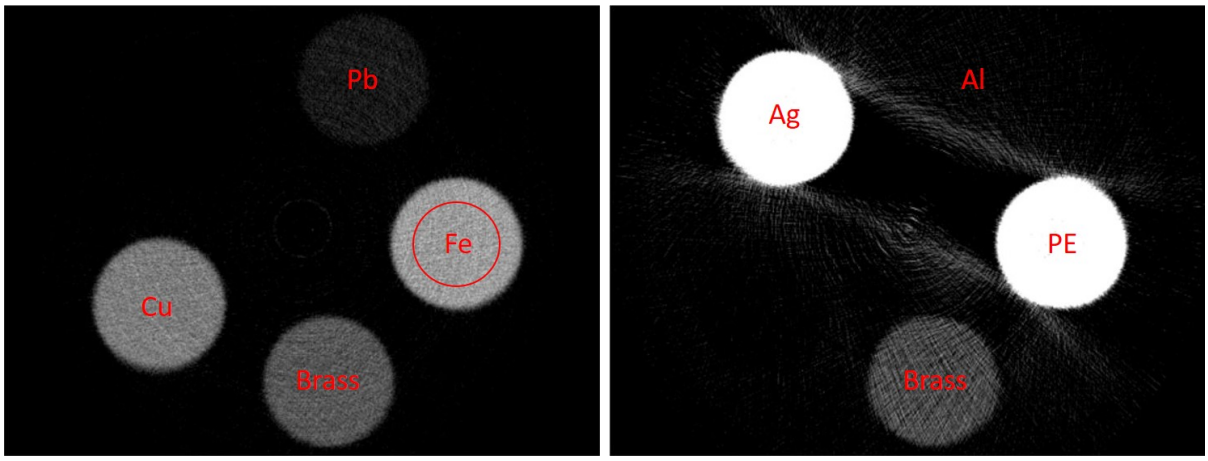

(a) (b)

Figure 5.19: (a) Axial slice representing the superior section of the sample. In red the composing material of the cylinders and a ROI in the Iron (Fe) cylinder. (b) Axial slice for the inferior section of the sample.

For the computation of the calibration curve, needed for the conversion of the mean gray values of the cylinders in the reconstructed images to the corresponding neutron macroscopic cross sections (Σ_t), six adjacent axial slices for the superior section and six for the inferior one have been selected. In each of them and for each cylinder, a ROI, with same shape and area of the one shown in red on the Iron (Fe) cylinder in fig.5.19a, was used for the calculation of the corresponding mean gray value, computing first the mean in one slice, then the average on the six slices.
The obtained gray levels were compared with the theorethical macroscopic cross sections (Σ_t), calculated with the method described in section 4.1.2.
Table 5.1 reports density, neutron microscopic and macroscopic cross sections of the cylinders composing materials. Figure 5.20 shows the theoretical Σ_t plotted as a function of the mean gray level for each cylinder and the resulting fitting curve is the calibration curve. The curve equation is the following:

$$y = a + bx = -0.06 + 0.02\,x \tag{5.8}$$

with y the total macroscopic cross section (Σ_t) and x the average gray level. More precisely, the curve coefficients are $a = (-0.06 \pm 0.20)\ cm^{-1}$ and $b = (0.020 \pm 0.002)\ (cm \cdot gray\ level)^{-1}$.

Material	**Composition**	**Density** (g/cm^3)	$\sigma_t = \sigma_{abs} + \sigma_{scatt}$ (b)	**Atomic weight (amu)**	Σ_t ($1/cm$)
Brass	Cu (63%)	8.96	1.18×10^{-23}	63.55	0.76
	Zn (37%)	7.13	5.24×10^{-24}	65.38	
Silver	Ag	10.5	6.83×10^{-23}	107.86	4.00
Aluminium	Al	2.7	1.73×10^{-24}	26.98	0.10
Lead	Pb	11.35	1.13×10^{-23}	207.2	0.37
Copper	Cu	8.96	1.18×10^{-23}	63.55	1.00
Polyethilene (PE)	C (33%)	2.26	5.55×10^{-24}	12.01	3.15
	H (66%)	0.09	8.24×10^{-23}	1.00	
Iron	Fe	7.87	1.42×10^{-23}	55.85	1.20

Table 5.1: density, total microscopic cross section (σ_t) from NIST site [28], atomic weight and total macroscopic cross section (Σ_t) for each cylinder. Σ_t is calculated with the formula reported in equation 1.7.

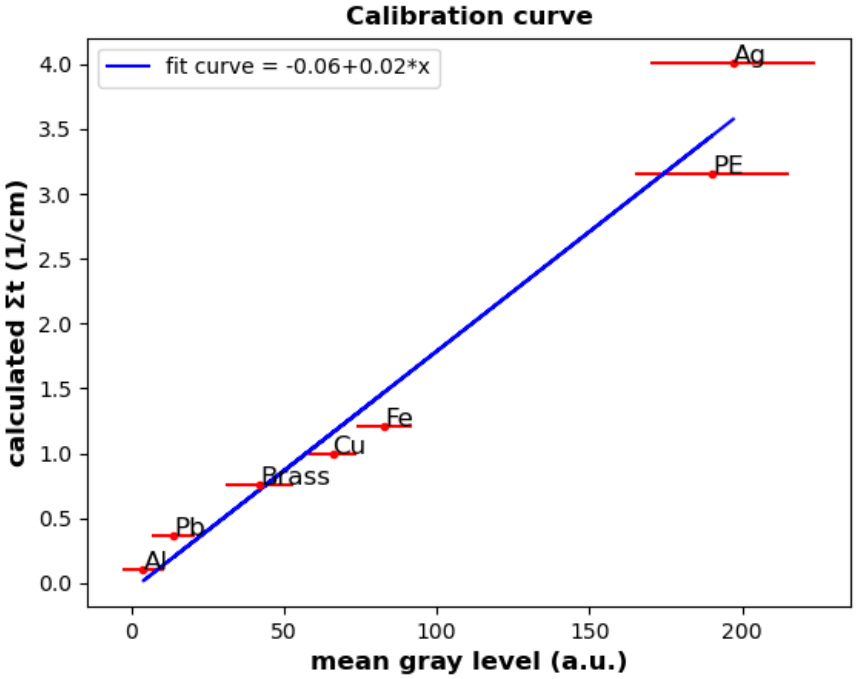

Figure 5.20: The plot has on the abscissa the mean gray levels with the corresponding standard deviations (in red) for each cylinder, on the ordinate the corresponding calculated total neutron macroscopic cross section, from the tabulated microscopic cross section data reported in NIST site [28]. The blue line is the fitting line, that turns to be a calibration curve for the conversion of the mean gray levels to total macroscopic cross sections.

5.6.3 Tomo 3

The third tomography was performed with the samples listed in table 4.4, all placed into an Aluminium hollow cylinder in order to facilitate the positioning of the samples on the rotable stage. The main sample, the additive manufacturing MACHINA accelerator component, is illustrated in fig. 4.6d. Two examples of acquired projections are shown in fig.5.21.

By means of ***axis of rotation*** program, the projections were preprocessed (cropping, normalization and outliers filtering) and corrected for the misalignment between the sample axis of rotation and the central vertical axis of the images by an angle $\theta = 0.477°$ and a $offset = -15.00px$ at the central vertical coordinate. The results are shown in fig.5.22 and fig.5.23.

The corrected tomographic projections were reconstructed with FeldKamp algorithm, through the usage of ***PARREC*** software and then visualized with ***VgStudio Max*** program. The resulting 3D rendering of the samples is shown in fig.5.24 and two virtual sections of the samples are shown in fig.5.25.

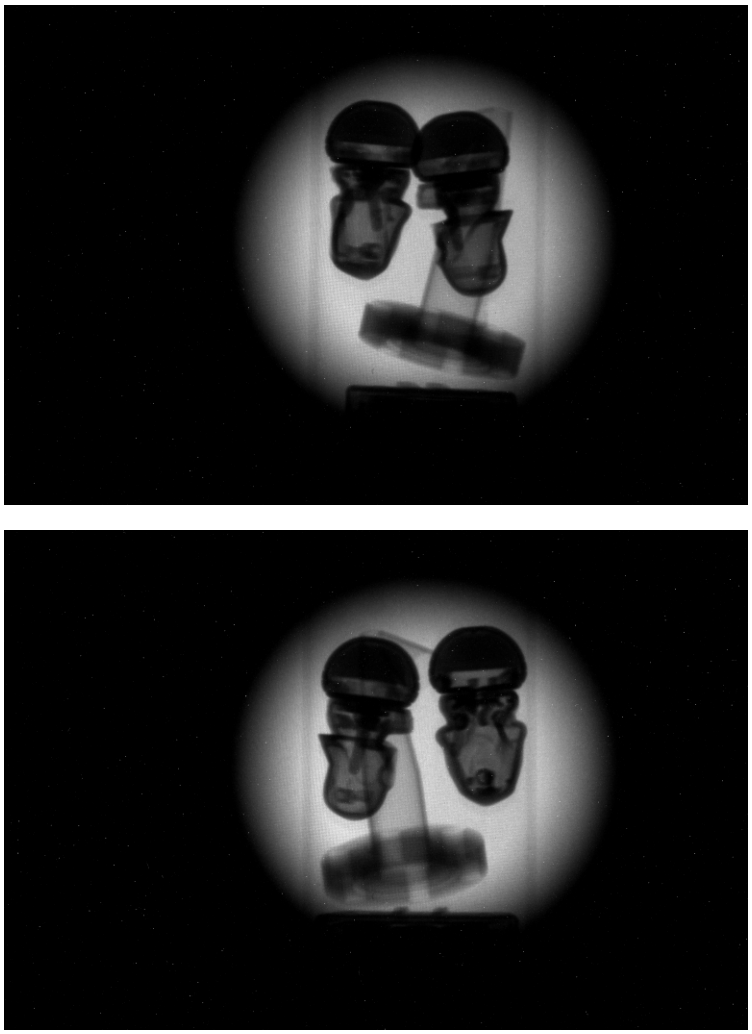

Figure 5.21: Two of the 300 acquired radiographic projections in the neutron tomography Tomo 3 at different angles.

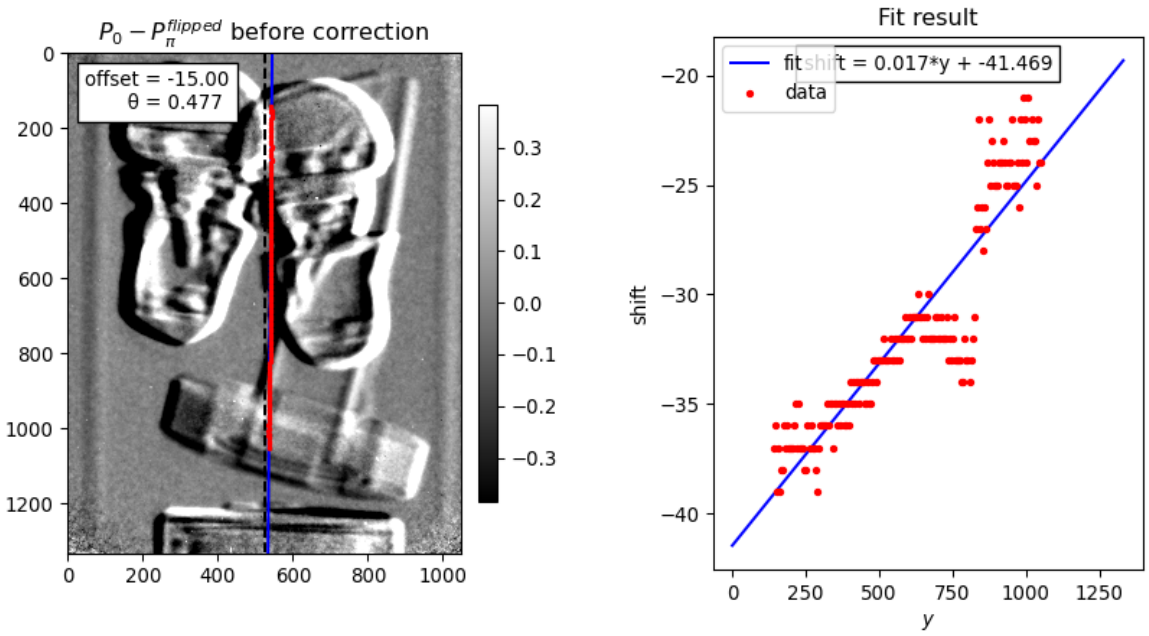

Figure 5.22: Results of the elaborations performed with ***axis of rotation*** *program, before the correction of the images. On the left, the difference between the projection acquired at angle 0° and the flipped projection at 180°. In this image, the dashed black line represents the central vertical axis, while the red line represents the computed axis of rotation of the sample. On the right, the red points are the shift values of the sample axis of rotation with respect to the central axis of the images for each selected vertical coordinate (y). The blue line is the fitting line of the data, used for the computation of the sample axis of rotation position and tilt angle.*

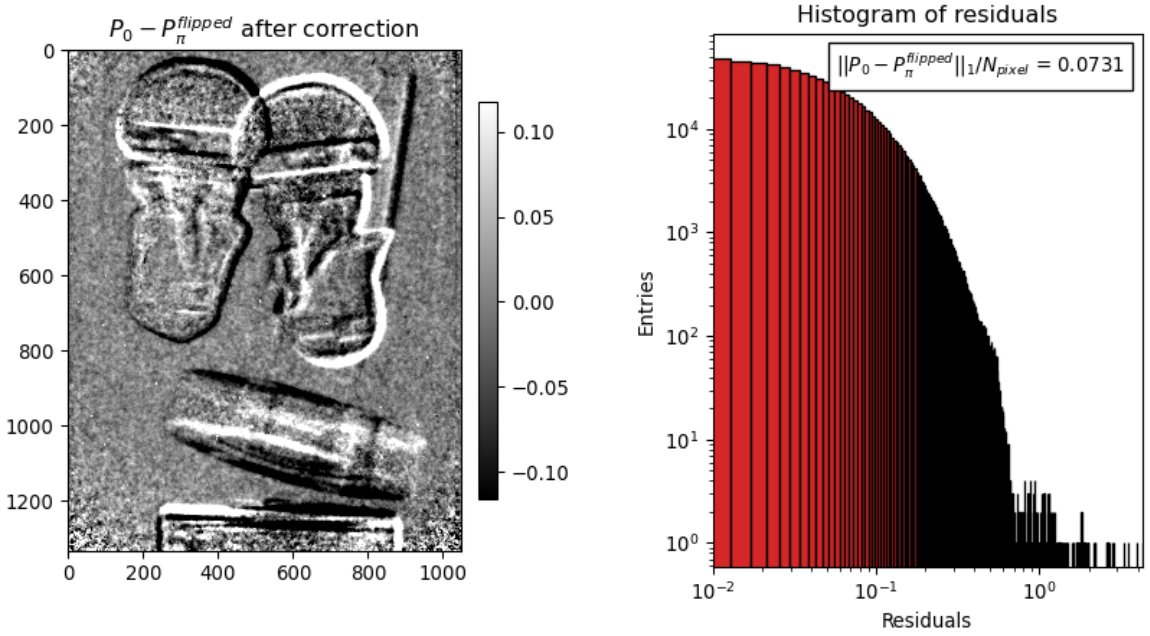

Figure 5.23: Results of the elaborations performed with ***axis of rotation*** *program, after the correction of the images. On the left the difference between the corrected projection at 0° and the flipped corrected projection at 180°. On the right the histogram of the residuals of the two images.*

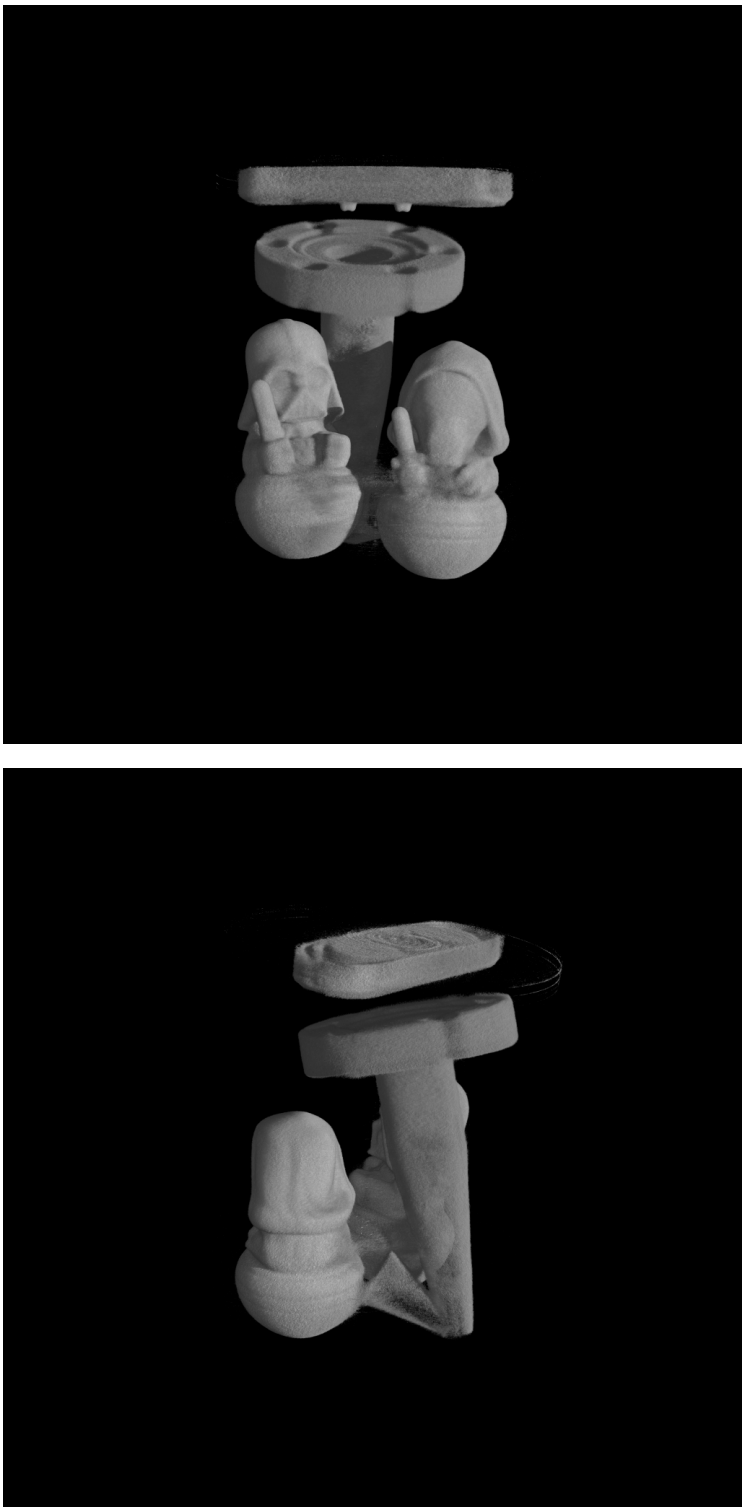

Figure 5.24: Two views of the three dimensional rendering of the tomographic reconstruction for Tomo 3.

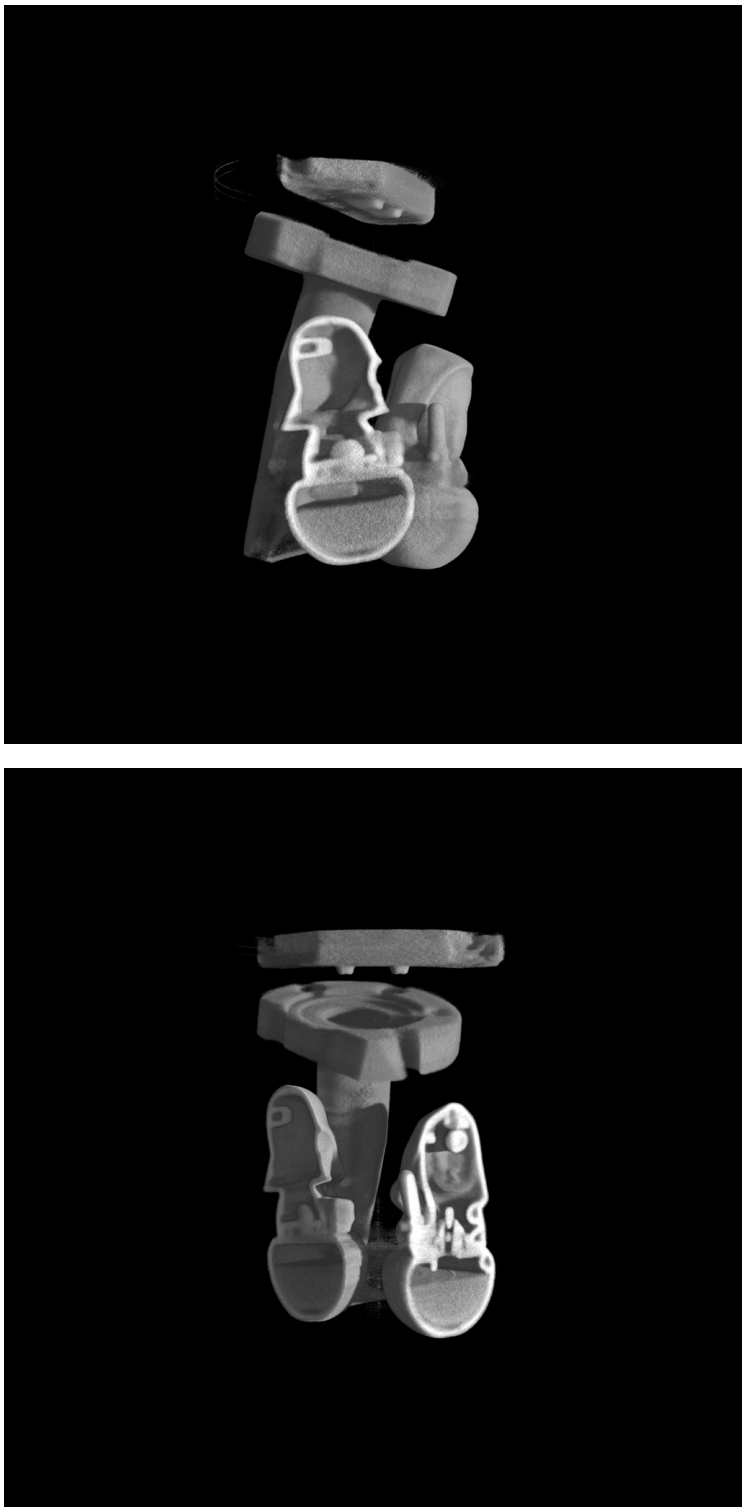

Figure 5.25: Virtual sections of the samples of Tomo 3.

Some reconstructed frontal slices of the samples, in which the accelerator component is visible, were visually compared with two images published in Grazzi F. et al. article [29], which shows virtual frontal views of the same object, obtained through the acquisition of a neutron tomography. More details are reported in the *Discussion* section 6.6.3.

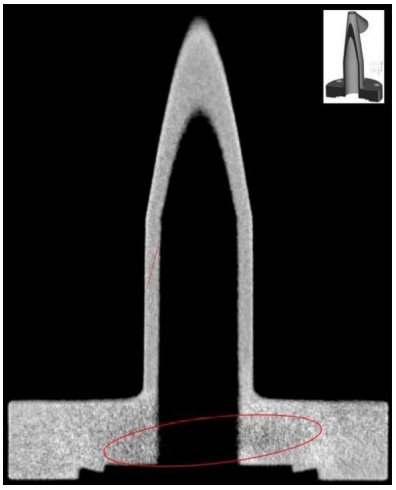

(a)

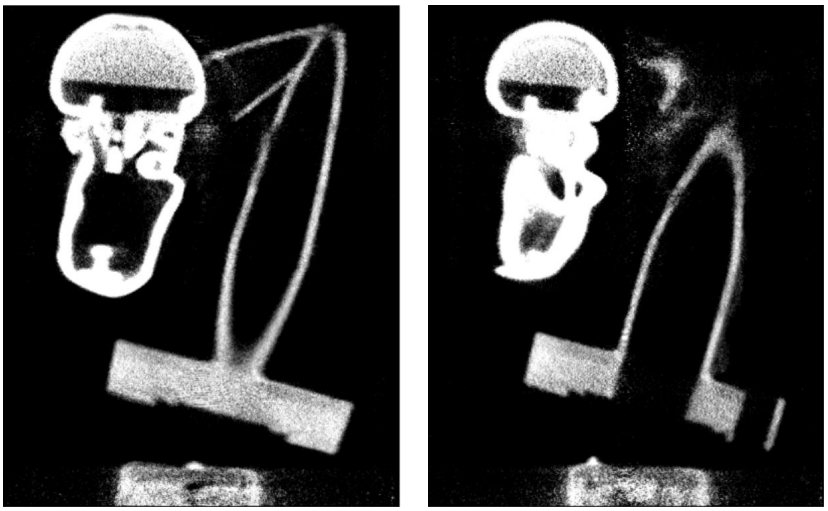

(b)

Figure 5.26: (a) From [29], a frontal view of the accelerator component. It is evident the anisotropic distribution of porosity (as highlighted by the red oval). (b) Two reconstructed vertical slices of the samples of Tomo 3. The porosity on the accelerator component base is visible. Contrast and brightness of the images are adjusted to highlight the object base details, to the detriment of a worse visualization of the plastic puppet.

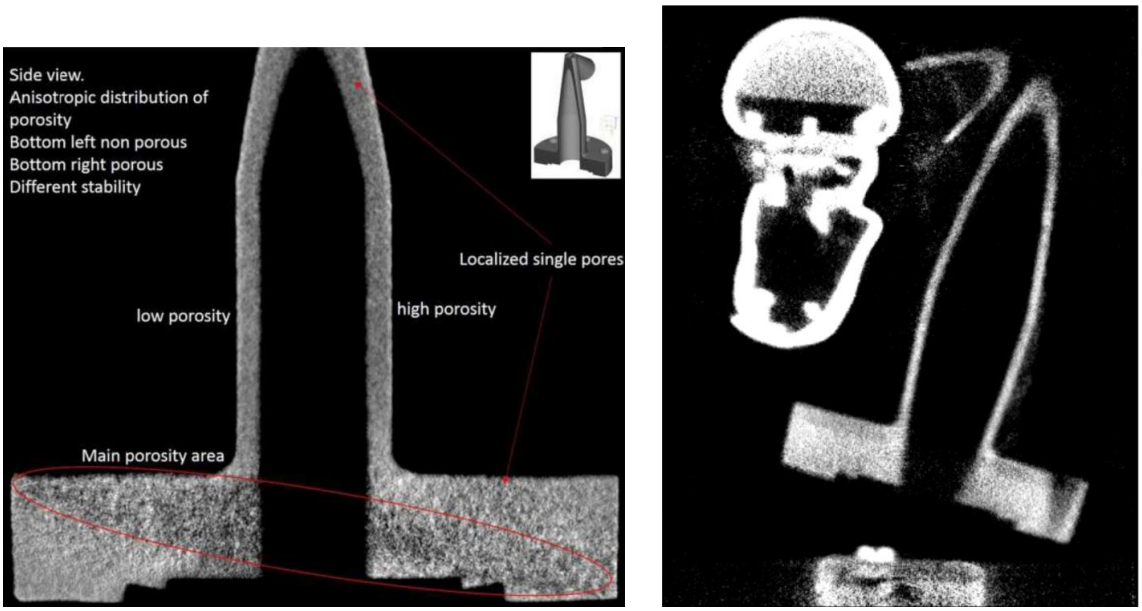

(a)

(b)

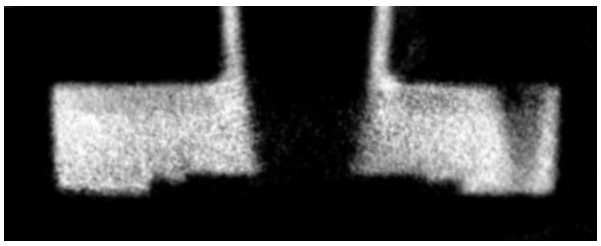

(c)

Figure 5.27: (a) From [29], a frontal section of the MACHINA exit snout (accelerator component). The anisotropic distribution of the porous areas in the different parts is clearly visible [29]. (b) A reconstructed vertical slice of the samples in Tomo 3. Contrast and brightness of the image are adjusted to highlight the object base details. (c) A zoom on the base of the MACHINA exit snout of the image (b), showing the presence of porosity.

Chapter 6

Discussion

6.1 Scintillators comparison

Looking at the fig. 5.1, it is possible to note that the $(10 \times 10)\ mm^2$ scintillators doped with Ag and Cu lead to the production of the same light signals in flat images for the thicknesses of $50\mu m$, $100\mu m$ and $200\mu m$. Increasing the thickness of the scintillator, Ag doping gives rise to a greater brightness with respect to Cu doping. Signal differences produced by Ag doped and Cu doped LiF-ZnS scintillators increase with the tickness, reaching a maximum at $400\mu m$, the last measured. The Cd doped scintillators lead to the acquisition of less bright images. It is important to note that the image produced by the LiF-ZnS:Cu $(200 \times 200)\ mm^2$ scintillator, manufactured in 2013, is brighter compared to the ones obtained with the scintillators produced 7 years later, having the same thickness ($300\mu m$). The reason of this anomaly, according to the clarification provided by "TRITEC AG" manufacturer, is that the 2013 scintillator is made with a different mixture, in terms of grain and pre-mixing, and it is an application of multiple layers, made in a different way than the new scintillators. No further information have been added by the manufacturing company.
An accurate choice of the scintillator is mandatory to achieve the goal of the experiment, that requires the acquisition of images with high brightness and spatial resolution.
In this way, it is fundamental to consider the effects of the parameters of the scintillating device.
About the thickness, on one hand, the greater is this scintillator characteristic, the wider

will be the spread of visible light cone produced into the scintillator, hence the more the images will present blurring, that corresponds to a wider PSF and to a lower spatial resolution. On the other hand, a too thin scintillator leads to a low amount of visible light production, hence to a low signal on the images, making the sample visualization and the tomographic analysis more difficult.
So, the best way is to choose a trade off between the two thickness extemes considered and the doping material that leads to bright images.
The LiF-ZnS:Cu manufactured in 2013, with a thickness of 300 μm, represented by the red star in the graph 5.1, has been chosen as scintillator for the NICHE experiment.

6.2 Spatial resolution

Let's consider the results obtained in equation 5.1, from the observation of the radiography of the Gd bar pattern, and the ones expressed in fig. 5.2 and eqs. 5.2 and 5.3, from the computation of the Modulation Transfer Function in a ROI of the same radiographic image. The observed spatial resolution, qualitatively provided by the first empirical method, $(2.9 \pm 0.2)\ lp/mm$, is compatible with the cutting frequency $f_{cut} = 3.00\ lp/mm$, more rigorously obtained by the computation of the MTF.
Now, considering the calculated Nyquist frequency, $(10.00 \pm 0.02)\ lp/mm$, that is theoretically the maximum spatial frequency detectable and correctly reproduced by the acquisition device, and the spatial frequencies corresponding to the 10% and 5% of the MTF in fig.5.2c, 1.87 lp/mm and 2.23 lp/mm, it is evident that these two latter values are considerably lower than the Nyquist frequency.
The cause of this discrepancy is attributed to the fact that the total spatial resolution is the combination of all the detection system components resolution, as explained in section 3.2.2. Hence, some components with a bad spatial resolution negatively affect the resolution of the whole system. Further analyses are required to understand which are these low spatial resolution components.

6.3 Linearity

Considering just the CCD camera, figure 5.3 shows fully linearity between the mean acquired signal and the acquisition time. This is in agreement with the theory, according to which, increasing the acquisition time, the number of detected photons increases as well as the measured signal.
In fig.4.8, that shows an image of the series acquired with just the CCD camera, it is worth noting the circular bright area inscribed in the image, due to the fact that the objective area is inscribed in the CCD camera sensor area.
Considering now the whole detection system, figure 5.4, that shows the mean intensity values of flat images as a function of the acquisition time, proves that the linearity between the acquired signal and the acquisition time is satisfied with the experimental detection setup.
Looking at the two figures 5.3 and 5.4, it is evident that the detection system irradiated by thermal neutron beam acquires in 600 s a mean signal almost equal to the one acquired in about 2 ms by the CCD camera exposed to visible light. A critical point of the neutron imaging system is here highlighted: the long needed acquisition time, especially for tomographies (about 12 hours for Tomo 2).

6.4 Signal to noise ratio

In figure 5.5, the signal to noise ratio calculated for the image series acquired with just the CCD camera is plotted as a function of the acquisition time. The mean signals, used for the linearity analysis, are plotted in fig. 5.3.
Considering the SNR calculated for the four flat images acquired with the whole detection system, as shown in fig. 5.6, and the fit of the data represented by the curve equation 5.7, it is apparent that the images are affected by unavoidable statistical noise, since the degree of the fit curve equation is 0.51 ± 0.02, compatible with 0.5. In fact, the statistical noise, as explained in section 3.2.3, is expressed by a Signal-to-Noise Ratio $SNR \propto \sqrt{N}$, with N the number of detected photons, proportional to the mean signal in the image.

6.5 Preliminary radiographic tests

Neutron radiographies in figures 5.7 and 5.8 show some interesting samples features, some of which may be not visualized with X-ray images, due to the different attenuation exerted on the two radiations by same materials.
In fig.5.7, the inside of the bronze elephant statue can be investigated, since bronze is a low attenuating material for thermal neutrons. Hence, two rods of unknown materials can be clearly visualized.
On even grater impact, in fig.5.8, it is possible to visualize all the inside of the coffee maker: water on the bottom, the coffee powder in the middle and the liquid coffee on the top section. In fact the principal component of the coffee maker is aluminium, very low attenuating material for thermal neutrons, as shown in the periodic table in fig.2.2, while organic materials and water have a high probability of interaction with thermal neutrons. Plastic components, like the coffee maker handle and the oval object on the cover, are highly visible as well, due to their high attenuating power on thermal neutrons. A X-ray radiography of the same object would have prevented the internal visualization of the coffee maker, since attenuation of X-rays by aluminium is greater than that of neutrons, as shown in fig.2.2. The acquired neutron radiographies highlight the important investigation power of neutron imaging, that allows the visualization of organic materials, hidden within metallic objects, without the necessity of physically opening the sample. This aspect is of fundamental relevance in the field of cultural heritage, where scholars and restores aim to investigate artefacts constituent materials, manufacturing processes, and conservation state, without affecting the objects integrity, due to their uniqueness and the material value.

6.6 Tomography

6.6.1 Tomo 1

In the acquired tomographic projection images (fig.5.9), it is evident a circular irradiated area, with a diameter of $(99.3 \pm 0.2)mm$, caused by the neutron divergent beam shape. It is worth noting that the illuminated area in the acquired projections is smaller than the one in the images acquired with the CCD camera without neutron irradiation (fig.4.8).

Hence, in all the tomographies, the neutron beam irradiates an area smaller than the areas of the objective and the CCD camera sensor.
Axis of rotation program provided good results for the correction of the sample axis of rotation in the images. It is evident, from fig.5.10, the misalignment of the sample axis of rotation with the central vertical axis of the images (the central axis of the detector), since the subtraction of the projection acquired at angle 0° and the flipped one at 180° should result in a null image, at most with backgroung since they are not ideal images. Instead, in the figure on the left, the image obtained by the subtraction, the borders of the samples are clearly visible. The projections correction led to a resulting image obtained by subtraction (fig.5.11 on the left) where the samples contours are less visible, improving the alignment of the sample axis of rotation with the central vertical axis of the images.
From the three dimensional rendering, it is possible to distinguish all the samples analyzed, with details on their surfaces. It is also possible to visualize the internal volume of the samples, since, in fig.5.13, the internal composition of the plastic puppet is shown, with some voids, some small plastic elements and a full base.

6.6.2 Tomo 2

The projections acquired in the second tomography, in which the acquisition configuration changes, as shown in table 4.4, provided a worse sample axis of rotation correction, with respect to the correction performed on the images of Tomo 1. The reason could be the presence of a greater amount of noise in the acquired images, that affects negatively the correction algorithm of ***Axis of rotation*** program. Nevertheless a better alignment between the sample axis of rotation and the central axis of the detector is apparent by comparing the left images in fig.5.16 and fig.5.17. In the former, the samples borders are more evident than in the latter image, where cylinders become less visible.
The three dimensional rendering in fig.5.18 allows the visualization of the cylinders arrangement, although some of them are blurred or even not visible, due to the presence of noise in the acquired images and the similar low neutron attenuation by some cylinders. Fig.5.19 shows two reconstructed axial slices, one for the superior section of the sample and one for the inferior section. If one considers the cylinders arrangement shown in fig.5.14, it is apparent that, while in the superior section all the five cylinders are

recognizable, in the inferior section one cylinder, the Al one, is not visible. The causes are: first of all, aluminium is low attenuating for thermal neutrons; secondly, even the biggest cylinder that incorporate all the others is in aluminium, hence the small and the big Al cylinders turn out to be not distinguishable; lastly, the presence of two highly attenuating cylinders (Ag and PE) in the same section of the sample gives rise to an image artifact according to which the visibility of objects in proximity of those cylinders is negatively affected.
The further analysis of the total neutron macroscopic cross section (Σ_t) of the cylinders, compared to the corresponding mean gray values in the reconstructed images, provided the calibration curve shown in fig.5.20.
First of all, since the mean signal registered for each cylinder is reported with the correspondent standard deviation, it is possible to note that the errors for the cylinders present just in the inferior section, composed by Ag, PE and Al, are greater with respect to the ones of the cylinders in the superior section, probably due to the presence of the artifact explained above.
However, from the fitting curve, it is evident a linear proportionality between the calculated Σ_t reported in table 5.1, and the mean gray level for each cylinder. The Al cylinder is the less attenuating, followed by the cylinders of lead, brass, copper and iron. The more attenuating cylinders are the Polyethylene and the Silver ones.

6.6.3 Tomo 3

The correction of the acquired projection images in Tomo 3, shown in fig.5.21, for the misalignment of the sample rotation axis with the central vertical axis of the images, provided a resulting image (fig.5.23), obtained by the subtraction of the 0° projection and the flipped 180° projection, qualitatively similar to the one obtained for Tomo 2. The samples borders are still visible, but less than the ones in the image obtained by the subtraction of the uncorrected projections (fig.5.22).
The three dimensional rendering and the virtual sections, represented in fig.5.24 and fig.5.25, allow the recognition of all the samples, with details on the surfaces. One of the puppets presents a more detailed profile, than the other puppet, probably because of the presence of a lower amount of noise in that part of the projection images. The inside of the puppets is similar to the one represented in fig.5.13 for Tomo 1, presenting

some small plastic elements, some voids and a full base.
A more detailed observation of the accelerator component was performed comparing some reconstructed frontal slices with two frontal views of the same object, shown in the article [29]. In that work, the neutron tomography of the accelerator component was performed with cold neutrons, with a wavelenght of 3Å, while in the present work, neutrons are thermal, with a wavelenght of almost 2Å. They exploited the fact that the energy of cold neutrons corresponds to the region where diffraction effects on the transmitted beam exhibit the maximum contrast, allowing the observation of microstructural features of the crystalline grains. In fact, the attenuation power of coherent scattering is related to the size of crystallographic domains, to the presence of preferential orientations, and to the compositional discrepancies [29].
As shown in fig.5.26a and fig.5.27a, it is possible to visualize the porosity distribution in the sample. In particular, in fig.5.27a, it is evident that the thick cylindrical base is highly porous, with large parts of the volume showing a lower attenuation coefficient, indicating higher porosity. This effect is particularly visible in the volume around the hollow central part of the object. In addition, the component shows a strong asymmetry in porosity distribution between the left- and the right-hand side. At the base, porosity is distributed along a diagonal ellipsoidal volume and this distribution is possibly correlated with the diagonally arranged printing direction of the sample [29]. Fig.5.26a shows again the anisotropic distribution of porosity, both radially (with respect to the central hole) and diagonally (with respect to the base).
Some reconstructed frontal slices of the present work are presented in fig.5.26b and fig.5.27b and a zoom on the base of the accelerator beam exit snout is in fig.5.27c. The high porosity of the base of the accelerator component is recognizable in the images, due to a darker, so lower attenuating area in the corresponding region, in particular near the base hollow central part.
Hence, the results of thermal neutron tomography performed with NICHE setup confirmed the outcomes reported in the article [29].

Chapter 7

Conclusions

The developed and characterized NICHE neutron imaging system has provided satisfactory results for images acquisition, allowing the acquisition of radiographies and three tomographies, but it has also highlighted the critical points of the neutron imaging system, including a long acquisition time, especially for tomographies.
The characterization analysis of the detection system led to the following results:

- the LiF-ZnS:Cu scintillator of area (200 $\times$ 200) mm^2 and produced in 2013 was chosen as scintillator for the experimental setup;

- the acquisition of a radiographic image of a Gd bar pattern led to a first qualitative evaluation of the spatial resolution ((2.9$\pm$0.2) lp/mm), compatible with the cutting frequency of the MTF (3.00 lp/mm), computed by means of PARREC software with a more rigorous method;

- the calculated spatial resolution at 10% and 5% of MTF are rispectively 1.87 lp/mm and 2.23 lp/mm, less than the computed Nyquist frequency (10.00 $\pm$ 0.02) lp/mm, because of the presence of some detection system components that negatively affect the spatial resolution of the whole acquisition setup;

- the CCD camera and the whole detection system showed linearity between the detected signal and the acquisition time. In particular, for the whole acquisition system, as shown in fig.5.4, the linearity is satisfied for all the acquisition times used in tomographies (60s for Tomo 1, 150s for Tomo 2 and 120s for Tomo 3);

- the Signal-to-Noise Ratio of the images acquired with the whole detection system, under neutron irradiation presented an increment compatible with a function $y = x^{1/2}$, with y SNR and x acquisition time. This trend reflects the predominant presence of unavoidable statistical noise in the acquired images;

After the experimental tests for the characterization of the CCD-based detector, some preliminary radiographies and three neutron tomographic scans were performed and the results are the following:

- neutron radiographic images highlighted the possibility to visualize features and organic materials inside metallic objects, prevented by X-ray imaging;
- ***Axis of rotation*** program, that I implemented, showed satisfactorily results in preprocessing the images and especially in correcting the acquired projection images for the misalignment between the sample axis of rotation and the central axis of the detector, allowing a more accurate tomographic reconstruction;
- tomographic reconstructions and the corresponding three dimensional rendering of the samples allowed the visualization of all the components, externally and internally, with some details;
- for Tomo 2, a calibration curve was computed for the conversion of the mean gray values of the reconstructed images into the total neutron macroscopic cross section of the corresponding materials;
- for Tomo 3, some reconstructed images of one of the samples (an additively manufactured metallic component, i.e. the exit-snout of the MACHINA transportable proton accelerator beam-line) were compared with the ones shown in the article [29], that reports the outcomes obtained by the acquisition of a neutron tomography of the same object, with different experimental conditions than the ones of the present work, for a non-invasive morphological and microstructural study, in order to acquire fabrication process-related microstructural information. The images reconstructed in the present work confirmed some of the features identified in the experimental research published in [29];

Some improvements of the detection system should be made in order to decrease the neutron tomography total acquisition time, that was about 12 hours for the second

tomography, letting this imaging method not feasible for the analysis of big samples, and in order to enhance the acquired images quality.
In this regard, since NICHE experimental research is still continuing, there are some new developments to be tested: a new scintillator LiF-ZnS:Ag with thickness 300 μm and area of (200 $\times$ 200) mm^2, a new CCD camera, the ZWO 2600MM Pro, with a greater resolution of 26 Mega Pixels (6248 $\times$ 4176) and a cooling system. In future, engines will be added to the movable stage in order to perform the focusing remotely and there will be a manual moving system for the setup along the neutron beam direction.
A new characterization of the detection system will be done soon, in order to determine in a quantitative way the improvement of the neutron imaging facility.

Bibliography

[1] J. Banhart, *Advanced Tomographic Methods in Materials Research and Engineering*, OUP Oxford, 2008;

[2] X. Huang, E. Uffelman, O. Cossairt, M. Walton and A. K. Katsaggelos, *Computational Imaging for Cultural Heritage: Recent developments in spectral imaging, 3-D surface measurement, image relighting, and X-ray mapping*, IEEE Signal Processing Magazine, vol. 33, no. 5, pp. 130-138, Sept. 2016, doi: 10.1109/MSP.2016.2581847;

[3] Morigi, M.P., Casali, F., Bettuzzi, M. et al., *Application of X-ray Computed Tomography to Cultural Heritage diagnostics.*, Appl. Phys. A 100, 653–661 (2010), https://doi.org/10.1007/s00339-010-5648-6;

[4] Ian S. Anderson, Robert McGreevy, Hassina Z. Bilheux eds., *Neutron Imaging and Applications*, Springer, Boston, MA, https://doi.org/10.1007/978-0-387-78693-3;

[5] J.Banhart, A.Borbely, F.García-Moreno, K.Dzieciol, I.Manke et al., *X-ray and neutron imaging - Complementary techniques for materials science and engineering*, International Journal of Materials Research, vol. 101, 2010, doi:10.3139/146.110382;

[6] Faycal Kharfi, *Mathematics and Physics of Computed Tomography*, In *Imaging and Radioanalytical Techniques in Interdisciplinary Research - Fundamentals and Cutting Edge Applications*, IntechOpen, https://doi.org/10.5772/52351;

[7] Avinash C. Kak and Malcolm Slaney, *Algorithms for Reconstruction with Nondiffracting Sources.* In *Principles of Computerized Tomographic Imaging*, pp.49-112, doi:10.1137/1.9780898719277.ch3;

[8] Avinash C. Kak and Malcolm Slaney, *Algebraic Reconstruction Algorithms.* In *Principles of Computerized Tomographic Imaging*, pp. 275-295, doi: 10.1137/1.9780898719277.ch7;

[9] Feldkamp et al., *Practical cone-beam algorithm*, Journal of The Optical Society of America A-optics Image Science and Vision, 1984, vol.1, pp. 612-619, doi:10.1364/JOSAA.1.000612;

[10] Daniel M. Pelt, Kees Joos Batenburg, *Fast Tomographic Reconstruction From Limited Data Using Artificial Neural Networks*, IEEE Transactions on Image Processing, 2013, doi: 10.1109/TIP.2013.2283142;

[11] L. Giuntini, L. Castelli, M. Massi, M. Fedi et al., *Detectors and cultural heritage: The INFN-CHNet experience*, Applied Sciences, 2021, vol. 11, doi: 10.3390/app11083462;

[12] J. Jamaludin, H. Rahim, M.H. Fazalul Rahiman et al., *Introducing an Application of a Charged Coupled Device (CCD) in an Optical Tomography System*, Jurnal Teknologi, 2015, vol. 73, doi: 10.11113/jt.v73.4253;

[13] `https://www.photometrics.com/learn/imaging-topics/linearity#:~:text=Linearity$%$20The$%$20fundamental$%$20process$%$20that$%$20occurs$%$20in$%$20CCD,captured$%$20under$%$20the$%$20gate$%$20electrodes$%$20of$%$20the$%$20CCD.`

[14] Ahmed Syed Naeem,*Position-sensitive detection and imaging*, in *Physics and Engineering of Radiation Detection*, Elsevier, 2014, pp.435-476;

[15] F. Casali, *Chapter 2 X-ray and neutron digital radiography and computed tomography for cultural heritage*, in *Physical Techniques in the Study of Art, Archaeology and Cultural Heritage*, Elsevier, vol.1, 2006, pp. 41-123, doi: 10.1016/S1871-1731(06)80003-5;

[16] Nikolay Kardjilov, Giulia Festa, *8 General Introduction to Neutron Physics and Instrumentation*, in *Neutron Methods for Archaeology and Cultural Heritage*, Springer, 2017, doi:10.1007/978-3-319-33163-8;

[17] P. Rinard, *Neutron Interactions with Matter*, 1997;

[18] Lehmann E.H. et al., *Bronze Sculptures and Lead Objects Tell Stories About Their Creators: Investigation of Renaissance Sculptures and Ancient Ingots by Means of Neutron Tomography.* In: Kardjilov N., Festa G. (eds) *Neutron Methods for Archaeology and Cultural Heritage. Neutron Scattering Applications and Techniques.* Springer, Cham., https://doi.org/10.1007/978-3-319-33163-8_2;

[19] Lehmann E.H., Hartmann S., Speidel M.O., *Investigation of the content of ancient Tibetan Metallic Buddah Statues by means of neutron imaging methods*, Archaeometry 52, vol. 3, 2009, doi: 10.1111/J.1475-4754.2009.00488.X;

[20] Mannes D., Schmid F., Frey J., Schmidt-Ott K., Lehmann E.,*Combined Neutron and X-ray Imaging for Non-invasive Investigations of Cultural Heritage Objects*, Physics Procedia, vol.69, 2015, doi: 10.1016/j.phpro.2015.07.092;

[21] `https://www.isnr.de/images/facilities/NI_Facilities_Database_v2019-02-04.pdf`;

[22] Prata M., Alloni D., De Felice P. et al., *Italian neutron sources*, The European Physical Journal Plus, vol.129, 2014, doi: 10.1140/epjp/i2014-14255-3;

[23] `https://astronomy-imaging-camera.com/product/asi178mm-mono`;

[24] Brancaccio R., Bettuzzi M., Casali F., Morigi M.P. et al., *Real-time reconstruction for 3-D CT applied to large objects of cultural heritage*, IEEE Transactions on Nuclear Science, vol.58, 2011, pp. 1864-1871, doi: 10.1109/TNS.2011.2158850;

[25] `https://imagej.nih.gov/ij/`;

[26] `https://github.com/NaomiOrlandi/axis_of_rotation`;

[27] `https://www.volumegraphics.com/en/products/vgstudio.html`;

[28] `https://www.ncnr.nist.gov/resources/n-lengths/`;

[29] Grazzi F., Cialdai C., Manetti M., Massi M., Morigi M.P., Bettuzzi M. et al., *A multi-technique tomography-based approach for non-invasive characterization of additive manufacturing components in view of vacuum/UHV applications: preliminary*

results, Rendiconti Lincei. Scienze Fisiche e Naturali, vol.32, pp. 463-477, 2021, doi: 10.1007/s12210-021-00994-2;